IMAGE: A MAP OF THE STARS OF THE ORION CONSTELLATION

Print ISSN: 2631-8490 Online ISSN: 2631-8504

JournalPreview

London Journal of Research in Science: Natural & Formal

Volume 25 | Issue 6 | Compilation 1.0

Great Britain Journals Press

WWW.JOURNALSPRESS.COM

Journal Content
In this Issue

Great Britain Journals Press

A Physics-based Model of Hydrogen Bond Disruption in Cell Membranes Under Electric Fields

J. W. McPherson

ABSTRACT

A physics-based model is presented to explore the impact of external electric fields on hydrogen bonding within human cells. Drawing from fundamental dielectric physics and the role of hydrogen bonding in cell membrane integrity, the model demonstrates that minimal to no membrane degradation occurs at electric field strengths of ≤ 200 V/cm. However, it predicts that significant membrane damage begins at field levels as low as 1 kV/cm, with strong and irreversible degradation occurring at 10 kV/cm, and catastrophic membrane failure at 40 kV/cm. The model emphasizes that any degradation of the cell membrane— which normally serves as a hydrophobic barrier—can allow water molecules to penetrate and disrupt critically important hydrogen bonds, accelerating cellular failure. These findings are important not only for establishing safe exposure limits to external electric fields in humans but also for advancing electroporation techniques, where targeted cell membrane disruption is used therapeutically, particularly in cancer treatment.

Keywords: NA

Classification: LCC Code: QH601

Language: English

Great Britain Journals Press

LJP Copyright ID: 925661
Print ISSN: 2631-8490
Online ISSN: 2631-8504

London Journal of Research in Science: Natural & Formal

Volume 25 | Issue 6 | Compilation 1.0

A Physics-based Model of Hydrogen Bond Disruption in Cell Membranes Under Electric Fields

J. W. McPherson

ABSTRACT

A physics-based model is presented to explore the impact of external electric fields on hydrogen bonding within human cells. Drawing from fundamental dielectric physics and the role of hydrogen bonding in cell membrane integrity, the model demonstrates that minimal to no membrane degradation occurs at electric field strengths of ≤ 200 V/cm. However, it predicts that significant membrane damage begins at field levels as low as 1 kV/cm, with strong and irreversible degradation occurring at 10 kV/cm, and catastrophic membrane failure at 40 kV/cm. The model emphasizes that any degradation of the cell membrane— which normally serves as a hydrophobic barrier—can allow water molecules to penetrate and disrupt critically important hydrogen bonds, accelerating cellular failure. These findings are important not only for establishing safe exposure limits to external electric fields in humans but also for advancing electroporation techniques, where targeted cell membrane disruption is used therapeutically, particularly in cancer treatment.

Author: PhD, IEEE Fellow McPherson Reliability Consulting LLC.

I. INTRODUCTION

Human life, as we know it, cannot exist without hydrogen bonds (H-bonds). [1-3] These bonds are essential for the functioning of biological molecules such as DNA and proteins. However, the H-bonds are relatively weak (~ 0.1ev) versus the much stronger ionic and covalent bonds (~1eV). In chemistry, H-bonds have historically been described symbolically as $X - H$ ---- Y. [4] Here, $X - H$ represents a strong bond (ionic and/or covalent) between atom X and H and H --- Y represents a much weaker electrostatic bond to a neighboring polar molecule.

In biochemistry, X usually stands for Oxygen or Nitrogen. Since X and H have significant differences in electronegativity, the electron cloud around the H atom will be shifted more towards X. This electron cloud shifting results in H becoming more positively charged and X becoming more negatively charged. In chemistry, this electron cloud shifting is generally referred to as increased polar bonding while in physics this is generally referred to as a dipole formation. With the H now positively charged, the hydrogen can form a weak electrostatic bond with the negative end of an adjacent polar molecule. Thus, the bonding between the polar molecule $X - H$ and the polar molecule Y can be described as a dipole-dipole interaction.

The modeling for the impact of electric field on H-bonds will begin with a look at the fundamental physics and chemistry of hydrogen bonding and its importance for living organisms. [4,5] This is followed with a short review of fundamental dielectric physics and the development of the CCD-Model for the human cell. The impact of external field on H-bond degradation is given special attention with an emphasis on both safe-levels of electric fields for humans and electric field levels that are important for electroporation. The paper is concluded with a detailed look the frequency dependence of pulsed electric fields on cell membranes.

London Journal of Research in Science: Natural & Formal

II. HYDROGEN BONDS (H-BONDS)

Shown In Fig. 1 are two interacting dipoles. This dipole-dipole interaction potential energy can lead to an H-bonding state (negative potential energy state).

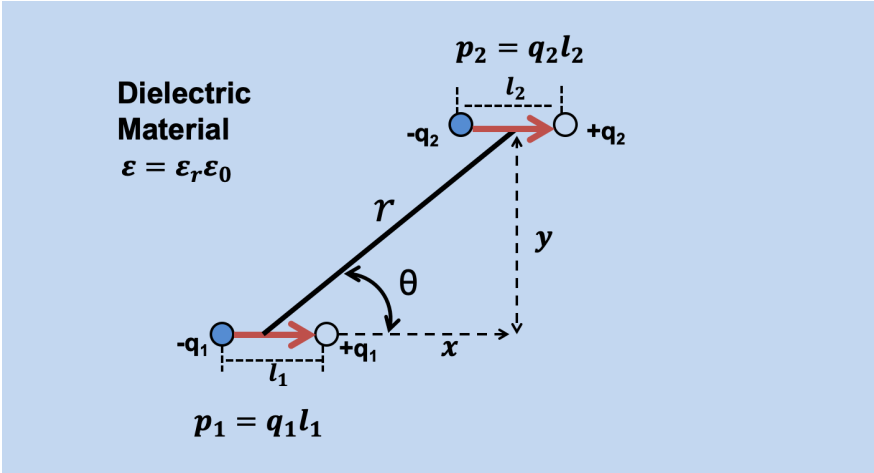

Fig. 1: Interacting dipoles lead to the H-bond state. Note that cos *cos* (θ) $= x/r$ where $r = \sqrt{x^2 + y^2}$.

As derived in the Appendix, the interaction energy for two dipoles is given by:

$$U(r) = \frac{p_1 p_2}{4\pi\varepsilon_r\varepsilon_0 r^3}(1 - 3cos^2\theta) \quad . \tag{1}$$

Generally, from Eq.(1), one can see that the maximum bonding potential energy (most negative potential energy U) occurs at θ= Zero while the repulsive potential energy (U is positive) starts at $\theta = 54.7^o$.

To further illustrate the H-bond energy dependence on bonding angle, in Fig. 2 we have used dipole moments of $p_1 = p_2 = 0.5e$Å, a bonding distance between dipoles of $r = 2.7$Å, and a free space permittivity of $\varepsilon_0 = 5.52\times10^{-3}\frac{e}{V\cdot Å}$. We see that the H-bond energy has a strong dependence on H-bonding angle θ and on the relative dielectric constant ε_r of the material in which the H-bond is imbedded.

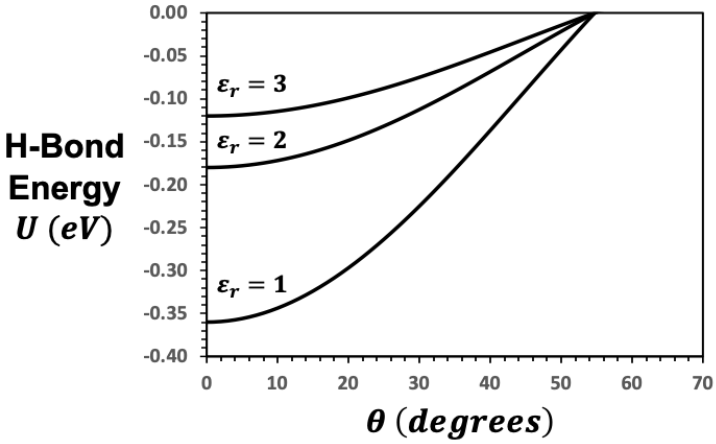

Fig. 2: H-bond energy as a function bond angle θ and relative dielectric constant ε_r. No bonding ($U \geq 0$) occurs for $\theta \geq 54.7$ degrees

For calculations that follow, it is instructive to express Eq. (1) in terms of the lateral separation distance x and the vertical separation distance y (as was illustrated in Fig. 1):

$$U(r) = \frac{p_1 p_2}{4\pi\varepsilon_r\varepsilon_0(x^2+y^2)^{3/2}}\left[1 - 3\left(\frac{x^2}{x^2+y^2}\right)\right]. \quad (2)$$

H-bond potential energy is shown in Fig. 3 (as a function of the lateral distance x for a fixed vertical distance $y = 2.7$Å) for materials with different relative dielectric constants.

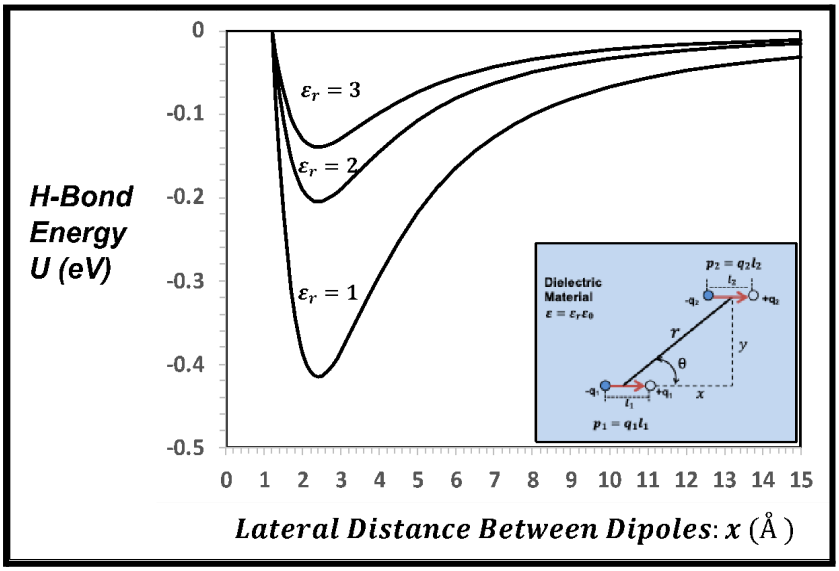

Fig. 3: H-bond potential energy as a function lateral distance x between dipoles with a fixed vertical separation of y=2.7Å. Strongest bonding (minimum energy) occurs for lateral distance of $x = 2.4$Å, giving a desired bonding angle for this particular charge configuration of $\theta \cong 48.4^{o}$

In Fig. 4, we show both the lateral-distance dependence x and the vertical-distance dependence y for the interacting dipoles that were shown in Fig. 1. In these calculations, $\varepsilon_r = 3$ was used because of its importance when we discuss H-bonding in cell membranes (found later in Section V).

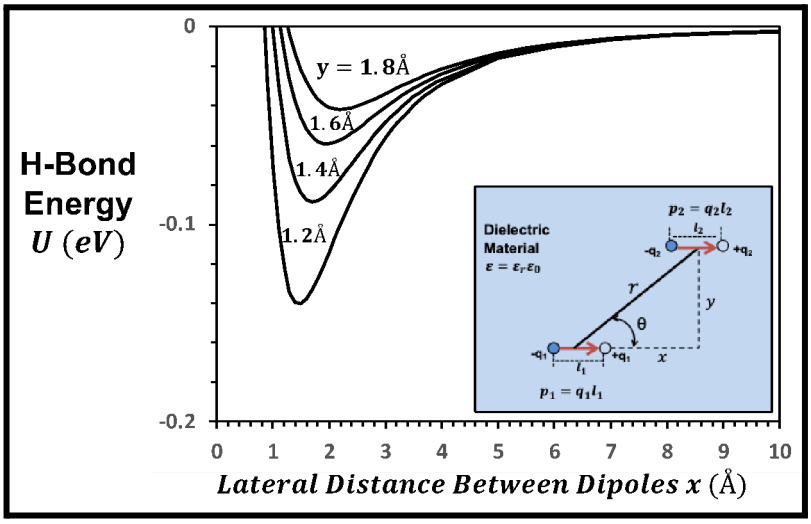

Fig. 4: The impact of horizontal displacements (x) and vertical displacements (y) on H-bond potential energy in a dielectric material of relative constant $\varepsilon_r = 3$.

In the work that follows, the impact that an external electric field has on H-bonding will be investigated in terms of field-dipole interaction. Since H-bonding is fundamental for cell life, then a predictive physical model for field-induced H-bond degradation could be very useful. The physical model could be used for not only determining safe levels of external electric field for human beings but also be used for determining optimal external electric-field levels for electroporation of cancer cells

III. IMPACT OF EXTERNAL FIELD ON H-BONDS

Shown in Fig. 5 is a H-bond in the presence of an electric field in the dielectric material.

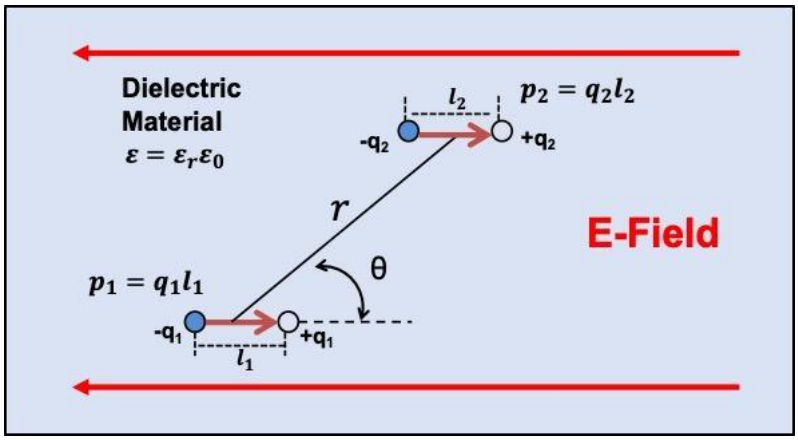

Fig. 5: The H-bond in the presence of an electric field in a material with relative dielectric constant ε_r.

The impact of the electric field on the H-bond potential energy is given by:

$$U(r) = \frac{p_1 p_2}{4\pi\varepsilon_r\varepsilon_0 r^3}\,(1 - 3cos^2\theta) \; - (\,\overrightarrow{p_1} + \overrightarrow{p_2}\,) \cdot \vec{E}_{dielectric} \; . \tag{3}$$

If we assume that the dipoles are approximately of equal magnitude ($p_1 = p_2 = p_0$) and opposite to the field (as illustrated in Fig. 5), then the field-dipole interaction serves to increase the potential energy of the H-bond (and thereby reduces the H-bond energy) by the amount:

$$\Delta U(r) = \; +2p_0 E_{dielectric} \; . \tag{4}$$

Thus, we see that fields in the dielectric material approaching ~ 1MV/cm will have an impact on reducing the H-bonding energy. As will be demonstrated in Section VI, fields in the cell membrane layers can easily approach and exceed 1MV/cm during electroporation procedures.

IV. IMPACT OF WATER MOLECULES ON H-BONDS

Water is an exceptionally effective solvent for polar-bonded materials. For instance, solid sodium chloride (NaCl), which is strongly polar-bonded, is resistant to dissolution in most non-polar, petroleum-based solvents such as mineral spirits, kerosene, and xylene. However, NaCl dissolves readily in water due to the strong interaction between water molecules and polar bonds. This behavior illustrates a key property of water: its ability to disrupt polar interactions. Polar hydrogen bonds, particularly those within biological systems, are highly susceptible to interference by water molecules. Under normal physiological conditions, the polar H-bonds present in the cell membrane are shielded from water by the membrane's hydrophobic lipid bilayer. This hydrophobic barrier helps maintain membrane stability and protects the structural integrity of membrane-bound proteins and other components. However, any disruption or compromise in the membrane's dielectric layer—whether due to physical damage, chemical exposure, or an external electric field—can permit water molecules to penetrate the membrane. Once inside, these water molecules can interact with and break existing hydrogen bonds, leading to widespread H-bond degradation. This process ultimately contributes to rapid membrane failure, which can have serious biological consequences.

Shown in Fig. 6 is a water molecule with its polar nature and the dipole-moment formation.

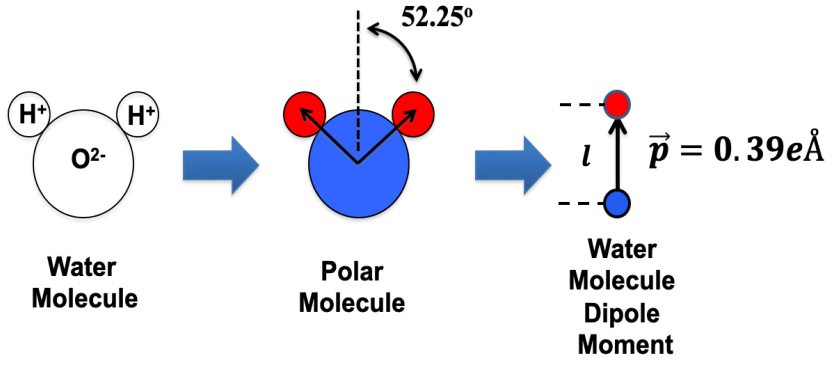

Fig. 6: Water is a very polar molecule with a dipole moment of 0.39eÅ .

The dipole moment of the water molecule depends on the amount of charge transfer from the hydrogen to the oxygen (z*e), bonding angle, and the distance between the hydrogen and oxygen atoms. The dipole moment for the water molecule is given by:

$$p = 2(z^*e)\cdot l\cdot \cos(52.25^o) = 2(0.32e)(1\text{Å})\cos(52.25^o) = 0.39e\text{Å} \quad (5)$$

From Eq.(1) we see that the strongest H-bond will occur when $\theta = 0$. The impact of an approaching water molecule has on such a H-bond is shown in Fig. 7 (for a material with relative dielectric constant $\varepsilon_r = 3$). A relative dielectric constant of $\varepsilon_r = 3$ was selected because of its usefulness when we discuss cell membranes in Section V.

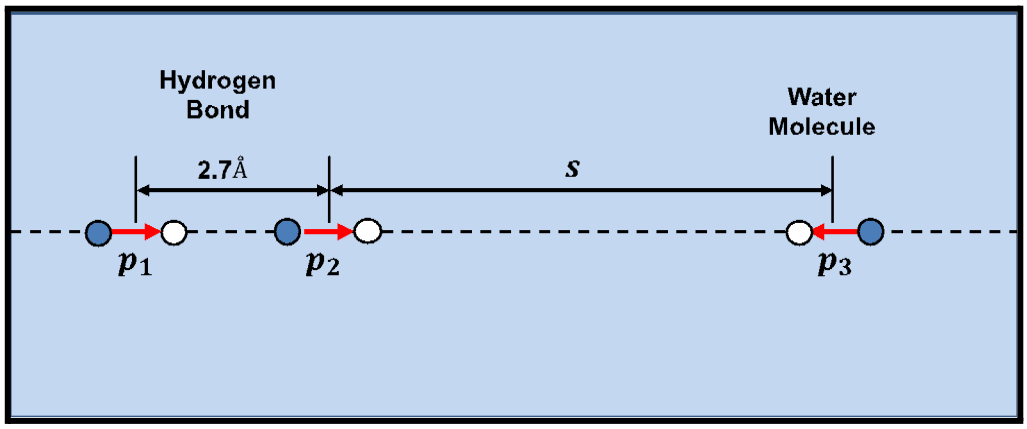

Fig. 7: H-bond is shown plus a water molecule at some distance *s* away.

The potential energy of the charge distribution in Fig. 7 is given by:

$$U = -\frac{p_1 p_2}{2\pi\varepsilon_r\varepsilon_0(2.7)^3} + \frac{p_1 p_3}{2\pi\varepsilon_r\varepsilon_0(s+2.7)^3} + \frac{p_2 p_3}{2\pi\varepsilon_r\varepsilon_0(s)^3}. \quad (6)$$

In Fig. 8 we show what happens to the H-bond potential energy *U* as the water molecule approaches.

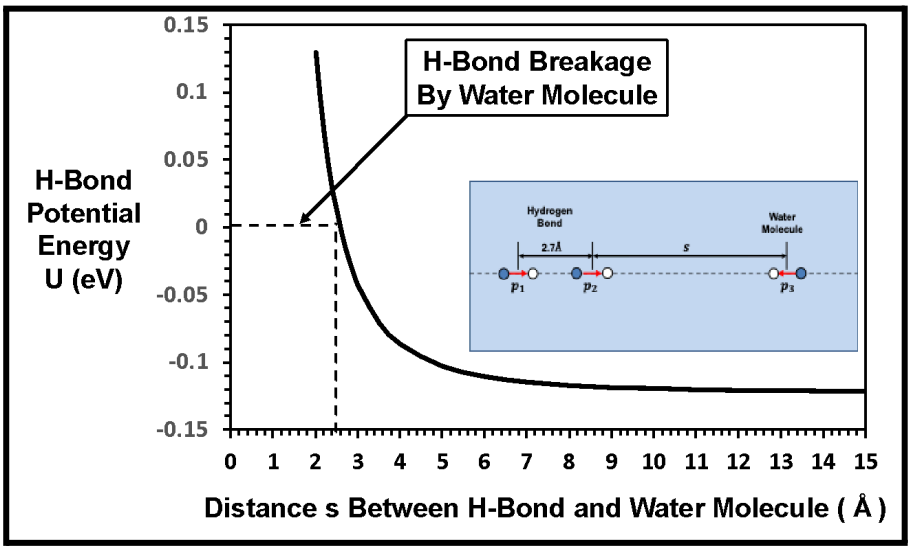

Fig. 8: H-Bond breakage by an approaching water molecule.

Fig. 8 shows that (for this material with relative dielectric constant $\varepsilon_r = 3$) H-bond weakening starts to occur when the water molecule is 10Å away and H-bond breakage occurs with the water molecule is $\cong$ 2.5 Å away.

A water molecule in a dielectric material can easily generate very high local electric fields . This is the reason that water molecules are so effective in H-bond breakage, as illustrated in Fig. 9.

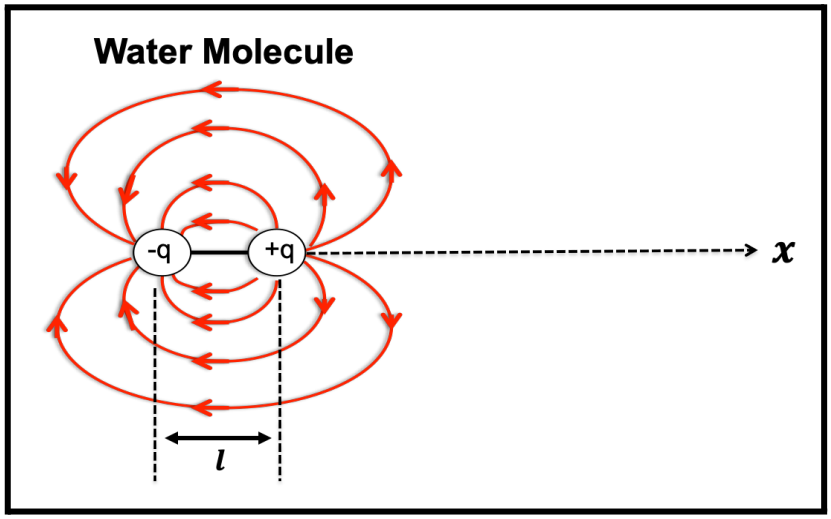

Fig. (9): Electric field lines associated with a water molecule/dipole.

The potential at location x [in Fig. (9)] due to the dipole-charge distribution is:

$$V(x) = \left(\frac{q}{4\pi\varepsilon_r\varepsilon_0}\right)\left[\frac{1}{x} - \frac{1}{x+l}\right] \quad . \tag{7}$$

The field at any location x (from the water-molecule dipole) is given by:

$$E = -\frac{dV}{dx} = \left(\frac{q}{4\pi\varepsilon_r\varepsilon_0}\right)\left[\frac{1}{x^2} - \frac{1}{(x+l)^2}\right] \quad . \tag{8}$$

Thus, for a water molecule (with dipole charge of $q = 0.39e$ and $l = 1$Å) in a material of relative dielectric constant $\varepsilon_r = 3$, the field at a distance of 2.5Å from the water molecule is approximately 15MV/cm. With this field, the H-Bond potential energy increase due the water molecule is

$$\Delta U(r) = 2p_0E_{dielectric} = 2(0.5e\text{Å})(15MV/cm) = +0.15eV \tag{9}$$

This increase in potential energy can serve to reduce the H-bond energy to zero. It can now be seen, regardless of whether we take a charge approach [Eq. (6)] or a field approach [Eq.(8)], we reach the same conclusion: a water molecule coming to within 2-3Å of a hydrogen bond can easily break the bond.

V. IMPACT OF EXTERNAL ELECTRIC FIELDS ON HUMAN CELLS

Electroporation refers to the application of external electric fields to induce pore formation in cell membranes. [6–14] The creation of these pores typically leads to either necrosis (cell death) or apoptosis (irreversible cellular degradation). Although electroporation has been studied for over four decades, [6–14] detailed physical models that fully describe the underlying mechanisms remain a subject of active research and interest. [15–18] To optimize electroporation protocols, physics-based models are essential for quantitatively analyzing how variables such as pulse amplitude, frequency, and duration influence membrane disruption. More critically, from a molecular physics perspective, there remains a fundamental question: Which specific molecular bonds are being disrupted during the electroporation process?

This work introduces a self-consistent, physics-based model that focuses on the field-induced breakage of hydrogen bonds—key molecular interactions that are vital for maintaining the structural integrity of the cell membrane. The modeling approach draws heavily from reliability physics research in the semiconductor industry, particularly studies on time-dependent dielectric breakdown (TDDB), a long-standing issue in microelectronics. [19–23] In both cases, bond degradation under electric stress is the central failure mechanism, providing a strong conceptual and mathematical bridge between biological and electronic systems.

For modeling purposes, the structure of a human cell is depicted in Fig. 10. The cytoplasm occupies the majority of the cell's volume and consists primarily of water with dissolved ions such as Na^+, K^+, and Cl^-. This region has a high relative dielectric constant of approximately $\varepsilon \approx 70$. The nucleoplasm, comprising about 10% of the total cell volume, has similar dielectric properties. The cell membrane, which is the primary focus of electroporation research, is a thin hydrophobic layer that encapsulates the cell. It functions as a selective barrier, permitting controlled ion transport while shielding the interior from external perturbations. Critically, this membrane has a much lower relative dielectric constant of $\varepsilon \approx 3$ and derives much of its mechanical and chemical stability from hydrogen bonding. The disruption of these H-bonds under an applied electric field is central to the electroporation mechanism explored in this study.

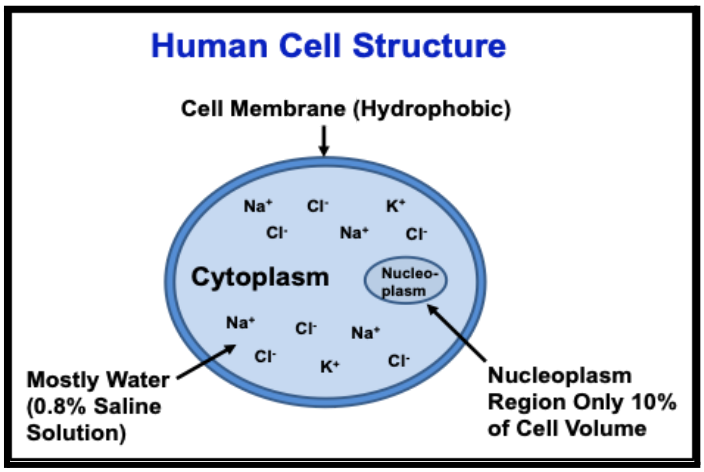

Fig. 10: Illustration of human cell-structure used for dielectric modeling.

The cell membrane is relatively impermeable and protects the cell. However, pulsed electric fields can make the cell membrane permeable. Water molecule penetration into the membrane will cause rapid H-bond breakage leading to rapid cell membrane degradation. Electroporation is generally referred to as the use of pulsed electric fields to make the cell membrane more permeable. Pore formation in the

cell membrane can lead to apoptosis (severe irreversible cell degradation) or to cell necrosis (cell death) as is illustrated in Fig. 11.

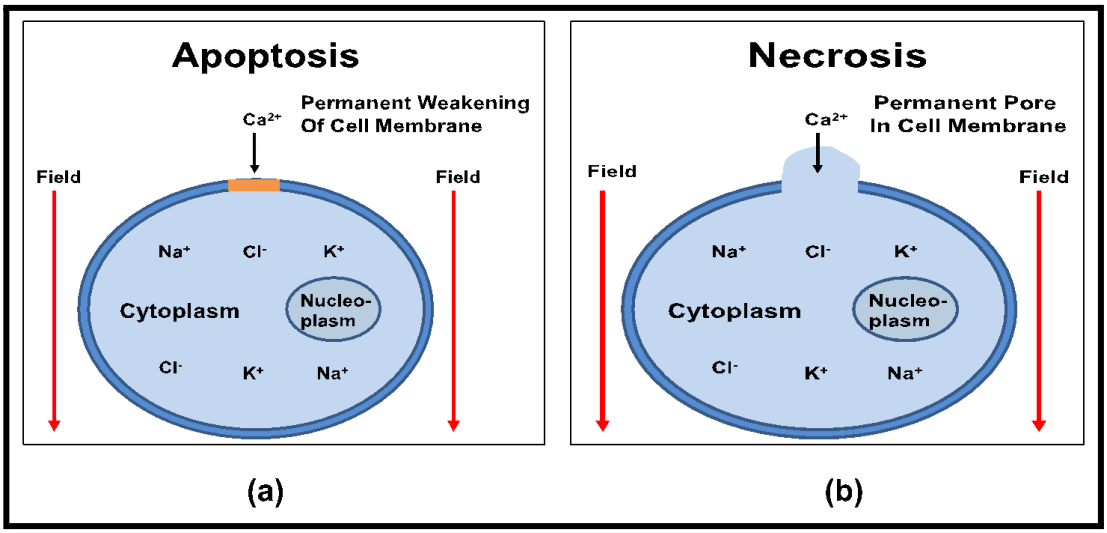

Fig. 11: (a) Permanent weakening of cell membrane eventually causing cell death (Apoptosis). (b) Permanent pore formation causing rapid cell death (Necrosis).

VI. CELL CAPACITOR DIELECTRIC MODEL

Figure 12 illustrates the primary components of the Cell Capacitor Dielectric (CCD) Model, which provides a simplified but insightful framework for understanding how electric fields interact with cellular structures. The model highlights three key elements:

1. *Cytoplasm Region:* This internal cell environment is composed of approximately 80% water and contains a variety of dissolved ions, primarily sodium (Na^+), potassium (K^+), and chloride (Cl^-). Due to its high water content, the cytoplasm exhibits a high relative dielectric constant of approximately $\varepsilon \approx 70$, making it highly responsive to electric fields.
2. *Mobile Ions:* These charged particles are free to move within the cytoplasm and play critical roles in maintaining membrane potential, signaling, and other cellular functions. Their distribution and dynamics are central to the cell's electrical behavior.
3. *Cell Membrane:* The membrane is a thin, hydrophobic dielectric layer surrounding the cytoplasm. It has a significantly lower relative dielectric constant of approximately $\varepsilon \approx 3$ and functions as both a protective barrier and a regulatory interface for ion transport. Structurally, the membrane is stabilized by hydrogen bonding, which is critically important for maintaining its integrity.

The hydrophobic nature of the membrane serves a crucial role—it prevents water molecules from penetrating and disrupting the hydrogen bonds within the membrane structure. As discussed earlier, these H-bonds are essential for membrane stability. If the dielectric layer is compromised, water molecules may infiltrate the membrane, leading to extensive H-bond breakage. This, in turn, can trigger necrosis or apoptosis, ultimately compromising cell viability.

By modeling the cell as a capacitor—with the cytoplasm and extracellular environment acting as conductive plates and the membrane as the dielectric layer—this CCD framework enables quantitative analysis of how external electric fields affect cellular function and stability. It also provides a physical

foundation for understanding phenomena such as electroporation and dielectric breakdown in biological systems.

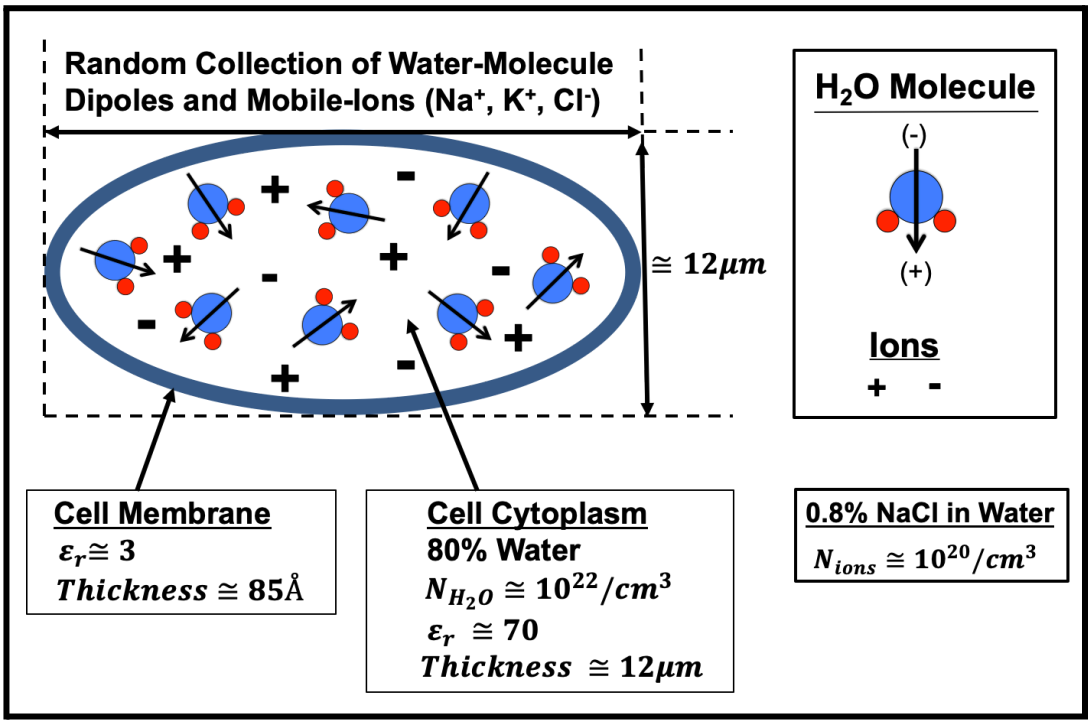

Fig. 12: Physical Model used for Cell Dielectric Analysis. Cell cytoplasm is saline like ($\varepsilon_r = 70$) and is treated as a collection of water molecules plus positive and negative ions. The protective cell membrane layer is more rigid and hydrophobic with a relative dielectric constant of $\varepsilon_r = 3$.

If an external electric field is applied to the cell shown in Fig. 12, the water-molecule dipoles will rotate and align with the electric field and the mobile-ions will drift with the electric field, as illustrated in Fig. 13.

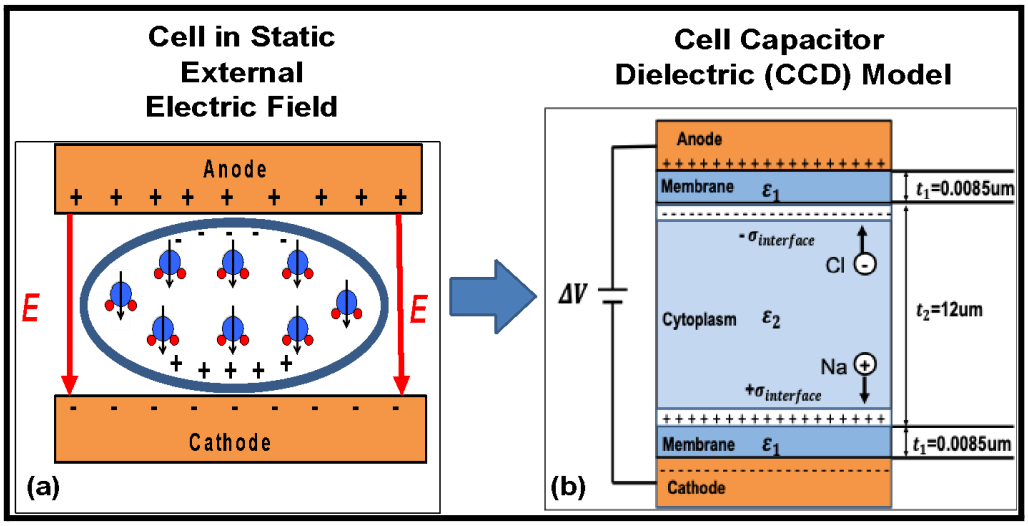

Fig. (13): (a) In a static electric field, due to the relative dielectric constants, polarization will occur in both the cytoplasm and membrane layers. Also, any mobile ions will move in the cytoplasm as illustrated. (b) This will be the cell capacitor dielectric (CCD) model used in this work.

Fig. 13(b) illustrates the Cell Capacitor Dielectric Model (CCD-Model) used in this modeling effort to describe a human cell under an external electric field stress. In between the two metal electrodes, we show the cell cytoplasm (~12um thick) and the cell membranes (each about 85Å thick). The cytoplasm is about 80% water and its dielectric constant will be taken to be approximately $\varepsilon_r = 70$ since water molecules are very polar. Because the cell membrane is hydrophobic (little to no water molecules exist in this layer), the dielectric constant of the inner core of the cell membrane is taken to be $\varepsilon_r = 3$.

In the CCD Model, if we ignore the mobile-ion drift for a moment, and use the fact that the electric displacement ($D = \varepsilon E$) is continuous across dielectric interfaces, then the fields in each layer become

$$E_{membrane} = \left[\frac{2t_1 + t_2}{2t_1 + \frac{\varepsilon_1}{\varepsilon_2} t_2}\right] E_{external} \tag{10}$$

and

$$E_{cytoplasm} = \frac{2t_1 + t_2}{\frac{\varepsilon_2}{\varepsilon_1}(2t_1) + t_2} E_{external} \quad . \tag{11}$$

where the external field is defined as simply the voltage dropped a across the total dielectric thickness:

$$E_{ext} = \frac{\Delta V}{2t_1 + t_2} \quad . \tag{12}$$

Using Eqs. (10) and (11), we see that, under static field conditions, the field in the membrane layer is 23.3 times greater than the field in the cytoplasm layer,

$$E_{membrane} = \frac{\varepsilon_2}{\varepsilon_1} E_{cytoplasm} = 23.3 E_{cytoplasm} \quad . \tag{13}$$

Any ion movement (due to the field and ions in the cytoplasm) will, of course, produce ion current and this current will lead to a charge buildup $\sigma_{interface}$ at the interface boundary between the cytoplasm and the membrane. This ion-charge buildup will lead to a further field increase in the membrane layer but reduced field in the cytoplasm layer, as given by:

$$E_{membrane} = \left[\frac{2t_1 + t_2}{2t_1 + \frac{\varepsilon_1}{\varepsilon_2} t_2}\right] E_{external} + \frac{\sigma_{interface}}{\varepsilon_1 \varepsilon_0} \tag{14}$$

and

$$E_{cytoplasm} = \left[\frac{2t_1 + t_2}{\frac{\varepsilon_2}{\varepsilon_1}(2t_1) + t_2}\right] E_{external} - \frac{\sigma_{interface}}{\varepsilon_2 \varepsilon_0} \quad . \tag{15}$$

The Na-ion and Cl-ion drift will continue in the cytoplasm layer until forces on the ions are balanced (by the tendency to drift due to the field in the cytoplasm $E_{cytoplasm}$ versus the repulsive nature of like-charge building up at the interface). In steady-state, the equivalent but opposite forces on the ions of charge q becomes:

$$q\left(E_{cytoplasm} - \frac{(\sigma_{interface})max}{\varepsilon_2\varepsilon_0}\right) = q\frac{(\sigma_{interface})max}{\varepsilon_2\varepsilon_0} \quad . \tag{16}$$

Eq.(16) [with the help of Eq. (11)] gives:

$$(\sigma_{interface})_{max} = \frac{\varepsilon_2\varepsilon_0}{2}E_{cytoplasm} = \frac{\varepsilon_2\varepsilon_0}{2}\frac{2t_1 + t_2}{\frac{\varepsilon_2}{\varepsilon_1}(2t_1) + t_2}E_{external} = \left(0.19\frac{e}{V\cdot Å}\right)E_{ext}. \tag{17}$$

For example, at E_{ext} =1kV/cm, the steady state interfacial charge buildup would be $(\sigma_{interface})_{max} = 1.9\times10^{10} e/cm^2$.

Finally, the field in each layer, due external field plus mobile-ion movement, is given by

$$E_{membrane} = 34.2E_{ext} \tag{18}$$

and

$$E_{cytoplasm} = 0.48E_{ext} \quad . \tag{19}$$

One will recall that without mobile-ion movement, the field in the cell membrane was some 23.3 times greater than in the cytoplasm. With the Na and Cl ion drift (in the saline), the field in the membrane has increased to 71.3 times greater than the field in the cytoplasm. This means that in steady state, the expected degradation is most severe in the cell membrane.

As for how fast can the ions drift in order to establish the interface concentration of $(\sigma_{interface})_{max}$, the response time can occur within microseconds. This is because the actual drift distance is relatively short. With a 0.8% NaCl solution, there are ~10^{20} /cm^3 Na and Cl ions present in the solution. Therefore, when a field is applied, if the Cl ions only drift 1Å away from the cathode (or Na ions drift only 1Å away from the anode), then this drifting leaves behind an enormous surface ion-concentration on the order of $\sim10^{15}/cm^2$. This is more than enough to create the equilibrium $(\sigma_{interface})_{max}$.

The impact of a static external electric field on H-bonds will be quite different in each layer since the field in each layer is different. In the membrane layer, the field in this layer can be ~ 70 times greater than the field in the cytoplasm layer. For this reason, we will focus our attention on the membrane. The reduction in H-bond strength in the membrane layer can be as great as,

$$\Delta U = 2p_0E_{membrane} = (1eÅ)(34.2)E_{ext} \quad . \tag{20}$$

To help comprehend the degrading impact of this reduction in H-bond energy has on human cells, it is instructive to determine a effective temperature-rise equivalent (TRE) for this amount of energy. TRE can be useful because we know that human cells degrade rapidly with only a few degrees rise in temperature.[26] Since the average thermal energy of a vibrating molecule in a solid is $3K_BT$, we can easily determine a TRE for the degrading impact of field in the membrane layer. We must remember

that the TRE is not an actual temperature rise in the specimen but it is expected to have the same degrading impact at an actual temperature rise. The TRE is given by,

$$3K_B(\Delta T)_{equivalent} = \Delta U = (34.2e\text{Å})E_{ext} \tag{21}$$

where K_b is Boltzmann's constant equal to $8.62\times10^{-5} eV/K$.

In Fig. 14, we show the TRE for various external fields. Note that some membrane degradation is expected at an external field of 1kV/cm. For an external field of 2kV/cm, the degrading impact of field on the cell membrane is expected to have the same degrading impact as if the cell temperature actually increased by 3°C. As a check on these results, remember that the homeostasis body temperature is 37°C (98.6°F). For a body temperature rise of 3°C (5.4°F), this would produce a body temperature of 104°F. A body temperature of 104°F (40°C) is considered a medical emergency, and prolonged exposure can lead to organ damage and death.

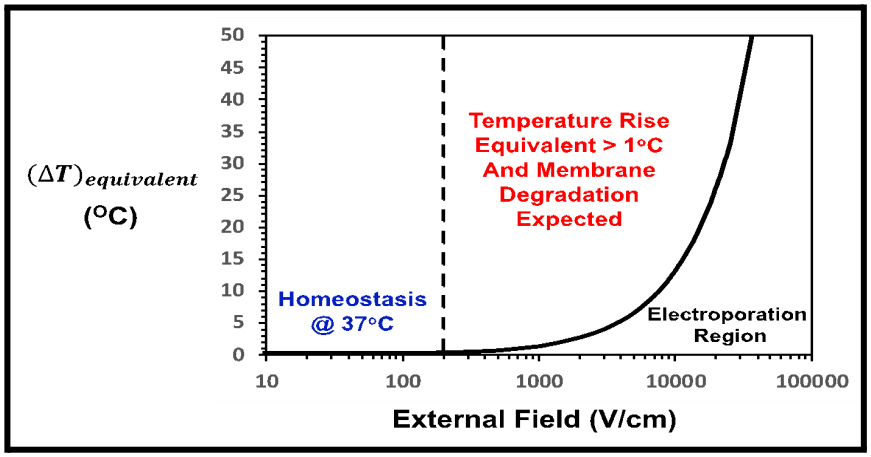

Fig. 14: Impact of external fields on cell membrane degradation in terms of effective temperature-rise equivalents (TREs).

VII. IMPACT OF EXTERNAL FIELD ON HOMEOSTASIS FIELD IN MEMBRANE

Due to electrochemical differences between cytoplasm and extra-cellular region, an electric field exists in the membrane layer in its homeostasis (natural) state, as is illustrated in Fig. 15.

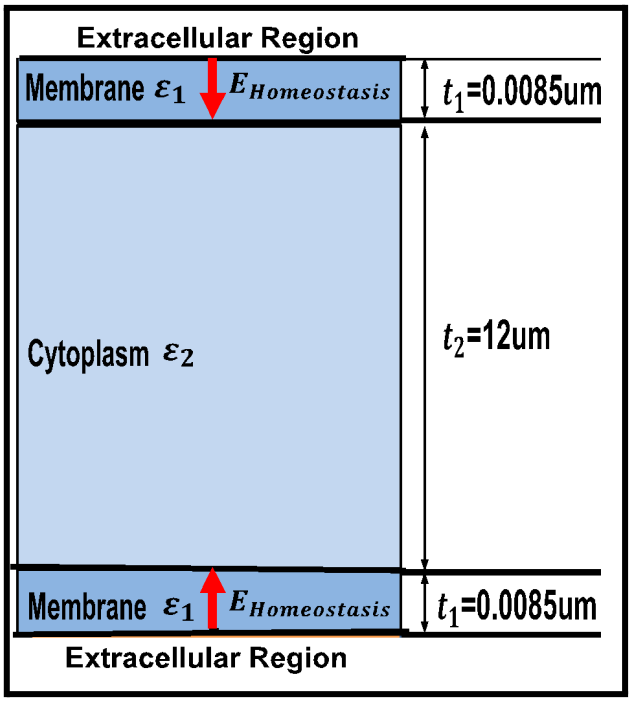

Fig. 15: Illustrates the electric field that exists in the cell membrane in the homeostasis state.

The homeostasis voltage drop is generally accepted to be approximately 70mV. Thus, this voltage drop across the 85Å membrane layer produces a homeostasis field 82.4kV/cm. Therefore, when an external unipolar voltage is applied (as illustrated in Fig. 13), the field in the membrane layer near the anode will be higher:

$$E_{Membrane} = 82.4kV/cm + 34.2E_{External} \cdot \quad (22)$$

The electric-field in the anode membrane is shown in Fig. 16. We can see that membrane damage is expected to start when the field exceeds 200V/cm.

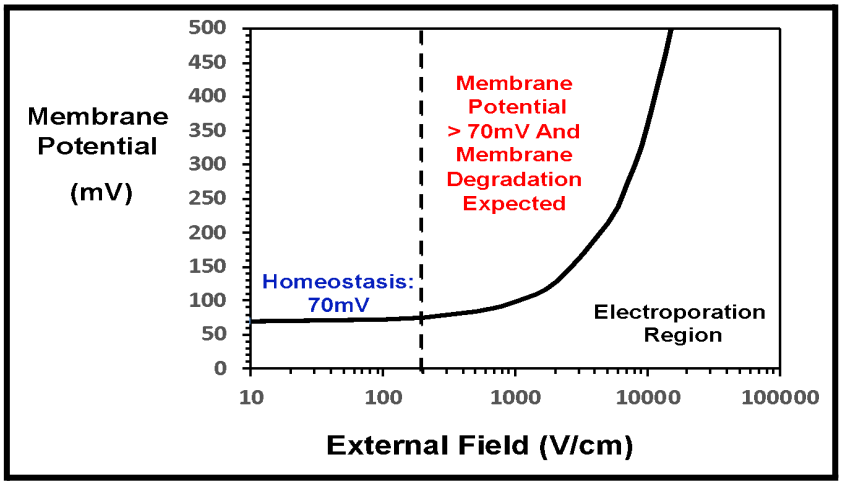

Fig. 16: Membrane potential versus applied external field. Little/no impact on homeostasis field in membrane for external fields $\leq 200V/cm$. Strong increases in membrane field above 200V/cm.

VIII. IMPACT OF ELECTRIC-FIELD PULSING

As we have shown, the dielectric constants in the layers of a cell are critically important for determining fields in each layer because the cell degradation rate is expected to be strongly dependent on the field. [27-29] The relative dielectric constant ε_r for a material depends on the polarization as given here:

$$\varepsilon_r = 1 + \frac{P/\varepsilon_0}{E_{dielectric}} \tag{23}$$

where P is the dielectric polarization (net dipole moment per unit volume). There are various types of polarization, as illustrated in the Table shown. Polarization can occur via: electron cloud shifts, molecular bond-stretching, molecular rotation, and ion drift. Each polarization type has its own characteristic response time-constant. Polarization response-time physics is very important for a good understanding of the frequency dependence of pulsed-field testing of dielectrics.

Table: Fundamental Physical-Limitations on Dielectric Response Times

Polarization Type	No Field	Field ←	Time Constant
Electron Cloud Shift	Atom 	Atom 	~ 10^{-15} s
Bond Stretching	Molecule 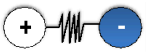	Molecule 	~ 10^{-12} s
Molecular Rotation (In Liquids)	H_2O 	H_2O 	~ 10^{-9} s
Ion Drift/Diffusion (In Solids)	Ion 	Ion 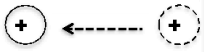 1 Lattice Constant @ 25°C	≥ 10^{-6} s

As for cell polarization, the cell membrane layer is hydrophobic and its response time is expected to be controlled by molecular distortion (bond stretching). Thus, the membrane polarization response time is expected to be fast (~picoseconds). Since the cytoplasm layer is mostly water, its response time is slower (~nanoseconds) because water molecules must rotate in order to increase the dielectric constant. Also, since the cytoplasm layer is saline-like, complete cytoplasm polarization (due to water-molecule rotation plus Na-ion and Cl-ion drift in this layer) will take much longer (~ microseconds or more).

The observed polarization response times are not quite as sharp as the table would indicate. Due to many-body physical interactions in a material, a power-law frequency model has been demonstrated to be more useful in describing the observed frequency dependence in materials. [29] This power-law dependence of ε_r is illustrated with a dashed line in Fig. 15.

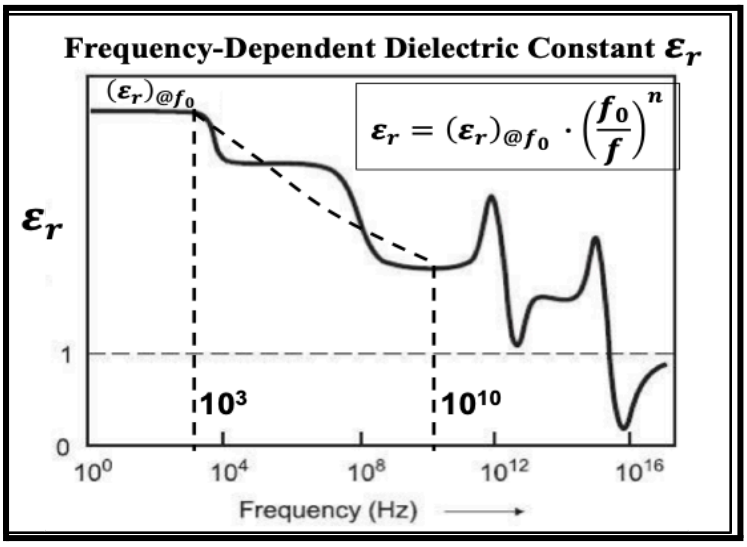

Fig. 17: The general trend shown here is a reduction in dielectric constant ε_r with frequency.

Due to many-body interactions in a solid, the observed dielectric constant (dashed line) takes on less of a lumpy appearance and more of an inverse power law dependence on frequency. [29]

The impact of all of this physics on the cell response to pulsed electric fields can now be summarized. The cell membrane can more quickly respond to electric fields than the cytoplasm. Thus, for high frequency (GHz) pulsing, the cytoplasm will have a lower dielectric constant (due to the fact that the water molecules cannot rotate fast enough). This means that the cytoplasm layer will experience higher fields and the membrane lower fields. Since cell degradation is expected to be dependent strongly on field [Figs. 14 and 16], this would imply that GHz pulsing would be expected to induce more damage in the cytoplasm layer.

For lower frequency (MHz) pulsing, water molecule rotation should be nearly complete in the cytoplasm layer and this results in a higher dielectric constant and a lower field in this layer; but, as we have shown, the higher dielectric constant in the cytoplasm layer results in a much higher field in the membrane layer. Thus, MHz pulsing is expected to produce more damage in the cell membrane layer than in the cytoplasm layer. In summary, for electric-field pulsing, high frequency (GHz) pulsing is best for producing more damage to the cell cytoplasm region and less damage to the cell membrane. Lower frequency (MHz) pulsing produces more damage to the cell membrane layer and less damage to the cell cytoplasm region.

Before leaving this section on electric-field pulsing, perhaps we should again consider the cell membrane degradation model. Only those H-bonds anti-parallel to the field will experience an accelerated degradation rate due to an unipolar pulse. On average, 50% of the H-bonds will have some degree of anti-parallelism to the field and thus a higher degradation rate. In order for the field to have an adverse impact on the other 50% of the H-bonds, perhaps bipolar pulsing would be a more efficient way of pulsing for improved cell membrane electroporation.

IX. DISCUSSION

In this work, a physics-based model for hydrogen bond (H-bond) breakage in cell membranes was developed and presented. Electroporation was interpreted through the lens of dielectric breakdown, treating the cell membrane as the critical dielectric layer in a capacitor-like system. The Cell Capacitor Dielectric (CCD) Model introduced here conceptualizes a single human cell as a dielectric system, where irreversible membrane damage occurs when dielectric breakdown thresholds are exceeded. In a static external electric field, the cytoplasm—composed primarily of water—exhibits a high relative dielectric constant ($\varepsilon \approx 70$), while the cell membrane's hydrophobic core has a much lower dielectric constant ($\varepsilon \approx 3$). This disparity means that, under static or low-frequency electric fields, the electric field strength concentrates across the membrane, making it especially vulnerable to breakdown. The CCD-Model also demonstrates that the time-dependent dielectric properties of these cellular regions play a crucial role in determining the outcome of pulsed electric fields.

At lower-frequency pulsing (on the order of megahertz), water molecules within the cytoplasm have sufficient time to reorient and achieve full polarization. This results in a peak in the dielectric constant of the cytoplasmic region, which in turn reduces the local electric field within the cytoplasm and intensifies the field across the membrane. Additionally, ion drift (particularly of Na^+ and Cl^-) induced by the electric field contributes to interface charging at the cytoplasm–membrane boundary. This further amplifies the membrane field, reinforcing the case for using MHz-range pulses in electroporation applications aimed at selectively targeting the membrane.

In contrast, at higher frequencies (in the GHz range), water molecules cannot fully reorient in response to the rapidly oscillating field. As a result, the dielectric constant of the cytoplasm decreases. This leads to an increased electric field in the cytoplasm and a relative reduction in the field across the membrane. Consequently, GHz pulsing is thought to produce more intracellular damage, potentially affecting the cytoplasmic and nucleoplasmic regions, including the nucleolus, rather than just compromising the membrane.

Finally, while this work is grounded in a purely physical modeling approach, it is important to recognize the need for cross-disciplinary efforts. For example, in the physical model presented, it was predicted and observed that external fields of ~ 1kV/cm will produce at least some cell membrane degradation. While a lower external-field electroporation process may not produce a stable pore (pore recovery is possible), this lower electric field may weaken the cell membrane to the extent that chemotherapy and/or immunotherapy is now much more effective. [31-38]

X. Summary

A physical Cell Capacitor Dielectric (CCD) Model, based on hydrogen bond (H-bond) breakage, was presented to better understand the effects of external electric fields on cell membrane degradation. This model, which treats a single human cell as a capacitor with the membrane as the dielectric layer, effectively captures a wide range of observed electroporation behaviors. Whether the membrane damage is interpreted through an effective temperature-rise or a direct electric field-induced breakdown mechanism, the CCD-Model remains consistent with experimental data. It provides a unified explanation for varying degrees of cell membrane response across different electric field strengths. Specifically, the model predicts:

Minimal or no membrane damage at field strengths below ~200 V/cm, aligning with Environmental Protection Agency (EPA) guidelines for exposure to high-voltage sources. [39]
Initial, measurable degradation of the cell membrane at field strengths around ~1 kV/cm.
Strong and irreversible membrane damage at approximately ~10 kV/cm.

Catastrophic failure of the membrane at field strengths near ~40 kV/cm.

These predictions are in good agreement with established electroporation data and widely accepted safety standards. In summary, the CCD-Model—grounded in the physics of hydrogen bond breakage—offers a useful framework for understanding how external electric fields can compromise cell membrane integrity. It provides insight not only into electroporation mechanisms but also into broader biomedical applications, potentially supporting future advances in therapeutic strategies involving electric-field exposure.

APPENDIX

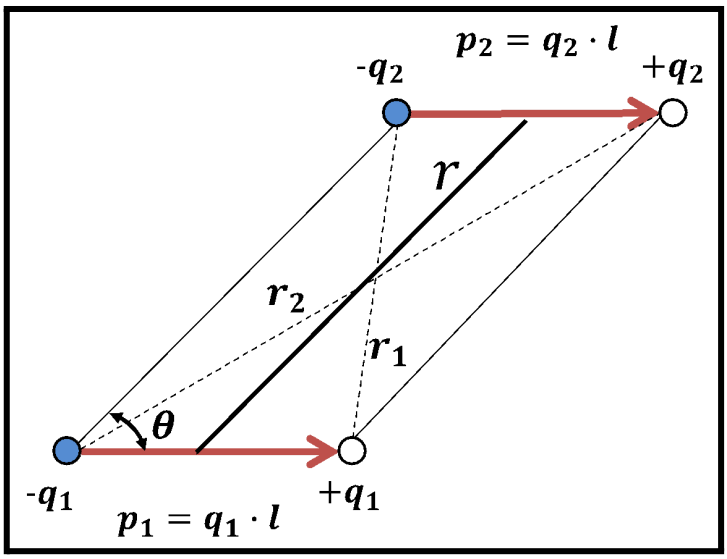

Fig. A1: Geometrical arrangement of 4 charges (two dipoles)

The potential energy of the charge distribution shown in Fig. A1 is given by:

$$U = \frac{q_1 q_2}{4\pi\varepsilon_r\varepsilon_0}\left[\frac{2}{r} - \frac{1}{r_1} - \frac{1}{r_2}\right] \quad . \tag{A1}$$

Using the geometrical properties of the parallelogram,

$$r_1 = \sqrt{l^2 + r^2 - 2lr\cos(\theta)} = r\sqrt{1-\alpha} \tag{A2}$$

where:

$$\alpha = 2\left(\frac{l}{r}\right)\cos(\theta) - \left(\frac{l}{r}\right)^2 < 1 \quad . \tag{A3}$$

Likewise,

$$r_2 = \sqrt{l^2 + r^2 - 2lr\cos(180-\theta)} = r\sqrt{1+\beta} \tag{A4}$$

where:

$$\beta = 2\left(\frac{l}{r}\right)\cos(\theta) + \left(\frac{l}{r}\right)^2 < 1 \quad . \tag{A5}$$

Rewriting Eq. (A2) and expanding in a power series through quadradic terms, we obtain

$$\frac{1}{r_1} = \frac{1}{r}\left[(1-\alpha)^{-\frac{1}{2}}\right] \cong \frac{1}{r}\left[1 + \frac{1}{2}\alpha + \frac{3}{8}\alpha^2\right]$$
$$= \frac{1}{r}\left[1 + \left(\frac{l}{r}\right)\cos(\theta) - \frac{1}{2}\left(\frac{l}{r}\right)^2 + \frac{3}{8}(4)\left(\frac{l}{r}\right)^2 cos^2(\theta)\right] \quad . \tag{A6}$$

Likewise,

$$\frac{1}{r_2} = \frac{1}{r}\left[(1+\beta)^{-1/2}\right] \cong \frac{1}{r}\left[1 + \frac{1}{2}\beta + \frac{3}{8}\beta^2\right]$$
$$= \frac{1}{r}\left[1 - \left(\frac{l}{r}\right)\cos(\theta) - \frac{1}{2}\left(\frac{l}{r}\right)^2 + \frac{3}{8}(4)\left(\frac{l}{r}\right)^2 cos^2(\theta)\right] \quad . \tag{A7}$$

Combining equations (A6) and (A7), we obtain

$$\frac{1}{r_1} + \frac{1}{r_2} = \frac{1}{r}\left[2 - \left(\frac{l}{r}\right)^2 (1 - 3cos^2\theta)\right] \quad . \tag{A8}$$

Therefore,

$$U = \frac{q_1 q_2}{4\pi\varepsilon_r\varepsilon_0}\left[\frac{2}{r} - \left(\frac{1}{r_1} + \frac{1}{r_2}\right)\right] = \frac{p_1 p_2}{4\pi\varepsilon_r\varepsilon_0 r^3}[(1 - 3cos^2\theta)] \quad . \tag{A9}$$

REFERENCES

1. Bowie, J., *Membrane protein folding: how important are the hydrogen bonds?*, Curr. Opin. Struct. Biol, 21, 42 (2011).
2. Bondar, A. and S. White, *Hydrogen bond dynamics in membrane protein function*, Biochimica et Biophysica Acta, 1818, 942 (2012).
3. Vladilo, G. and A. Hassanali, *Hydrogen bonds and life in the universe,* Life, 8, 1 (2018).
4. Pauling, L., The Nature of the Chemical Bond, 3rd Ed., Cornel University Press, 449 (1960).
5. Atkins, P., Physical Chemistry, 5th Ed., W. H. Freeman and Company, 765 (1994).
6. Coster, H.G., *A quantitative analysis of the voltage-current relationship of fixed charge membranes and the associated property of punch-through*, Biophysical J., 5, 669 (1965).
7. Zimmerman, U., G. Piwat and F. Riemann, *Dielectric breakdown of cell membranes*, Biophysical J., 14, 881 (1974).
8. Nuccitelli, R., X. Chen, A. Pakhomov, W. Baldwin and S. Sheikh, *A new pulsed electric field therapy for melanoma disrupts the tumor's blood supply and causes complete remission without recurrence*, Bioelectrics Publications, 189 (2009).
9. Kotnik, T., P. Kramar, G. Puchihar and D. Miklavcic, *Cell Membrane Electroporation – Part 1: The Phenomenon,* IEEE Electrical Insulation Magazine, Vol. 8, No.5 (2012).
10. Haberl, S. and D. Miklavcic, G. Sersa, W. Frey and B. Rubinsky, *Cell Membrane Electroporation – Part The Applications,* IEEE Electrical Insulation Magazine, Vol. 29, No.1 (2013).
11. Akiyama H. and R. Heller, Bioelectrics, Springer Publishing, Tokyo, (2017).
12. Nuccitelli, R., *Application of pulsed electric fields to cancer therapy*, Bioelectricity, 1, 30 (2019).
13. Napotnik, T., T. Polajzer and D. Miklavcic, *Cell death due to electroporation – a review*, Biochemistry, 141, 107871 (2021).
14. Rakoczy, K., M. Kisielewska, M. Sedzik, et al., *Electroporation in clinical applications – the potential of gene electrotransfer and electrochemotherapy,* Appl. Science 12, 10821 (2022).

15. Krassowska, W. and P. Filev, *Modeling electroporation in a single cell*, Biophysical Journal, 92, 404 (2007)
16. Milestone, W., C. Baker, A. Garner and R. Joshi, *Electroporation from mitochondria to cell clusters: Model development toward analyzing electrically driven bioeffects over a large special range*, Journal of Applied Physics, 133, 244701 (2023).
17. Guedert, R., D. Andrade, J. Silva, G. Pintarelli and D. Suzuki, *Dynamic model of tissue electroporation on the basis of biological dispersion and Joule heating*, J. Appl. Physics, 135, 095109 (2024).
18. Lv Yanpeng, Shihan Lu and Jianhua Zhang, *Theoretical study of discriminative electroporation effect between tumor and normal blood vessels by high frequency bipolar and traditional monopolar pulses,* J. Appl. Physics, 136, 064701 (2024).
19. McPherson, J. and H. Mogul: *Underlying physics of the thermochemical E-Model in describing low-field time-dependent dielectric breakdown in SiO_2 thin films*, J. Appl. Phys., 84, 1513 (1998).
20. McPherson, J., R. Khamankar and A. Shanware: *Complementary model for intrinsic time-dependent dielectric breakdown in SiO_2 dielectrics*, J. Appl. Physics, 88, 5351 (2000).
21. McPherson, J., J. Kim, A. Shanware, H. Mogul and J. Rodriguez: *Trends in the ultimate breakdown strength of high dielectric-constant materials*, IEEE Trans. On Elect. Devs., 50, 1771 (2003).
22. McPherson, J., *Determination of the nature of molecular bonding in silica from time-dependent dielectric breakdown data*, J. Appl. Physics, 95, 8101 (2004).
23. McPherson, J., *Time Dependent Dielectric Breakdown Physics --- Models Revisited*, Microelectronics Reliability, 52, 1753 (2012).
24. Shepherd, V., *The cytomatrix as a cooperative system of macromolecular and water networks*. Current Topics in Developmental Biology. 75, 171 (2006).
25. Gramse, G., A. Dols-Perez, M. Edwards, L. Fumagalli and G. Gomila, *Nanoscale measurement of the dielectric constant of supported lipid Bbilayers in aqueous solutions with electrostatic force microscopy,* Biophysical Journal, 104, 1257 (2013).
26. Leber, B., U. Mayrhauser, B. Leopold, S. Koestenbauer, K.Tscheliessnigg, V. Stadlbauer and P. Stiegler, *Impact of temperature on cell death in a cell-culture model of hepatocellular carcinoma,* Anticancer Research, 32, 915 (2012).
27. McPherson, J., *A generalized Gibbs potential model for materials degradation,* World Journal of Condensed Matter Physics, 14, 107 (2024).
28. McPherson, J., *Thermochemical description of dielectric breakdown in high dielectric-constant materials*, Appl. Phys. Lett., 82, 2121 (2003).
29. McPherson, J., *Physical model for the frequency dependence of time-dependent dielectric breakdown (tddb),* AIP Advances in Physics, 13, 055217 (2023).
30. Hussein, M., F. Awwad, D. Jithin, H. El Hasasna, K. Athamneh and R. Iratni, *Breast cancer cells exhibits specific dielectric signature in vitro using the open-ended coaxial probe technique from 200 MHz to 13.6 MHz,* Scientific Reports, 9, 4681 (2019).
31. Okino, M. and H. Mohri, *Effects of a high-voltage electical impulse and an anticancer drug on in vivo growing tumors*, Japan Journal Cancer Research, 78, 1319 (1987).
32. Mir, L., H. Banoun, C. Paoletti, *Introduction of definite amounts of nonpermeant molecules into living cells after electropermeabilization: direct access to the cytosol,* Experimental Cell Research, 175, 15 (1988).
33. Mir, L., M. Belehradek, C. Domenge, et al., *Electrochemotherapy, a new antitumor treatment: first clinical trial*, C R Acad Sci III, 313, 613 (1991).
34. Heller, R., MJ Jaroszeski, DS Reintgen, et al., *Treatment of cutaneous and subcutaneous tumors with electrochemotherapy using intralesional bleomycin*. Cancer, 83, 148 (1998).
35. Gehl, J., *Electroporation for drug and gene delivery in the clinic: doctors go electric*, Methods Mol. Biol., 423, 351 (2008).

36. Matthiessen, L., RL Chalmers, DC Sainsbury, et al., *Management of cutaneous metastases using electrochemotherapy*, Acta Oncol, 50, 621 (2011).
37. Miklavcic, D., G. Serva, E. Brecelj,et al., *Electrochemotherapy: technological advancements for efficient electroporation-based treatments of internal tumors*, Med Biol Eng Comput, 50, 1213 (2012).
38. Gehl, J., G. Sersa, L. Matthiessen, et al., *Updated standard operating procedures for electochemotherapy of cultaneous tumors and skin metastases*, Acta Oncol., 57, 874 (2018).
39. Environmental Protection Agency (EPA), *Guidelines for Electric Fields Under Power Lines*, Technical Note ORP/EAD 80-1.

This page is intentionally left blank

The Geometry of the Universe: In search of unity. New Possible Mathematical Connections with the DN Constant, Ramanujan's Recurring Numbers and Some parameters of Number Theory and String Theory

Michele Nardelli

Università degli Studi di Napoli

ABSTRACT

In this work, we analyze the DN Constant (Del Gaudio-Nardelli Constant). We will describe the possible mathematical connections with Ramanujan's Recurring Numbers, some parameters of Number Theory and String Theory.

Keywords: NA

Classification: LCC Code: QA351

Language: English

Great Britain Journals Press

LJP Copyright ID: 925662
Print ISSN: 2631-8490
Online ISSN: 2631-8504

London Journal of Research in Science: Natural & Formal

Volume 25 | Issue 6 | Compilation 1.0

The Geometry of the Universe: In search of unity. New Possible Mathematical Connections with the DN Constant, Ramanujan's Recurring Numbers and Some parameters of Number Theory and String Theory

Michele Nardelli

ABSTRACT

In this work, we analyze the DN Constant (Del Gaudio-Nardelli Constant). We will describe the possible mathematical connections with Ramanujan's Recurring Numbers, some parameters of Number Theory and String Theory

Author: Nardelli studied at Dipartimento di Scienze della Terra Università degli Studi di Napoli Federico II, Largo S. Marcellino, 10 - 80138 Napoli, Dipartimento di Matematica ed Applicazioni "R. Caccioppoli" - Università degli Studi di Napoli "Federico II" – Polo delle Scienze e delle Tecnologie Monte S. Angelo, Via Cintia (Fuorigrotta), 80126 Napoli, Italy.

I. DN CONSTANT

What is DN Constant (Del Gaudio-Nardelli Constant)?

The ratio of the volume of an octahedron to the volume of a sphere

$$V_o = \frac{1}{3}\cdot\sqrt{2}\cdot a^3 \; ; \quad V_s = \frac{4}{3}\cdot\pi\cdot\left(\frac{a}{2}\right)^3$$

is given by the following formula:

$$\frac{V_o}{V_s} = \frac{\frac{1}{3}\cdot\sqrt{2}\cdot a^3}{\frac{4}{3}\cdot\pi\cdot\left(\frac{a}{2}\right)^3} = \frac{2\sqrt{2}}{\pi} = 0.9003163161571\ldots = DN\ Constant$$

Multiplying the ratio described above by 3, and taking the square root, we obtain:

$$\sqrt{3\left(\frac{\frac{1}{3}\cdot\sqrt{2}\cdot a^3}{\frac{4}{3}\cdot\pi\cdot\left(\frac{a}{2}\right)^3}\right)} = 1.64345640297\ldots \approx \zeta(2) = \frac{\pi^2}{6}$$

London Journal of Research in Science: Natural & Formal

Indeed:

$$\sqrt{3\times\frac{\frac{1}{3}\sqrt{2}\,a^3}{\frac{4}{3}\pi\left(\frac{a}{2}\right)^3}}$$

Exact result

$$2^{3/4}\sqrt{\frac{3}{\pi}}$$

Decimal approximation

1.6434564029725…≈ $\zeta(2) = \pi^2/6 = 1.644934$ (trace of the instanton shape and Ramanujan Recurring Number)

Property

$$2^{3/4}\sqrt{\frac{3}{\pi}}$$

Series representations

$$\sqrt{\frac{3\left(\sqrt{2}\,a^3\right)}{\frac{3}{3}\left(4\,\pi\left(\frac{a}{2}\right)^3\right)}}=\sqrt{-1+\frac{6\sqrt{2}}{\pi}}\sum_{k=0}^{\infty}\binom{\frac{1}{2}}{k}\left(-1+\frac{6\sqrt{2}}{\pi}\right)^{-k}$$

$$\sqrt{\frac{3\left(\sqrt{2}\,a^3\right)}{\frac{3}{3}\left(4\,\pi\left(\frac{a}{2}\right)^3\right)}}=\sqrt{-1+\frac{6\sqrt{2}}{\pi}}\sum_{k=0}^{\infty}\frac{(-1)^k\left(-\frac{1}{2}\right)_k\left(-1+\frac{6\sqrt{2}}{\pi}\right)^{-k}}{k!}$$

$$\sqrt{\frac{3\left(\sqrt{2}\,a^3\right)}{\frac{3}{3}\left(4\,\pi\left(\frac{a}{2}\right)^3\right)}}=\sqrt{z_0}\sum_{k=0}^{\infty}\frac{(-1)^k\left(-\frac{1}{2}\right)_k\left(\frac{6\sqrt{2}}{\pi}-z_0\right)^k z_0^{-k}}{k!}$$

for $(\text{not}\,(z_0\in\mathbb{R}\ \text{and}\ -\infty<z_0\le 0))$

Multiplying the above expression by 6, and taking the square root, we obtain:

$$\sqrt{6\sqrt{3\left(\frac{\frac{1}{3}\cdot\sqrt{2}\cdot a^3}{\frac{4}{3}\cdot\pi\cdot\left(\frac{a}{2}\right)^3}\right)}} = 3.14018127149294\ldots \approx \pi$$

Indeed:

$$\sqrt{6\sqrt{3\times\frac{\frac{1}{3}\sqrt{2}\,a^3}{\frac{4}{3}\pi\left(\frac{a}{2}\right)^3}}}$$

Exact result

$$\frac{2^{7/8}\times 3^{3/4}}{\sqrt[4]{\pi}}$$

Decimal approximation

3.14018127149294...≈ π (Ramanujan Recurring Number)

Property

$\frac{2^{7/8}\times 3^{3/4}}{\sqrt[4]{\pi}}$ is a transcendental number

Series representations

$$\sqrt{6\sqrt{\frac{3\left(\sqrt{2}\,a^3\right)}{\frac{3}{3}\left(4\,\pi\left(\frac{a}{2}\right)^3\right)}}} = \frac{2^{3/8}\times 3^{3/4}}{\sqrt[4]{\sum_{k=0}^{\infty}\frac{(-1)^k}{1+2k}}}$$

$$\sqrt{6\sqrt{\frac{3\left(\sqrt{2}\,a^3\right)}{\frac{3}{3}\left(4\,\pi\left(\frac{a}{2}\right)^3\right)}}} = \frac{2^{7/8}\times 3^{3/4}}{\sqrt[4]{\sum_{k=0}^{\infty}\left(-\frac{1}{4}\right)^k\left(\frac{1}{1+2k}+\frac{2}{1+4k}+\frac{1}{3+4k}\right)}}$$

$$\sqrt{6\sqrt{\frac{3\left(\sqrt{2}\,a^3\right)}{\frac{3}{3}\left(4\,\pi\left(\frac{a}{2}\right)^3\right)}}}=\frac{2^{3/8}\times 3^{3/4}}{\sqrt[4]{\sum_{k=0}^{\infty}\frac{(-1)^{1+k}\,1195^{-1-2\,k}\left(5^{1+2\,k}-4\times 239^{1+2\,k}\right)}{1+2\,k}}}$$

Integral representations

$$\sqrt{6\sqrt{\frac{3\left(\sqrt{2}\,a^3\right)}{\frac{3}{3}\left(4\,\pi\left(\frac{a}{2}\right)^3\right)}}}=\frac{2^{3/8}\times 3^{3/4}}{\sqrt[4]{\int_0^1\sqrt{1-t^2}\,dt}}$$

$$\sqrt{6\sqrt{\frac{3\left(\sqrt{2}\,a^3\right)}{\frac{3}{3}\left(4\,\pi\left(\frac{a}{2}\right)^3\right)}}}=\frac{2^{5/8}\times 3^{3/4}}{\sqrt[4]{\int_0^{\infty}\frac{1}{1+t^2}\,dt}}$$

$$\sqrt{6\sqrt{\frac{3\left(\sqrt{2}\,a^3\right)}{\frac{3}{3}\left(4\,\pi\left(\frac{a}{2}\right)^3\right)}}}=\frac{2^{5/8}\times 3^{3/4}}{\sqrt[4]{\int_0^1\frac{1}{\sqrt{1-t^2}}\,dt}}$$

Finally carrying out the following calculations, which include the above expression, we obtain:

$$\sqrt[2\pi]{\frac{1}{4}\left(\sqrt{6\sqrt{3\left(\frac{\frac{1}{3}\cdot\sqrt{2}\cdot a^3}{\frac{4}{3}\cdot\pi\cdot\left(\frac{a}{2}\right)^3}\right)}\left(5\left(3+\sqrt{5}\right)\right)}\right)}=1.61789283408194\ldots\approx\phi=\frac{\sqrt{5}+1}{2}=1.61803398\ldots$$

practically, a value very close to the Golden Ratio.

Indeed:

$$\sqrt[2\,\pi]{\frac{1}{4}\left(\sqrt{6\sqrt{3\times\frac{\frac{1}{3}\sqrt{2}\,a^3}{\frac{4}{3}\,\pi\left(\frac{a}{2}\right)^3}}\left(5\left(3+\sqrt{5}\right)\right)}\right)}$$

Exact result

$$2^{-9/(16\pi)} \times 3^{3/(8\pi)} \sqrt[2\pi]{5\left(3+\sqrt{5}\right)}\ \pi^{-1/(8\pi)}$$

Decimal approximation

1.61789283408194…. result that is a very good approximation to the value of the golden ratio 1.618033988749… (Ramanujan Recurring Number)

Series representations

$$\sqrt[2\pi]{\frac{1}{4}\sqrt{6\sqrt{\frac{3\left(\sqrt{2}\,a^3\right)}{\frac{3}{3}\left(4\pi\left(\frac{a}{2}\right)^3\right)}}}\ \left(5\left(3+\sqrt{5}\right)\right)} = 2^{-1/\pi}\sqrt[2\pi]{5}$$

$$\sqrt[2\pi]{\sqrt{-1+6\sqrt{\frac{6\sqrt{2}}{\pi}}}\ \left(3+\sqrt{4}\sum_{k=0}^{\infty}4^{-k}\left(\frac{\frac{1}{2}}{k}\right)\right)\sum_{k=0}^{\infty}\left(\frac{\frac{1}{2}}{k}\right)\left(-1+6\sqrt{\frac{6\sqrt{2}}{\pi}}\right)^{-k}}$$

$$\sqrt[2\pi]{\frac{1}{4}\sqrt{6\sqrt{\frac{3\left(\sqrt{2}\,a^3\right)}{\frac{3}{3}\left(4\pi\left(\frac{a}{2}\right)^3\right)}}}\ \left(5\left(3+\sqrt{5}\right)\right)} =$$

$$2^{-1/\pi}\sqrt[2\pi]{5}\left(\sqrt{-1+6\sqrt{\frac{6\sqrt{2}}{\pi}}}\ \left(3+\sqrt{4}\sum_{k=0}^{\infty}\frac{\left(-\frac{1}{4}\right)^k\left(-\frac{1}{2}\right)_k}{k!}\right)\right.$$
$$\left.\sum_{k=0}^{\infty}\frac{(-1)^k\left(-\frac{1}{2}\right)_k\left(-1+6\sqrt{\frac{6\sqrt{2}}{\pi}}\right)^{-k}}{k!}\right)\wedge\left(\frac{1}{2\pi}\right)$$

$$\sqrt[2\pi]{\frac{1}{4}\sqrt{6\sqrt{\frac{3\left(\sqrt{2}\,a^3\right)}{\frac{3}{3}\left(4\,\pi\left(\frac{a}{2}\right)^3\right)}}}}\left(5\left(3+\sqrt{5}\right)\right) =$$

$$2^{-1/\pi}\,\sqrt[2\pi]{5}\left(\sqrt{z_0}\left(3+\sqrt{z_0}\sum_{k=0}^{\infty}\frac{(-1)^k\left(-\frac{1}{2}\right)_k\left(5-z_0\right)^k z_0^{-k}}{k!}\right)\right.$$

$$\left.\sum_{k=0}^{\infty}\frac{(-1)^k\left(-\frac{1}{2}\right)_k\left(6\sqrt{\frac{6\sqrt{2}}{\pi}}-z_0\right)^k z_0^{-k}}{k!}\right)^{\wedge}\left(\frac{1}{2\pi}\right)$$

for (not ($z_0 \in \mathbb{R}$ and $-\infty < z_0 \leq 0$))

Integral representation

$$(1+z)^a = \frac{\int_{-i\infty+\gamma}^{i\infty+\gamma}\frac{\Gamma(s)\,\Gamma(-a-s)}{z^s}\,ds}{(2\pi i)\,\Gamma(-a)} \quad \text{for } (0 < \gamma < -\mathrm{Re}(a) \text{ and } |\arg(z)| < \pi)$$

The relationship between the volume of an octahedron and the volume of a sphere is an interesting mathematical topic. Let's see how it is calculated:

Volume of the Octahedron (V_0):

The octahedron is a polyhedron with 8 triangular faces. If (a) represents the length of one side of the octahedron, then its volume is given by:

$$[\ V_o = \frac{1}{3}\cdot\sqrt{2}\cdot a^3\ ]$$

Volume of the Sphere (V_s): The sphere has a radius (r = a/2). Its volume is given by:

$$[\ V_s = \frac{4}{3}\cdot\pi\cdot\left(\frac{a}{2}\right)^3\ ]$$

Volume ratio: the volume ratio is therefore:

$$\frac{\frac{1}{3}\cdot\sqrt{2}\cdot a^3}{\frac{4}{3}\cdot\pi\cdot\left(\frac{a}{2}\right)^3} = \frac{2\sqrt{2}}{\pi}$$

This ratio is known as the **Del Gaudio-Nardelli (DN) constant**. Its approximate value is (0.9003163161571). From this formula, we can obtain easily also 4096, where $4096 = 64^2 = 8^4 = 2^{12}$, that is a fundamental Ramanujan number and appears in the fundamental work of Srinivasa Ramanujan: "Modular Equations and Approximations to Pi". We obtain also 1729, the so-called Hardy-Ramanujan number, that is a Taxicab Number. Ramanujan said: "it is a very interesting number; it is the smallest number expressible as the sum of two cubes in two different ways.". Indeed, $1729 = 1^3 + 12^3 = 10^3 + 9^3$. These numbers are also connected to some parameters of String Theory [1] [2]

II. OTHER RELATIONSHIPS

Multiplying the above ratio by 3 and calculating the square root, we get:

$$\sqrt{3\left(\frac{\frac{1}{3}\cdot\sqrt{2}\cdot a^3}{\frac{4}{3}\cdot\pi\cdot\left(\frac{a}{2}\right)^3}\right)} = 1.64345640297\ldots \approx \zeta(2) = \frac{\pi^2}{6}$$

Multiplying the above ratio by 6 and calculating the square root, we get:

$$\sqrt{6\sqrt{3\left(\frac{\frac{1}{3}\cdot\sqrt{2}\cdot a^3}{\frac{4}{3}\cdot\pi\cdot\left(\frac{a}{2}\right)^3}\right)}} = 3.14018127149294\ldots \approx \pi$$

Finally, combining these relations, we get:

$$\sqrt[2\pi]{\frac{1}{4}\left(\sqrt{6\sqrt{3\left(\frac{\frac{1}{3}\cdot\sqrt{2}\cdot a^3}{\frac{4}{3}\cdot\pi\cdot\left(\frac{a}{2}\right)^3}\right)}}\left(5\left(3+\sqrt{5}\right)\right)\right)} = 1.61789283408194\ldots \approx \phi = \frac{\sqrt{5}+1}{2} =$$

1.61803398....

These results are fascinating and connect the octahedron, the sphere and the constant (phi), also known as the Golden Ratio.

III. EXTENDED DN CONSTANT

We have the following expression concerning the ratios (and/or inverses) between the volumes of the icosahedron, octahedron, tetrahedron and the volume of the sphere:

$$\sqrt[2\pi]{\frac{\frac{5}{12}(3+\sqrt{5})d^3}{\frac{4}{3}\pi\left(\frac{d}{2}\right)^3}\times\frac{1}{\frac{\frac{1}{3}\sqrt{2}a^3}{\frac{4}{3}\pi\left(\frac{a}{2}\right)^3}}\times\frac{1}{\frac{\sqrt{2}}{12}d^3\cdot\frac{1}{\frac{4}{3}\pi\left(\frac{d}{2}\right)^3}}}$$

(in the formula we have highlighted the DN Constant in blue)

The exact result of the above formula is:

$$2^{-1/\pi}\sqrt[2\pi]{5(3+\sqrt{5})\pi}=1.6180085459000107\ldots$$

Indeed:

$$\sqrt[2\pi]{\frac{\frac{5}{12}\left(3+\sqrt{5}\right)d^3}{\frac{4}{3}\pi\left(\frac{d}{2}\right)^3}\times\frac{1}{\frac{\frac{1}{3}\sqrt{2}\,a^3}{\frac{4}{3}\pi\left(\frac{a}{2}\right)^3}}\times\frac{1}{\frac{\sqrt{2}}{12}d^3\times\frac{1}{\frac{4}{3}\pi\left(\frac{d}{2}\right)^3}}}$$

Exact result

$$2^{-1/\pi}\sqrt[2\pi]{5\left(3+\sqrt{5}\right)\pi}$$

Decimal approximation

1.6180085459… result that is a very good approximation to the value of the golden ratio 1.618033988749… (Ramanujan Recurring Number)

Alternate form

$$2^{-1/\pi}\sqrt[2\pi]{\left(15+5\sqrt{5}\right)\pi}$$

Series representations

$$\sqrt[2\pi]{\frac{5\left(3+\sqrt{5}\right)d^3}{\frac{\left(\left(\sqrt{2}\,a^3\right)\left(\sqrt{2}\,d^3\right)\right)12\left(4\pi\left(\frac{d}{2}\right)^3\right)}{\left(\left(3\left(4\pi\left(\frac{a}{2}\right)^3\right)\right)\left(12\left(4\pi\left(\frac{d}{2}\right)^3\right)\right)\right)3}}}{}_{3\times3} = \sqrt[2\pi]{\frac{5}{2}}\sqrt[2\pi]{\frac{\pi\left(3+\sqrt{z_0}\ \sum_{k=0}^{\infty}\frac{(-1)^k\left(-\frac{1}{2}\right)_k(5-z_0)^k\,z_0^{-k}}{k!}\right)}{\sqrt{z_0}^{\,2}\left(\sum_{k=0}^{\infty}\frac{(-1)^k\left(-\frac{1}{2}\right)_k(2-z_0)^k\,z_0^{-k}}{k!}\right)^2}}$$

for (not ($z_0 \in \mathbb{R}$ and $-\infty < z_0 \leq 0$))

$$\sqrt[2\pi]{\frac{5\left(3+\sqrt{5}\right)d^3}{\frac{\left(\left(\sqrt{2}\,a^3\right)\left(\sqrt{2}\,d^3\right)\right)12\left(4\pi\left(\frac{d}{2}\right)^3\right)}{\left(\left(3\left(4\pi\left(\frac{a}{2}\right)^3\right)\right)\left(12\left(4\pi\left(\frac{d}{2}\right)^3\right)\right)\right)3}}}{}_{3\times3} =$$

$$\sqrt[2\pi]{\frac{5}{2}}\sqrt[2\pi]{\frac{\pi\left(3+\exp\left(i\,\pi\left\lfloor\frac{\arg(5-x)}{2\pi}\right\rfloor\right)\sqrt{x}\ \sum_{k=0}^{\infty}\frac{(-1)^k(5-x)^k\,x^{-k}\left(-\frac{1}{2}\right)_k}{k!}\right)}{\exp^2\left(i\,\pi\left\lfloor\frac{\arg(2-x)}{2\pi}\right\rfloor\right)\sqrt{x}^{\,2}\left(\sum_{k=0}^{\infty}\frac{(-1)^k(2-x)^k\,x^{-k}\left(-\frac{1}{2}\right)_k}{k!}\right)^2}}$$

for ($x \in \mathbb{R}$ and $x < 0$)

$$\sqrt[2\pi]{\frac{5\left(3+\sqrt{5}\right)d^3}{\frac{\left(\left(\sqrt{2}\,a^3\right)\left(\sqrt{2}\,d^3\right)\right)12\left(4\pi\left(\frac{d}{2}\right)^3\right)}{\left(\left(3\left(4\pi\left(\frac{a}{2}\right)^3\right)\right)\left(12\left(4\pi\left(\frac{d}{2}\right)^3\right)\right)\right)3}}}{}_{3\times3} =$$

$$\sqrt[2\pi]{\frac{5}{2}}\left(\left(\pi\left(\frac{1}{z_0}\right)^{-\lfloor\arg(2-z_0)/(2\pi)\rfloor}z_0^{-1-\lfloor\arg(2-z_0)/(2\pi)\rfloor}\left(3+\left(\frac{1}{z_0}\right)^{1/2\lfloor\arg(5-z_0)/(2\pi)\rfloor}z_0^{1/2+1/2\lfloor\arg(5-z_0)/(2\pi)\rfloor}\sum_{k=0}^{\infty}\frac{(-1)^k\left(-\frac{1}{2}\right)_k(5-z_0)^k\,z_0^{-k}}{k!}\right)\right)\Big/\left(\sum_{k=0}^{\infty}\frac{(-1)^k\left(-\frac{1}{2}\right)_k(2-z_0)^k\,z_0^{-k}}{k!}\right)^2\right)\wedge\left(\frac{1}{2\pi}\right)$$

Indeed:

$$\frac{4\times 1.6180085459001 07^{2\pi}}{5\left(3+\sqrt{5}\right)}$$

Result

3.14159265358979…

3.14159265358979…= π (Ramanujan Recurring Number)

Series representations

$$\frac{4\times 1.6180085459001070000^{2\pi}}{5\left(3+\sqrt{5}\right)}=\frac{4\,e^{0.9623922007800638614\,\pi}}{5\left(3+\sqrt{4}\,\sum_{k=0}^{\infty}4^{-k}\binom{\frac{1}{2}}{k}\right)}$$

Indeed:

$$\frac{4\times 1.6180085459001 07^{2\pi}}{5\left(3+\sqrt{5}\right)}$$

Indeed:

$$\frac{1}{6}\left(\frac{4\times 1.6180085459001 07^{2\pi}}{5\left(3+\sqrt{5}\right)}\right)^2$$

Result

1.64493406684823……≈ ζ(2) = $\pi^2/6$ = 1.644934 (trace of the instanton shape and Ramanujan Recurring Number)

Series representations

$$\frac{1}{6}\left(\frac{4\times 1.6180085459001070000^{2\pi}}{5\left(3+\sqrt{5}\right)}\right)^2=\frac{8\,e^{1.9247844015601277229\,\pi}}{75\left(3+\sqrt{4}\,\sum_{k=0}^{\infty}4^{-k}\binom{\frac{1}{2}}{k}\right)^2}$$

$$\frac{1}{6}\left(\frac{4\times 1.6180085459001070000^{2\pi}}{5\left(3+\sqrt{5}\right)}\right)^2=\frac{8\,e^{1.9247844015601277229\,\pi}}{75\left(3+\sqrt{4}\,\sum_{k=0}^{\infty}\frac{\left(-\frac{1}{4}\right)^k\left(-\frac{1}{2}\right)_k}{k!}\right)^2}$$

$$\frac{1}{6}\left(\frac{4\times 1.6180085459001070000^{2\pi}}{5\left(3+\sqrt{5}\right)}\right)^2=\frac{32\,e^{1.9247844015601277229\,\pi}\,\sqrt{\pi}^{\,2}}{75\left(6\sqrt{\pi}+\sum_{j=0}^{\infty}\operatorname{Res}_{s=-\frac{1}{2}+j}4^{-s}\,\Gamma\left(-\frac{1}{2}-s\right)\Gamma(s)\right)^2}$$

The expression regarding the relationships between the volumes of the icosahedron, the octahedron, the tetrahedron and the volume of the sphere is fascinating! Let's break it down step by step:

1. Icosahedron and Octahedron

The icosahedron has a surface made up of 20 regular triangular faces. Its volume is given by the formula: [$V = \frac{5}{12}\left(3+\sqrt{5}\right)d^3$]

The octahedron has a surface composed of 8 regular triangular faces. Its volume is given by the formula: [$V = \frac{1}{3}\sqrt{2}a^3$]

2. Ratio between volumes

The ratio between the volumes is given by the following expression:

$$\sqrt[2\pi]{\frac{\frac{5}{12}\left(3+\sqrt{5}\right)d^3}{\frac{4}{3}\pi\left(\frac{d}{2}\right)^3}\times\frac{1}{\frac{\frac{1}{3}\sqrt{2}a^3}{\frac{4}{3}\pi\left(\frac{a}{2}\right)^3}}\times\frac{1}{\frac{\sqrt{2}}{12}d^3\cdot\frac{1}{\frac{4}{3}\pi\left(\frac{d}{2}\right)^3}}}$$

3. Del Gaudio-Nardelli Constant (DN):

The DN constant is highlighted in blue in the formula. The exact result of this expression is: $[2^{-1/\pi}\sqrt[2\pi]{5\left(3+\sqrt{5}\right)\pi}=1.618008545900107]$

4. Other relationships:

From the previous formula, we obtain:

$$\frac{4 \times 1.6180085459001 07^{2\pi}}{5\left(3+\sqrt{5}\right)} = 3.141592653589 \ldots = \pi$$

Also, calculating

$$\frac{1}{6}\left(\frac{4 \times 1.6180085459001 07^{2\pi}}{5\left(3+\sqrt{5}\right)}\right)^2 = 1.64493406684823\ldots \approx \zeta(2) = \frac{\pi^2}{6}$$

we obtain a very good approximation to $\zeta(2) = \frac{\pi^2}{6}$.

These results link the geometry of the Platonic solids with the golden constant (ϕ) and the constant (π).

IV. PROPOSAL

Taking into account that a sphere is contained in an octahedron and the above results, it is hypothesized, in an "Eternal Inflation" type cosmology, that the octahedron represents a phase in which the Universe is highly symmetrical and with very low entropy, and the sphere represents the bubble Universe that emerges from the perturbations of the quantum vacuum. The relationship between the two volumes is, as we have described, equal to the DN Constant, which therefore plays a key role in the geometry of the Universe, a sort of "bridge" between geometry and physics, even before the phase of the so-called Big Bang.

The idea that the octahedron and the sphere could represent different phases of the Universe in an “Eternal Inflation” cosmology is fascinating.

Let's further explore this connection between geometry and physics:

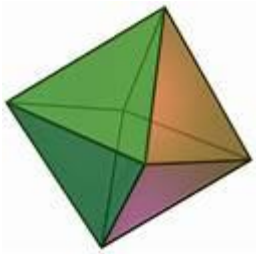

1. The Octahedron and the Symmetrical Universe

The octahedron, with its 8 triangular faces, could represent an initial phase of the Universe characterized by very high symmetry and very low entropy.

During this phase, the Universe may be highly ordered and uniform, with regular geometric structures.

2. The Sphere and the Bubble Universe

The sphere, contained in the octahedron, could represent a transition towards a different phase.

This sphere could symbolize the bubble Universe that emerges from the perturbations of the quantum vacuum.

Quantum fluctuations may have given rise to regions of different densities, creating expanding bubbles of space-time.

3. The Relationship between Volumes and DN Constant

The ratio between the volume of the octahedron and the volume of the sphere is equal to the Del Gaudio-Nardelli Constant (DN).

This constant, which we calculated previously, could play a key role in the geometry of the Universe.

It could be a "bridge" between the geometric structure and the physical laws that govern the Universe.

4. Before the Big Bang

The idea that the DN Constant is relevant even before the Big Bang phase suggests that geometry and physics are closely intertwined.

Perhaps symmetry and geometric regularity played a fundamental role in the early phases of the Universe.

Ultimately, this connection between geometric solids, mathematical constants and cosmology invites us to further explore the mysteries of the Universe and seek a deeper integration between geometry and physics.

But let's see what the cosmological implications could be in an "eternal inflation" type scenario of these formulas, results and, above all, of the DN Constant (Del Gaudio-Nardelli Constant).

Eternal inflation is a model of cosmological inflation predicted by some extensions of the Big Bang theory and the standard model of cosmology.

Let's explore the implications of this model, along with the formulas and results associated with the Del Gaudio-Nardelli Constant (DN):

1. Eternal Inflation and Multiverse

Eternal inflation suggests that the accelerated expansion of the universe due to inflation continues forever, at least in some regions.

These regions expand at exponential rates, leading to the indefinite increase in the volume of the universe.

This model predicts the existence of multiple universes, often called a multiverse. Each “bubble” of space-time could represent a separate universe.

2. Bubble Theory

The bubble theory is part of the multiverse elaborations.

According to this theory, our universe is just one of infinite “bubbles” that emerge from the quantum foam of a “parent universe” or from a single Big Bang.

These bubbles expand at different rates and may have different physical constants.

3. Connection with DN Constant

The DN Constant (Del Gaudio-Nardelli Constant) is present in the formulas that connect the volumes of geometric solids such as the octahedron and the sphere.

This constant could play a key role in the geometry of the Universe.

It could be a "bridge" between the geometric structure and the physical laws that govern the Universe.

4. Experimental checks

Some experimental evidence could transform the inflationary universe hypothesis into a verified theory.

If theoretical calculations based on DN Constant and bubble theory were experimentally confirmed, this would support the idea of an eternal multiverse.

In summary, eternal inflation and DN Constant open new perspectives on the connection between geometry, physics and the origin of the Universe. These concepts challenge us to further explore cosmological mysteries and better understand our reality.

We will explore the image of the Universe in relation to the concepts of eternal inflation, bubble theory and the Del Gaudio-Nardelli Constant (DN).

1. Eternal Inflation and Multiverse

Eternal inflation suggests that the accelerated expansion of the Universe due to inflation continues forever, at least in some regions.

We imagine a vast cosmic space in which new "bubbles" of space-time are constantly forming.

Each bubble could represent a separate universe, with different physical laws and different constants.

2. Bubble Theory

The bubble theory is part of the multiverse elaborations.

Each "bubble" represents a space-time with unique characteristics.

These bubbles emerge from the quantum foam of a "parent universe" or from a single Big Bang.

3. Connection with DN Constant

The Del Gaudio-Nardelli Constant (DN) is present in the formulas that connect the volumes of geometric solids such as the octahedron and the sphere.

This constant could be a "bridge" between the geometric structure and the physical laws of the Universe.

Let's imagine the DN as a thread that connects the different bubbles of the multiverse.

1. Image of the Universe:

We visualize a vast space in which each bubble represents a universe.

Each bubble has different geometry, different physical constants and different laws.

These bubbles expand, collide and overlap in the great cosmic landscape.

In summary, the image of the Universe in a context of eternal inflation is that of a multiversal fabric, with bubbles of reality that form, expand and intertwine infinitely. This concept challenges us to explore the depths of the Universe and understand its complexity.

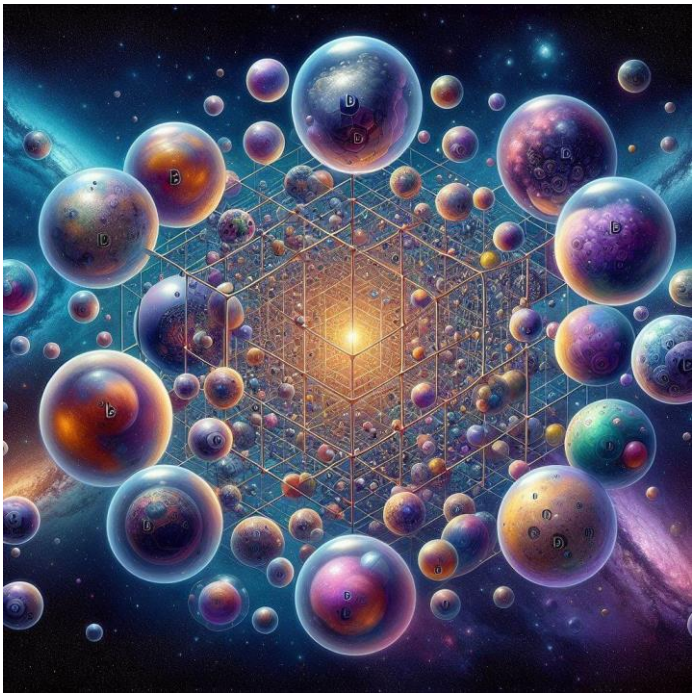

Fig. 1

A representation of the universe incorporating the concepts of eternal inflation, octahedron, sphere, and the Del Gaudio-Nardelli (DN) Constant. In the image, the different bubbles represent separate universes, each with its own geometry and physical laws. The DN Constant connects these different realities, creating a mathematical tapestry in the vast cosmic landscape

V. FURTHER DEVELOPMENTS OF THE EXTENDED DN CONSTANT

We have the following extended DN Constant:

$$\sqrt[2\pi]{\frac{\frac{5}{12}\left(3+\sqrt{5}\right)d^3}{\frac{4}{3}\pi\left(\frac{d}{2}\right)^3}\times\frac{1}{\frac{\frac{1}{3}\sqrt{2}a^3}{\frac{4}{3}\pi\left(\frac{a}{2}\right)^3}}\times\frac{1}{\frac{\sqrt{2}}{12}d^3\cdot\frac{1}{\frac{4}{3}\pi\left(\frac{d}{2}\right)^3}}}$$

and the following Cardano formula:

$$y=\sqrt[3]{-\frac{q}{2}+\sqrt{\frac{q^2}{4}+\frac{p^3}{27}}}+\sqrt[3]{-\frac{q}{2}-\sqrt{\frac{q^2}{4}+\frac{p^3}{27}}}$$

Multiplying both the above formulas, we obtain:

$$\sqrt[2\pi]{\frac{\frac{5}{12}\left(3+\sqrt{5}\right)d^3}{\frac{4}{3}\pi\left(\frac{d}{2}\right)^3}\times\frac{1}{\frac{\frac{1}{3}\sqrt{2}\,a^3}{\frac{4}{3}\pi\left(\frac{a}{2}\right)^3}}\times\frac{1}{\frac{\sqrt{2}}{12}d^3\times\frac{1}{\frac{4}{3}\pi\left(\frac{d}{2}\right)^3}}}\left(\sqrt[3]{-\frac{q}{2}+\sqrt{\frac{q^2}{4}+\frac{p^3}{27}}}+\sqrt[3]{-\frac{q}{2}-\sqrt{\frac{q^2}{4}+\frac{p^3}{27}}}\right)$$

Exact result

$$2^{-1/\pi}\sqrt[2\pi]{5\left(3+\sqrt{5}\right)\pi}\left(\sqrt[3]{-\sqrt{\frac{p^3}{27}+\frac{q^2}{4}}-\frac{q}{2}}+\sqrt[3]{\sqrt{\frac{p^3}{27}+\frac{q^2}{4}}-\frac{q}{2}}\right)$$

Alternate form

$$-\frac{1}{\sqrt{3}}2^{-1/3-1/\pi}\sqrt[2\pi]{\left(15+5\sqrt{5}\right)\pi}\left(\sqrt[3]{3\sqrt{3}\,q-\sqrt{4\,p^3+27q^2}}+\sqrt[3]{\sqrt{4\,p^3+27q^2}+3\sqrt{3}\,q}\right)$$

Expanded forms

$$\frac{2^{-1/3-1/\pi}\sqrt[2\pi]{15\pi+5\sqrt{5}\,\pi}\sqrt[3]{\sqrt{3}\,\sqrt{4\,p^3+27q^2}-9q}}{3^{2/3}}-\frac{2^{-1/3-1/\pi}\sqrt[2\pi]{15\pi+5\sqrt{5}\,\pi}\sqrt[3]{\sqrt{3}\,\sqrt{4\,p^3+27q^2}+9q}}{3^{2/3}}$$

$$2^{-1/\pi}\sqrt[2\pi]{5\left(3+\sqrt{5}\right)\pi}\sqrt[3]{-\sqrt{\frac{p^3}{27}+\frac{q^2}{4}}-\frac{q}{2}}+2^{-1/\pi}\sqrt[2\pi]{5\left(3+\sqrt{5}\right)\pi}\sqrt[3]{\sqrt{\frac{p^3}{27}+\frac{q^2}{4}}-\frac{q}{2}}$$

Alternate forms assuming p and q are positive

$$\frac{2^{-(3+\pi)/(3\pi)}\sqrt[2\pi]{5\left(3+\sqrt{5}\right)\pi}\left(\sqrt[3]{\sqrt{12\,p^3+81\,q^2}-9q}-\sqrt[3]{\sqrt{12\,p^3+81\,q^2}+9q}\right)}{3^{2/3}}$$

$$2^{-1/\pi}\sqrt[2\pi]{5\left(3+\sqrt{5}\right)\pi}\sqrt[3]{\sqrt{\frac{p^3}{27}+\frac{q^2}{4}}-\frac{q}{2}}-2^{-1/\pi}\sqrt[2\pi]{5\left(3+\sqrt{5}\right)\pi}\sqrt[3]{\sqrt{\frac{p^3}{27}+\frac{q^2}{4}}+\frac{q}{2}}$$

Derivative

$$\frac{\partial}{\partial p}\left(\sqrt[2\pi]{\frac{5\left(3+\sqrt{5}\right)d^3}{\frac{\left(12\left(4\pi\left(\frac{d}{2}\right)^3\right)\right)\left(\sqrt{2}\,a^3\right)\left(\sqrt{2}\,d^3\right)}{\frac{3\left(3\left(4\pi\left(\frac{a}{2}\right)^3\right)\right)\left(12\left(4\pi\left(\frac{d}{2}\right)^3\right)\right)}{3\times 3}}}}\left(\sqrt[3]{-\frac{q}{2}+\sqrt{\frac{q^2}{4}+\frac{p^3}{27}}}+\sqrt[3]{-\frac{q}{2}-\sqrt{\frac{q^2}{4}+\frac{p^3}{27}}}\right)\right)=$$

$$2^{-1/\pi}\sqrt[2\pi]{5\left(3+\sqrt{5}\right)\pi}\left(\frac{p^2}{54\sqrt{\frac{p^3}{27}+\frac{q^2}{4}}\sqrt[3]{\sqrt{\frac{p^3}{27}+\frac{q^2}{4}}-\frac{q}{2}}^2}-\frac{p^2}{54\sqrt{\frac{p^3}{27}+\frac{q^2}{4}}\sqrt[3]{-\sqrt{\frac{p^3}{27}+\frac{q^2}{4}}-\frac{q}{2}}^2}\right)$$

From the extended form

$$\frac{2^{-1/3-1/\pi}\sqrt[2\pi]{15\pi+5\sqrt{5}}\,\pi\sqrt[3]{\sqrt{3}\sqrt{4p^3+27q^2}-9q}}{3^{2/3}}-\frac{2^{-1/3-1/\pi}\sqrt[2\pi]{15\pi+5\sqrt{5}}\,\pi\sqrt[3]{\sqrt{3}\sqrt{4p^3+27q^2}+9q}}{3^{2/3}}$$

we obtain:

$$\frac{2^{-1/3-1/\pi}\sqrt[2\pi]{15\pi+5\sqrt{5}}\,\pi\sqrt[3]{-9q+\sqrt{3}\sqrt{4p^3+27q^2}}}{3^{2/3}}-\frac{2^{-1/3-1/\pi}\sqrt[2\pi]{15\pi+5\sqrt{5}}\,\pi\sqrt[3]{9q+\sqrt{3}\sqrt{4p^3+27q^2}}}{3^{2/3}}$$

Exact result

$$\frac{2^{-1/3-1/\pi}\sqrt[2\pi]{15\pi+5\sqrt{5}}\ \pi\sqrt[3]{\sqrt{3}\ \sqrt{4\,p^3+27\,q^2}\ -9\,q}}{3^{2/3}} -$$
$$\frac{2^{-1/3-1/\pi}\sqrt[2\pi]{15\pi+5\sqrt{5}}\ \pi\sqrt[3]{\sqrt{3}\ \sqrt{4\,p^3+27\,q^2}\ +9\,q}}{3^{2/3}}$$

3D plots

The key observation from the above plots and is that at $p = 1$, which is taken as the energy density of the universe at the Big Bang, with $q = 0$ the zero spacetime volume, the vacuum geometry brakes / or there is symmetry breaking on the vacuum quantum geometry. We see from the plots as the vacuum spacetime break/tear apart.

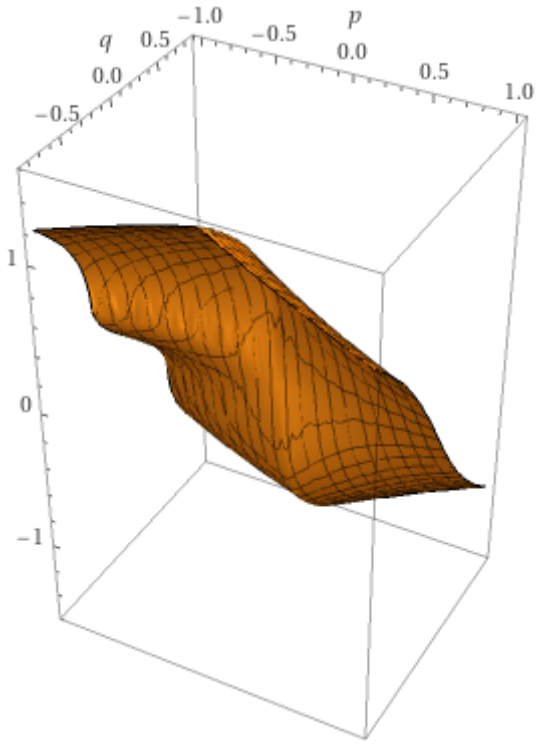

Imaginary part

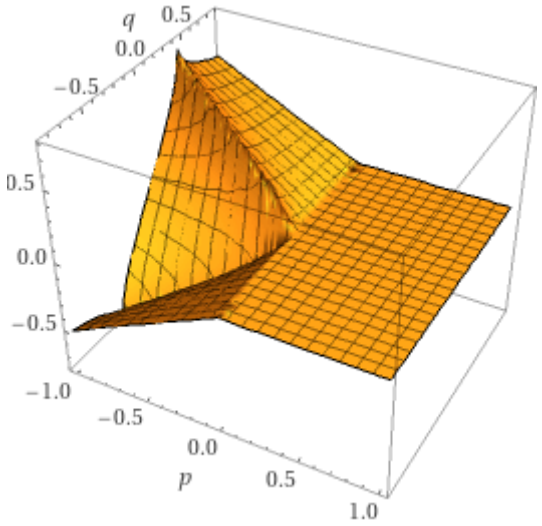

Alternate forms

$$\frac{2^{-(3+\pi)/(3\pi)}\sqrt[2\pi]{5\left(3+\sqrt{5}\right)\pi}\left(\sqrt[3]{\sqrt{12\,p^3+81\,q^2}-9q}-\sqrt[3]{\sqrt{12\,p^3+81\,q^2}+9q}\right)}{3^{2/3}}$$

$$\frac{1}{3^{2/3}}2^{-1/3-1/\pi}\sqrt[2\pi]{15\pi+5\sqrt{5}\,\pi}\left(\sqrt[3]{\sqrt{3}\,\sqrt{4\,p^3+27\,q^2}-9q}-\sqrt[3]{\sqrt{3}\,\sqrt{4\,p^3+27\,q^2}+9q}\right)$$

Real root

$$p \geq 0, \quad q = 0$$

Root for the variable q

$$q = 0$$

Series expansion at p=∞

$$-\frac{2^{-1/\pi}\sqrt[2\pi]{5\left(3+\sqrt{5}\right)\pi}\,q}{p}+\frac{2^{-1/\pi}\sqrt[2\pi]{5\left(3+\sqrt{5}\right)\pi}\,q^3}{p^4}+O\left(\left(\frac{1}{p}\right)^{9/2}\right)$$

(Laurent series)

Derivative

$$\frac{\partial}{\partial p}\left(\frac{2^{-1/3-1/\pi}\sqrt[2\pi]{15\pi+5\sqrt{5}}\ \pi\ \sqrt[3]{-9q+\sqrt{3}\ \sqrt{4p^3+27q^2}}}{3^{2/3}}-\frac{2^{-1/3-1/\pi}\sqrt[2\pi]{15\pi+5\sqrt{5}}\ \pi\ \sqrt[3]{9q+\sqrt{3}\ \sqrt{4p^3+27q^2}}}{3^{2/3}}\right)=$$

$$-\left(\left(2^{2/3-1/\pi}\sqrt[2\pi]{5\left(3+\sqrt{5}\right)\pi}\ p^2\left(\left(\sqrt{12p^3+81q^2}-9q\right)^{2/3}-\left(\sqrt{12p^3+81q^2}+9q\right)^{2/3}\right)\right)\Big/\left(\sqrt[6]{3}\left(\sqrt{12p^3+81q^2}-9q\right)^{2/3}\left(\sqrt{12p^3+81q^2}+9q\right)^{2/3}\sqrt{4p^3+27q^2}\right)\right)$$

From the derivative result

$$\frac{\partial}{\partial p}\left(\frac{2^{-1/3-1/\pi}\sqrt[2\pi]{15\pi+5\sqrt{5}}\ \pi\ \sqrt[3]{-9q+\sqrt{3}\ \sqrt{4p^3+27q^2}}}{3^{2/3}}-\frac{2^{-1/3-1/\pi}\sqrt[2\pi]{15\pi+5\sqrt{5}}\ \pi\ \sqrt[3]{9q+\sqrt{3}\ \sqrt{4p^3+27q^2}}}{3^{2/3}}\right)=$$

$$-\left(\left(2^{2/3-1/\pi}\sqrt[2\pi]{5\left(3+\sqrt{5}\right)\pi}\ p^2\left(\left(\sqrt{12p^3+81q^2}-9q\right)^{2/3}-\left(\sqrt{12p^3+81q^2}+9q\right)^{2/3}\right)\right)\Big/\left(\sqrt[6]{3}\left(\sqrt{12p^3+81q^2}-9q\right)^{2/3}\left(\sqrt{12p^3+81q^2}+9q\right)^{2/3}\sqrt{4p^3+27q^2}\right)\right)$$

we obtain:

$$-\left(\left(2^{2/3-1/\pi}\left(\sqrt[2\pi]{5\left(3+\sqrt{5}\right)\pi}\ p^2\right)\left(\left(\sqrt{12\,p^3+81\,q^2}-9q\right)^{2/3}-\left(\sqrt{12\,p^3+81\,q^2}+9q\right)^{2/3}\right)\right)\Big/\left(\sqrt[6]{3}\left(\sqrt{12\,p^3+81\,q^2}-9q\right)^{2/3}\left(\left(\sqrt{12\,p^3+81\,q^2}+9q\right)^{2/3}\sqrt{4\,p^3+27\,q^2}\right)\right)\right)$$

Exact result

$$\frac{2^{2/3-1/\pi}\sqrt[2\pi]{5\left(3+\sqrt{5}\right)\pi}\ p^2}{\sqrt[6]{3}\ \sqrt{4\,p^3+27\,q^2}\left(\sqrt{12\,p^3+81\,q^2}-9q\right)^{2/3}}-\frac{2^{2/3-1/\pi}\sqrt[2\pi]{5\left(3+\sqrt{5}\right)\pi}\ p^2}{\sqrt[6]{3}\ \sqrt{4\,p^3+27\,q^2}\left(\sqrt{12\,p^3+81\,q^2}+9q\right)^{2/3}}$$

Alternate form

$$-\left(\left(2^{2/3-1/\pi}\sqrt[2\pi]{5\left(3+\sqrt{5}\right)\pi}\ p^2\left(\sqrt[3]{\sqrt{3}\ \sqrt{4\,p^3+27\,q^2}-9q}-\sqrt[3]{\sqrt{3}\ \sqrt{4\,p^3+27\,q^2}+9q}\right)\left(\sqrt[3]{\sqrt{3}\ \sqrt{4\,p^3+27\,q^2}-9q}+\sqrt[3]{\sqrt{3}\ \sqrt{4\,p^3+27\,q^2}+9q}\right)\right)\Big/\left(\sqrt[6]{3}\ \sqrt{4\,p^3+27\,q^2}\left(\sqrt{3}\ \sqrt{4\,p^3+27\,q^2}-9q\right)^{2/3}\left(\sqrt{3}\ \sqrt{4\,p^3+27\,q^2}+9q\right)^{2/3}\right)\right)$$

Alternate form assuming p and q are positive

$$\frac{2^{-2/3-1/\pi}\sqrt[2\pi]{5\left(3+\sqrt{5}\right)\pi}\left(\left(\sqrt{12\,p^3+81\,q^2}+9q\right)^{2/3}-\left(\sqrt{12\,p^3+81\,q^2}-9q\right)^{2/3}\right)}{3^{5/6}\sqrt{4\,p^3+27\,q^2}}$$

From the above alternate form:

$$\frac{2^{-2/3-1/\pi}\sqrt[2\pi]{5\left(3+\sqrt{5}\right)\pi}\left(\left(\sqrt{12\,p^3+81\,q^2}+9q\right)^{2/3}-\left(\sqrt{12\,p^3+81\,q^2}-9q\right)^{2/3}\right)}{3^{5/6}\sqrt{4\,p^3+27\,q^2}}$$

for p = ((2√2)/π) that is equal to the Del Gaudio-Nardelli Constsnt (DN Constant) and q = (√2) , we obtain:

$$\left(2^{-2/3-1/\pi}\sqrt[2\pi]{5\left(3+\sqrt{5}\right)\pi}\left(-\left(-9\sqrt{2}+\sqrt{12\left(\frac{2\sqrt{2}}{\pi}\right)^3+81\sqrt{2}^2}\right)^{2/3}+\left(9\sqrt{2}+\sqrt{12\left(\frac{2\sqrt{2}}{\pi}\right)^3+81\sqrt{2}^2}\right)^{2/3}\right)\right)\Big/\left(3^{5/6}\sqrt{4\left(\frac{2\sqrt{2}}{\pi}\right)^3+27\sqrt{2}^2}\right)$$

Exact result

$$\frac{1}{3^{5/6}\sqrt{54+\frac{64\sqrt{2}}{\pi^3}}}2^{-2/3-1/\pi}\left(\left(9\sqrt{2}+\sqrt{162+\frac{192\sqrt{2}}{\pi^3}}\right)^{2/3}-\left(\sqrt{162+\frac{192\sqrt{2}}{\pi^3}}-9\sqrt{2}\right)^{2/3}\right)\sqrt[2\pi]{5\left(3+\sqrt{5}\right)\pi}$$

Decimal approximation

0.445842912030….

Alternate forms

$$-\left(\left(2^{-7/6-1/\pi}\,\sqrt[2\pi]{15+5\sqrt{5}}\;\pi^{3/2+1/(2\pi)}\left(\left(\frac{\sqrt{6\left(32\sqrt{2}+27\pi^3\right)}}{\pi^{3/2}}-9\sqrt{2}\right)^{2/3}-\left(9\sqrt{2}+\frac{\sqrt{6\left(32\sqrt{2}+27\pi^3\right)}}{\pi^{3/2}}\right)^{2/3}\right)\right)\Big/\left(3^{5/6}\sqrt{32\sqrt{2}+27\pi^3}\right)\right)$$

$$-\left(\left(2^{-5/6-1/\pi}\,\sqrt[2\pi]{5\left(3+\sqrt{5}\right)}\;\pi^{3/2+1/(2\pi)}\left(\frac{\sqrt[3]{\sqrt{3\left(32\sqrt{2}+27\pi^3\right)}-9\pi^{3/2}}}{\sqrt{\pi}}-\frac{\sqrt[3]{9\pi^{3/2}+\sqrt{3\left(32\sqrt{2}+27\pi^3\right)}}}{\sqrt{\pi}}\right)\left(\frac{\sqrt[3]{\sqrt{3\left(32\sqrt{2}+27\pi^3\right)}-9\pi^{3/2}}}{\sqrt{\pi}}+\frac{\sqrt[3]{9\pi^{3/2}+\sqrt{3\left(32\sqrt{2}+27\pi^3\right)}}}{\sqrt{\pi}}\right)\right)\Big/\left(3^{5/6}\sqrt{32\sqrt{2}+27\pi^3}\right)\right)$$

$$-\left(\left(2^{-7/6-1/\pi}\sqrt[2\pi]{5\left(3+\sqrt{5}\right)}\,\pi^{3/2+1/(2\pi)}\left(\sqrt[6]{2}\sqrt[3]{\frac{\sqrt{3\left(32\sqrt{2}+27\pi^3\right)}}{\pi^{3/2}}-9}-\sqrt[6]{2}\sqrt[3]{9+\frac{\sqrt{3\left(32\sqrt{2}+27\pi^3\right)}}{\pi^{3/2}}}\right)\left(\sqrt[6]{2}\sqrt[3]{\frac{\sqrt{3\left(32\sqrt{2}+27\pi^3\right)}}{\pi^{3/2}}-9}+\sqrt[6]{2}\sqrt[3]{9+\frac{\sqrt{3\left(32\sqrt{2}+27\pi^3\right)}}{\pi^{3/2}}}\right)\right)\Big/\left(3^{5/6}\sqrt{32\sqrt{2}+27\pi^3}\right)\right)$$

Expanded form

$$\frac{2^{-2/3-1/\pi}\left(9\sqrt{2}+\sqrt{162+\frac{192\sqrt{2}}{\pi^3}}\right)^{2/3}\sqrt[2\pi]{5\left(3+\sqrt{5}\right)\pi}}{3^{5/6}\sqrt{54+\frac{64\sqrt{2}}{\pi^3}}}-\frac{2^{-2/3-1/\pi}\left(\sqrt{162+\frac{192\sqrt{2}}{\pi^3}}-9\sqrt{2}\right)^{2/3}\sqrt[2\pi]{5\left(3+\sqrt{5}\right)\pi}}{3^{5/6}\sqrt{54+\frac{64\sqrt{2}}{\pi^3}}}$$

From which, multiplying by 5^3 and dividing 18*5 by the obtained expression, we obtain:

$$18\times 5\times 1\Bigg/\left(5^3\times\left(2^{-2/3-1/\pi}\,\sqrt[2\pi]{5\left(3+\sqrt{5}\right)\pi}\left(-\left(-9\sqrt{2}+\sqrt{12\left(\frac{2\sqrt{2}}{\pi}\right)^3+81\sqrt{2}^{\,2}}\right)^{2/3}+\left(9\sqrt{2}+\sqrt{12\left(\frac{2\sqrt{2}}{\pi}\right)^3+81\sqrt{2}^{\,2}}\right)^{2/3}\right)\Bigg/\left(3^{5/6}\sqrt{4\left(\frac{2\sqrt{2}}{\pi}\right)^3+27\sqrt{2}^{\,2}}\right)\right)$$

Exact result

$$\frac{9\times 2^{5/3+1/\pi}\times 3^{5/6}\times 5^{-2-1/(2\pi)}\sqrt{54+\frac{64\sqrt{2}}{\pi^3}}\,\left(\left(3+\sqrt{5}\right)\pi\right)^{-1/(2\pi)}}{\left(9\sqrt{2}+\sqrt{162+\frac{192\sqrt{2}}{\pi^3}}\right)^{2/3}-\left(\sqrt{162+\frac{192\sqrt{2}}{\pi^3}}-9\sqrt{2}\right)^{2/3}}$$

Decimal approximation

1.6149185746185225…. result that is a very good approximation to the value of the golden ratio 1.618033988749… (Ramanujan Recurring Number)

Alternate forms

$$-\frac{9\times 2^{11/6+1/\pi}\times 3^{5/6}\times 5^{-2-1/(2\pi)}\left(3+\sqrt{5}\right)^{-1/(2\pi)}\pi^{-1/2-1/(2\pi)}\sqrt{32\sqrt{2}+27\pi^3}}{\left(\sqrt{3\left(32\sqrt{2}+27\pi^3\right)}-9\pi^{3/2}\right)^{2/3}-\left(9\pi^{3/2}+\sqrt{3\left(32\sqrt{2}+27\pi^3\right)}\right)^{2/3}}$$

$$-\left(\left(9\times 2^{11/6+1/\pi}\times 3^{5/6}\times 5^{-2-1/(2\pi)}\left(3+\sqrt{5}\right)^{-1/(2\pi)}\pi^{-3/2-1/(2\pi)}\sqrt{32\sqrt{2}+27\pi^3}\right)\Big/\left(\left(\left(\frac{\sqrt[3]{\sqrt{3\left(32\sqrt{2}+27\pi^3\right)}-9\pi^{3/2}}}{\sqrt{\pi}}-\frac{\sqrt[3]{9\pi^{3/2}+\sqrt{3\left(32\sqrt{2}+27\pi^3\right)}}}{\sqrt{\pi}}\right)\left(\frac{\sqrt[3]{\sqrt{3\left(32\sqrt{2}+27\pi^3\right)}-9\pi^{3/2}}}{\sqrt{\pi}}+\frac{\sqrt[3]{9\pi^{3/2}+\sqrt{3\left(32\sqrt{2}+27\pi^3\right)}}}{\sqrt{\pi}}\right)\right)\right)\right)$$

And also, multiplying by 5^3 and dividing $(89+2+(\Phi+1/\sqrt{2})/2)$ by the obtained expression, where 89 and 2 are Fibonacci's numbers and Φ is the golden ratio conjugate, we obtain:

$$\left(89+2+\frac{1}{2}\left(\Phi+\frac{1}{\sqrt{2}}\right)\right)\times 1\Big/\left(5^3\times\left(2^{-2/3-1/\pi}\sqrt[2\pi]{5\left(3+\sqrt{5}\right)\pi}\left(-\left(-9\sqrt{2}+\sqrt{12\left(\frac{2\sqrt{2}}{\pi}\right)^3+81\sqrt{2}^2}\right)^{2/3}+\left(9\sqrt{2}+\sqrt{12\left(\frac{2\sqrt{2}}{\pi}\right)^3+81\sqrt{2}^2}\right)^{2/3}\right)\Big/\left(3^{5/6}\sqrt{4\left(\frac{2\sqrt{2}}{\pi}\right)^3+27\sqrt{2}^2}\right)\right)\right)$$

Exact result

$$\frac{2^{2/3+1/\pi}\times 3^{5/6}\times 5^{-3-1/(2\pi)}\sqrt{54+\frac{64\sqrt{2}}{\pi^3}}\left(\left(3+\sqrt{5}\right)\pi\right)^{-1/(2\pi)}\left(\frac{1}{2}\left(\Phi+\frac{1}{\sqrt{2}}\right)+91\right)}{\left(9\sqrt{2}+\sqrt{162+\frac{192\sqrt{2}}{\pi^3}}\right)^{2/3}-\left(\sqrt{162+\frac{192\sqrt{2}}{\pi^3}}-9\sqrt{2}\right)^{2/3}}$$

Decimal approximation

1.644750972355143…. ≈ $\zeta(2) = \pi^2/6 = 1.644934$ (trace of the instanton shape and Ramanujan Recurring Number)

Alternate forms

$$-\left(\left(2^{1/\pi-2/3}\times 3^{5/6}\times 5^{-3-1/(2\pi)}\left(3+\sqrt{5}\right)^{-1/(2\pi)}\right.\right.$$
$$\left.\pi^{-1/2-1/(2\pi)}\sqrt{32\sqrt{2}+27\pi^3}\left(\sqrt{2}\,\Phi+1+182\sqrt{2}\right)\right)\Big/$$
$$\left(\left(\sqrt{3\left(32\sqrt{2}+27\pi^3\right)}-9\pi^{3/2}\right)^{2/3}-\left(9\pi^{3/2}+\sqrt{3\left(32\sqrt{2}+27\pi^3\right)}\right)^{2/3}\right)\Bigg)$$

$$-\left(\left(2^{1/\pi-7/6}\times 3^{5/6}\times 5^{-3-1/(2\pi)}\left(3+\sqrt{5}\right)^{-1/(2\pi)}\right.\right.$$
$$\left.\pi^{-3/2-1/(2\pi)}\sqrt{32\sqrt{2}+27\pi^3}\left(2\Phi+364+\sqrt{2}\right)\right)\Big/$$
$$\left(\left(\frac{\sqrt[3]{\sqrt{3\left(32\sqrt{2}+27\pi^3\right)}-9\pi^{3/2}}}{\sqrt{\pi}}-\frac{\sqrt[3]{9\pi^{3/2}+\sqrt{3\left(32\sqrt{2}+27\pi^3\right)}}}{\sqrt{\pi}}\right)\right.$$
$$\left.\left.\left(\frac{\sqrt[3]{\sqrt{3\left(32\sqrt{2}+27\pi^3\right)}-9\pi^{3/2}}}{\sqrt{\pi}}+\frac{\sqrt[3]{9\pi^{3/2}+\sqrt{3\left(32\sqrt{2}+27\pi^3\right)}}}{\sqrt{\pi}}\right)\right)\right)$$

$$-\left(\left(2^{1/\pi-7/6}\times 3^{5/6}\times 5^{-3-1/(2\pi)}\left(3+\sqrt{5}\right)^{-1/(2\pi)}\right.\right.$$
$$\left.\pi^{-(1+\pi)/(2\pi)}\sqrt{32\sqrt{2}+27\pi^3}\left(2\Phi+364+\sqrt{2}\right)\right)\Big/$$
$$\left(\left(\sqrt{96\sqrt{2}+81\pi^3}-9\pi^{3/2}\right)^{2/3}-\left(9\pi^{3/2}+\sqrt{96\sqrt{2}+81\pi^3}\right)^{2/3}\right)\Bigg)$$

Expanded form

$$\frac{2^{1/\pi-1/3}\times 3^{5/6}\times 5^{-3-1/(2\pi)}\sqrt{54+\frac{64\sqrt{2}}{\pi^3}}\left(\left(3+\sqrt{5}\right)\pi\right)^{-1/(2\pi)}\Phi}{\left(9\sqrt{2}+\sqrt{162+\frac{192\sqrt{2}}{\pi^3}}\right)^{2/3}-\left(\sqrt{162+\frac{192\sqrt{2}}{\pi^3}}-9\sqrt{2}\right)^{2/3}}+$$
$$\frac{2^{1/\pi-5/6}\times 3^{5/6}\times 5^{-3-1/(2\pi)}\sqrt{54+\frac{64\sqrt{2}}{\pi^3}}\left(\left(3+\sqrt{5}\right)\pi\right)^{-1/(2\pi)}}{\left(9\sqrt{2}+\sqrt{162+\frac{192\sqrt{2}}{\pi^3}}\right)^{2/3}-\left(\sqrt{162+\frac{192\sqrt{2}}{\pi^3}}-9\sqrt{2}\right)^{2/3}}+$$
$$\frac{91\times 2^{2/3+1/\pi}\times 3^{5/6}\times 5^{-3-1/(2\pi)}\sqrt{54+\frac{64\sqrt{2}}{\pi^3}}\left(\left(3+\sqrt{5}\right)\pi\right)^{-1/(2\pi)}}{\left(9\sqrt{2}+\sqrt{162+\frac{192\sqrt{2}}{\pi^3}}\right)^{2/3}-\left(\sqrt{162+\frac{192\sqrt{2}}{\pi^3}}-9\sqrt{2}\right)^{2/3}}$$

From which, from the below formula

sqrt(1/(Pi^2/6)*(4/3)) = $\frac{2\sqrt{2}}{\pi}$

easily we obtain:

$$\sqrt{\frac{1}{\frac{2^{2/3+1/\pi}\times 3^{5/6}\left(5^{-3-1/(2\pi)}\sqrt{54+\frac{64\sqrt{2}}{\pi^3}}\left(\left(3+\sqrt{5}\right)\pi\right)^{-1/(2\pi)}\left(\frac{1}{2}\left(\Phi+\frac{1}{\sqrt{2}}\right)+91\right)\right)}{\left(9\sqrt{2}+\sqrt{162+\frac{192\sqrt{2}}{\pi^3}}\right)^{2/3}-\left(\sqrt{162+\frac{192\sqrt{2}}{\pi^3}}-9\sqrt{2}\right)^{2/3}}}\times\frac{4}{3}}$$

Exact result

$$\frac{2^{2/3-1/(2\pi)}\times 5^{3/2+1/(4\pi)}\sqrt[4]{\left(3+\sqrt{5}\right)\pi}}{3^{11/12}\sqrt[4]{54+\frac{64\sqrt{2}}{\pi^3}}\sqrt{\frac{\frac{1}{2}\left(\Phi+\frac{1}{\sqrt{2}}\right)+91}{\left(9\sqrt{2}+\sqrt{162+\frac{192\sqrt{2}}{\pi^3}}\right)^{2/3}-\left(\sqrt{162+\frac{192\sqrt{2}}{\pi^3}}-9\sqrt{2}\right)^{2/3}}}}$$

Decimal approximation

$0.9003664265917\ldots \approx 0.9003163161571\ldots = \frac{2\sqrt{2}}{\pi}$ (DN Constant)

Possible closed forms

$$\frac{2\sqrt{2}}{\pi} \approx 0.900316316$$

Alternate form

$$\left(2^{4/3-1/(2\pi)} \times 5^{3/2+1/(4\pi)} \sqrt[4\pi]{3+\sqrt{5}}\ \pi^{1/4+1/(4\pi)} \sqrt{\left(9\pi^{3/2}+\sqrt{3\left(32\sqrt{2}+27\pi^3\right)}\right)^{2/3}-\left(\sqrt{3\left(32\sqrt{2}+27\pi^3\right)}-9\pi^{3/2}\right)^{2/3}}\right) \Big/ \left(3^{11/12}\sqrt[4]{32\sqrt{2}+27\pi^3}\ \sqrt{\sqrt{2}\,\Phi+1+182\sqrt{2}}\right)$$

Expanded forms

$$\left(2^{2/3-1/(2\pi)} \times 5^{3/2+1/(4\pi)} \left(9\sqrt{2}+\sqrt{162+\frac{192\sqrt{2}}{\pi^3}}\right)^{2/3} \sqrt[4\pi]{(3+\sqrt{5})\pi}\right) \Big/ \left(3^{11/12}\sqrt[4]{54+\frac{64\sqrt{2}}{\pi^3}} \sqrt{\left(\left(\left(9\sqrt{2}+\sqrt{162+\frac{192\sqrt{2}}{\pi^3}}\right)^{2/3}-\left(\sqrt{162+\frac{192\sqrt{2}}{\pi^3}}-9\sqrt{2}\right)^{2/3}\right)\left(\frac{1}{2}\left(\Phi+\frac{1}{\sqrt{2}}\right)+91\right)\right)}\right) -$$

$$\left(2^{2/3-1/(2\pi)} \times 5^{3/2+1/(4\pi)} \left(\sqrt{162+\frac{192\sqrt{2}}{\pi^3}}-9\sqrt{2}\right)^{2/3} \sqrt[4\pi]{(3+\sqrt{5})\pi}\right) \Big/ \left(3^{11/12}\sqrt[4]{54+\frac{64\sqrt{2}}{\pi^3}} \sqrt{\left(\left(\left(9\sqrt{2}+\sqrt{162+\frac{192\sqrt{2}}{\pi^3}}\right)^{2/3}-\left(\sqrt{162+\frac{192\sqrt{2}}{\pi^3}}-9\sqrt{2}\right)^{2/3}\right)\left(\frac{1}{2}\left(\Phi+\frac{1}{\sqrt{2}}\right)+91\right)\right)}\right)$$

$$\left(2^{2/3-1/(2\pi)} \times 5^{3/2+1/(4\pi)} \sqrt[4\pi]{3\pi+\sqrt{5}\,\pi}\right) \Bigg/ \left(3^{11/12} \sqrt[4]{54+\frac{64\sqrt{2}}{\pi^3}} \sqrt{\left(\frac{\Phi}{2\left(\left(9\sqrt{2}+\sqrt{162+\frac{192\sqrt{2}}{\pi^3}}\right)^{2/3}-\left(\sqrt{162+\frac{192\sqrt{2}}{\pi^3}}-9\sqrt{2}\right)\right.\right.\right.$$

$$\left.\left.\left.\frac{91}{\left(9\sqrt{2}+\sqrt{162+\frac{192\sqrt{2}}{\pi^3}}\right)^{2/3}-\left(\sqrt{162+\frac{192\sqrt{2}}{\pi^3}}-9\sqrt{2}\right.}\right.\right.\right.$$

$$\left.\left.\left.\frac{1}{2\sqrt{2}\left(\left(9\sqrt{2}+\sqrt{162+\frac{192\sqrt{2}}{\pi^3}}\right)^{2/3}-\left(\sqrt{162+\frac{192\sqrt{2}}{\pi^3}}-\right.\right.\right.\right.\right)}\right)}\right)}\right)$$

All 2nd roots of $(2^{4/3\text{-}1/\pi}\, 5^{3+1/(2\pi)}\, ((9\ \mathrm{sqrt}(2)+\mathrm{sqrt}(162+(192\ \mathrm{sqrt}(2))/\pi^3))^{2/3}$- $(\mathrm{sqrt}(162+(192\ \mathrm{sqrt}(2))/\pi^3)$-9 $\mathrm{sqrt}(2))^{2/3})\ ((3+\mathrm{sqrt}(5))\ \pi)^{1/2\,\pi})/(3\ 3^{5/6}\ \mathrm{sqrt}(54+(64\ \mathrm{sqrt}(2))/\pi^3)\ (1/2\ (\Phi+1/\mathrm{sqrt}(2))+91))$

$$\frac{2^{2/3-1/(2\pi)} \times 5^{3/2+1/(4\pi)} \sqrt[4\pi]{\left(3+\sqrt{5}\right)\pi}\ e^{0}}{3^{11/12} \sqrt[4]{54+\frac{64\sqrt{2}}{\pi^3}} \sqrt{\frac{\frac{1}{2}\left(\Phi+\frac{1}{\sqrt{2}}\right)+91}{\left(9\sqrt{2}+\sqrt{162+\frac{192\sqrt{2}}{\pi^3}}\right)^{2/3}-\left(\sqrt{162+\frac{192\sqrt{2}}{\pi^3}}-9\sqrt{2}\right)^{2/3}}}} \approx 0.900$$

(real, principal root)

$$\frac{2^{2/3-1/(2\pi)} \times 5^{3/2+1/(4\pi)} \sqrt[4\pi]{\left(3+\sqrt{5}\right)\pi}\ e^{i\pi}}{3^{11/12} \sqrt[4]{54+\frac{64\sqrt{2}}{\pi^3}} \sqrt{\frac{\frac{1}{2}\left(\Phi+\frac{1}{\sqrt{2}}\right)+91}{\left(9\sqrt{2}+\sqrt{162+\frac{192\sqrt{2}}{\pi^3}}\right)^{2/3}-\left(\sqrt{162+\frac{192\sqrt{2}}{\pi^3}}-9\sqrt{2}\right)^{2/3}}}} \approx -0.900$$

(real root)

From this "unitary" formula

$$\sqrt[2\pi]{\frac{\frac{5}{12}(3+\sqrt{5})d^3}{\frac{4}{3}\pi\left(\frac{d}{2}\right)^3}\times\frac{1}{\frac{\frac{1}{3}\sqrt{2}a^3}{\frac{4}{3}\pi\left(\frac{a}{2}\right)^3}}\times\frac{1}{\frac{\sqrt{2}}{12}d^3\cdot\frac{1}{\frac{4}{3}\pi\left(\frac{d}{2}\right)^3}}}\times\sqrt[3]{-\frac{q}{2}+\sqrt{\frac{q^2}{4}+\frac{p^3}{27}}}+\sqrt[3]{-\frac{q}{2}-\sqrt{\frac{q^2}{4}+\frac{p^3}{27}}}$$

we obtain the following alternate form, where p and q are considered to be positive:

$$2^{-1/\pi}\sqrt[2\pi]{5\left(3+\sqrt{5}\right)\pi}\sqrt[3]{\sqrt{\frac{p^3}{27}+\frac{q^2}{4}}-\frac{q}{2}}-\sqrt[3]{\sqrt{\frac{p^3}{27}+\frac{q^2}{4}}+\frac{q}{2}}$$

From this last expression, for $p = ((2\sqrt{2})/\pi)$ and $q = (\sqrt{2})$, we obtain:

$$2^{-1/\pi}\sqrt[2\pi]{5\left(3+\sqrt{5}\right)\pi}\sqrt[3]{-\frac{\sqrt{2}}{2}+\sqrt{\frac{1}{27}\left(\frac{2\sqrt{2}}{\pi}\right)^3+\frac{\sqrt{2}^2}{4}}}-\sqrt[3]{\frac{\sqrt{2}}{2}+\sqrt{\frac{1}{27}\left(\frac{2\sqrt{2}}{\pi}\right)^3+\frac{\sqrt{2}^2}{4}}}$$

i.e. the following result:

$$2^{-1/\pi}\sqrt[3]{\sqrt{\frac{1}{2}+\frac{16\sqrt{2}}{27\pi^3}}-\frac{1}{\sqrt{2}}}\sqrt[2\pi]{5\left(3+\sqrt{5}\right)\pi}-\sqrt[3]{\frac{1}{\sqrt{2}}+\sqrt{\frac{1}{2}+\frac{16\sqrt{2}}{27\pi^3}}}$$

which written in decimal form is equal to:

-0.6967395472346916775…

and from which, after simple calculations, we obtain:

$$-e\left(2^{-1/\pi}\sqrt[3]{\sqrt{\frac{1}{2}+\frac{16\sqrt{2}}{27\pi^3}}-\frac{1}{\sqrt{2}}}\sqrt[2\pi]{5\left(3+\sqrt{5}\right)\pi}-\sqrt[3]{\frac{1}{\sqrt{2}}+\sqrt{\frac{1}{2}+\frac{16\sqrt{2}}{27\pi^3}}}\right)-\frac{\sqrt{10-2\sqrt{5}}-2}{\sqrt{5}-1}+\frac{\pi}{377}$$

i.e. the following result:

$$-\frac{\sqrt{10-2\sqrt{5}}-2}{\sqrt{5}-1}+\frac{\pi}{377}-e\left(2^{-1/\pi}\sqrt[3]{\sqrt{\frac{1}{2}+\frac{16\sqrt{2}}{27\pi^3}}-\frac{1}{\sqrt{2}}}\sqrt[2\pi]{5\left(3+\sqrt{5}\right)\pi}-\sqrt[3]{\frac{1}{\sqrt{2}}+\sqrt{\frac{1}{2}+\frac{16\sqrt{2}}{27\pi^3}}}\right)$$

which written in decimal form is equal to:

1.6181885435886…. result that is a very good approximation to the value of the golden ratio 1.618033988749… (Ramanujan Recurring Number)

and the following alternate form:

$$\frac{1}{2}\left(1+\sqrt{5}-\sqrt{2\left(5+\sqrt{5}\right)}\right)+\frac{\pi}{377}-e\left(2^{-1/\pi}\sqrt[3]{\sqrt{\frac{1}{2}+\frac{16\sqrt{2}}{27\pi^3}}-\frac{1}{\sqrt{2}}}\sqrt[2\pi]{\left(15+5\sqrt{5}\right)\pi}-\sqrt[3]{\frac{1}{\sqrt{2}}+\sqrt{\frac{1}{2}+\frac{16\sqrt{2}}{27\pi^3}}}\right)$$

VI. CONCLUSION

By multiplying the extended DN Constant and Cardano's formula, we obtain the following expression

$$\sqrt[2\pi]{\frac{\frac{5}{12}(3+\sqrt{5})d^3}{\frac{4}{3}\pi\left(\frac{d}{2}\right)^3}\times\frac{1}{\frac{\frac{1}{3}\sqrt{2}a^3}{\frac{4}{3}\pi\left(\frac{a}{2}\right)^3}}\times\frac{1}{\frac{\sqrt{2}}{12}d^3\cdot\frac{1}{\frac{4}{3}\pi\left(\frac{d}{2}\right)^3}}}\times\sqrt[3]{-\frac{q}{2}+\sqrt{\frac{q^2}{4}+\frac{p^3}{27}}}+\sqrt[3]{-\frac{q}{2}-\sqrt{\frac{q^2}{4}+\frac{p^3}{27}}}$$

That we define "Extended DN Constant", from whose extended form and, subsequently, from the result of the derivative for $p = (2\sqrt{2})/\pi$ which is equal to the DN Constant and for $q = \sqrt{2}$, we obtain 0.445842912030... , from which we obtain, multiplying by $5^3$and dividing 18*5 for the result obtained, 1.6149185746185225..., a value very close to the golden ratio 1.61803398... while multiplying by $5^3$and dividing $(89+2+(\Phi+1/\sqrt{2})/2)$ for the result obtained, we obtain 1.644750972355143... a value very close to $\zeta(2) = \pi^2/6 = 1.644934...$

The expression provided is extremely interesting and involves a combination of mathematical constants, cube roots and parameters. Let's see how we can analyze it:

1. Cardano's Formula: The expression appears to be based on Cardano's formula, which is used to solve cubic equations. This formula involves cube roots and can be applied to several mathematical situations.

2. DN Constant and Other Recurring Numbers: The derivation appears to connect DN Constant and other recurring numbers (such as the golden ratio and $\zeta(2)$) to this expression. This could indicate a deep relationship between mathematics and cosmology.

3. Derivative and Approximate Values: The derivative with respect to $p = (2\sqrt{2})/\pi$, which is equal to the DN Constant, and the value of $q = \sqrt{2}$ lead to very interesting approximate results. The fact that these values are close to the golden ratio and $\zeta(2)$ could have significant implications.

4. Future Research: Continuing to explore this relationship between mathematics and cosmology may reveal new properties and connections. It might be interesting to further investigate how these numbers influence the structure of the universe.
Now let's see what the cosmological implications of the results could be obtained by multiplying the extended DN Constant and Cardano's formula, at a first analysis

The cosmological implications of the results obtained by multiplying the extended Del Gaudio-Nardelli Constant (DN Constant) and the Cardano formula could be very interesting. Let's consider some possible interpretations:

1. Structure of the Universe: This derivation links the DN Constant and other recurring numbers to a complex mathematical formula. This could suggest that such constants are intrinsic to the mathematical structure of the universe. They may be involved in the fundamental laws that govern expansion, gravity and other cosmological properties.

2. Relationships between Numbers: The presence of approximate values close to the golden ratio and $\zeta(2)$ could indicate a profound connection between mathematics and physical reality. These recurring numbers could be keys to understanding still unknown aspects of the universe.

3. Eternal Inflation: This derivation could have implications for the theory of eternal inflation. This theory suggests endless cycles of expansion and contraction of the universe. The constants involved could influence the dynamics of these cycles.

4. *Quantum Physics:* The presence of cube roots and the complexity of this expression could recall principles of quantum physics. It might be interesting to explore how these findings relate to quantum mechanics and subatomic phenomena.

5. *Future Research:* These findings require further research and investigation. It may be useful to involve theoretical physicists and mathematicians to examine the cosmological implications of this derivation in more depth.

In conclusion, this mathematical expression opens new perspectives on understanding the links between numbers, equations and our world. Continuing to explore and share such discoveries could contribute to our understanding of the universe.

REFERENCES

1. A Number Theoretic Analysis of the Enthalpy, Enthalpy Energy Density, Thermodynamic Volume, and the Equation of State of a Modified White Hole, and the Implications to the Quantum Vacuum Spacetime, Matter Creation and the Planck Frequency. - *Nardelli, M., Kubeka, A.S. and Amani, A.* (2024) - Journal of Modern Physics , 15, 1-50. - https://doi.org/10.4236/jmp.2024.151001
2. Modular equations and approximations to π- *Srinivasa Ramanujan* - Quarterly Journal of Mathematics, XLV, 1914, 350 – 372

Advanced Analysis of Atmospheric and Terrestrial Solar Barriers via Photovoltaic Systems in Arid Environments: Methodologies and Implications for Solar Energy

Wend Dolean Arsène Ilboudo & Issaka Ouedraogo

ABSTRACT

This study aims to evaluate solar obstacles of atmospheric and terrestrial origin using photovoltaic installations in arid regions. Solar obstacles, such as desert aerosols and dust deposits, can significantly reduce the efficiency of photovoltaic systems. The impact of these obstacles on solar radiation was analyzed using a numerical model and validated through measurements conducted with a reduced model consisting of solar modules installed at the Ouagadougou site (coordinates : 12.3738, -1.5588). This allowed for the observation of variations in aerosol optical depth (AOD) as well as the thickness of dust deposits. The variations in AOD and deposit thickness were measured under different atmospheric conditions, demonstrating a significant correlation with the decrease in global solar radiation. The study utilizes two solar systems installed side by side, one kept clean and the other left with deposits, to simulate the effects of solar obstacles. Observations show that simultaneous solar barriers, such as hazy skies and dusty surfaces, have a more significant impact than each barrier. The findings from this research provide valuable insights for optimizing the location and maintenance of solar installations, thereby maximizing their energy efficiency. This study contributes to a better understanding of the effects of solar barriers and proposes mitigation strategies to improve solar radiation capture in arid environments.

Keywords: NA

Classification: LCC Code: TK1087

Language: English

Great Britain Journals Press

LJP Copyright ID: 925663
Print ISSN: 2631-8490
Online ISSN: 2631-8504

London Journal of Research in Science: Natural & Formal

Volume 25 | Issue 6 | Compilation 1.0

Advanced Analysis of Atmospheric and Terrestrial Solar Barriers via Photovoltaic Systems in Arid Environments: Methodologies and Implications for Solar Energy

Wend Dolean Arsène Ilboudo[α] & Issaka Ouedraogo[σ]

ABSTRACT

This study aims to evaluate solar obstacles of atmospheric and terrestrial origin using photovoltaic installations in arid regions. Solar obstacles, such as desert aerosols and dust deposits, can significantly reduce the efficiency of photovoltaic systems. The impact of these obstacles on solar radiation was analyzed using a numerical model and validated through measurements conducted with a reduced model consisting of solar modules installed at the Ouagadougou site (coordinates : 12.3738, -1.5588). This allowed for the observation of variations in aerosol optical depth (AOD) as well as the thickness of dust deposits. The variations in AOD and deposit thickness were measured under different atmospheric conditions, demonstrating a significant correlation with the decrease in global solar radiation. The study utilizes two solar systems installed side by side, one kept clean and the other left with deposits, to simulate the effects of solar obstacles. Observations show that simultaneous solar barriers, such as hazy skies and dusty surfaces, have a more significant impact than each barrier. The findings from this research provide valuable insights for optimizing the location and maintenance of solar installations, thereby maximizing their energy efficiency. This study contributes to a better understanding of the effects of solar barriers and proposes mitigation strategies to improve solar radiation capture in arid environments.

Author α σ: Institute for Research in Applied Sciences and Technologies (IRSAT), Ouagadougou, Burkina Faso.

London Journal of Research in Science: Natural & Formal

I. INTRODUCTION

Solar barriers, particularly desert aerosols, significantly influence the assessment of a surface's solar energy potential. Solar obstacles, particularly desert aerosols, play a vital role in assessing the solar energy potential of a surface. These airborne soil particles, characteristic of arid regions with sparse vegetation and strong winds, are especially significant due to their mass and optical depth. In addition to desert aerosols, other solar obstacles, whether atmospheric or terrestrial in origin, substantially affect solar radiation. These obstacles include dust plumes, cloud formations, volcanic eruptions, and dust deposits, which disrupt radiation at various temporal scales, from isolated events to monthly and annual variations. Understanding these phenomena is crucial for optimizing the use of photovoltaic systems in environments subject to these constraints.

In the atmosphere, the optical depth of aerosols indicates the extent to which these particles reduce the transmission of light. The higher the value, the more the light is absorbed or scattered by aerosols, thereby limiting its propagation. Aerosols scatter and absorb incoming solar light, thus reducing visibility. An aerosol optical depth (AOD) of less than 0.1 µm corresponds to a "clean" atmosphere, with clear blue skies and maximum visibility. As the Aerosol Optical Depth (AOD) increases to values such as 0.5, 3, or even beyond 10 µm, the concentration of aerosols becomes so dense that it obscures

sunlight. The primary sources of these aerosols include industrial pollution, wildfire smoke, storm-generated dust, sea salt, volcanic ash, and urban smog.

In photovoltaic fields, dust deposits on the surface of solar modules reduce the efficiency of the cells by blocking sunlight from passing through the glass. A clean and intact surface corresponds to a zero deposit thickness (0 μm), while deposit thicknesses of 0.5, 1, and 3 μm indicate an increasing accumulation of dust, progressively diminishing the transparency of the glass and exposure to solar radiation.

To effectively assess aerosol optical depth and the thickness of dust deposit layers influencing global solar radiation on photovoltaic cells, specific conditions must be met. These include accounting for clear or hazy sky conditions, utilizing low-power photovoltaic modules operating in parallel, installing solar systems side by side and oriented to the south, and conducting comparisons between a module kept consistently clean and another intentionally left dirty.

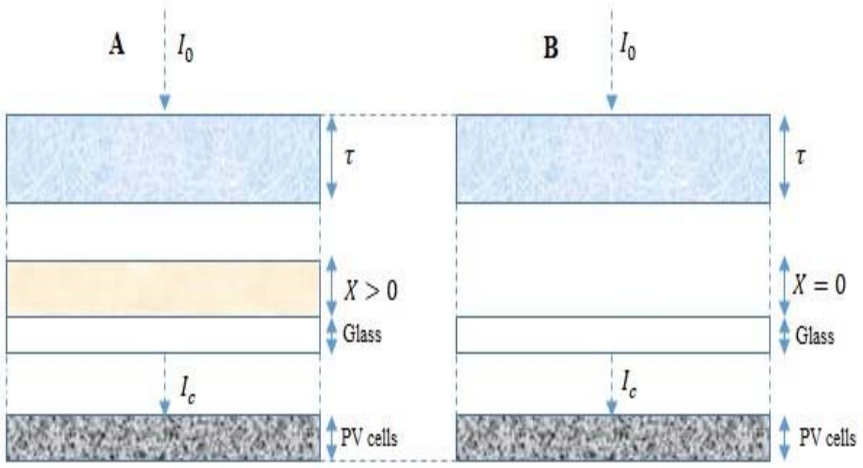

Figure 1: Analyzed physical model.

Table 1: Global distribution of solar intensity on Earth

Latitude (degre)	Relative air mass	Optical Path Length	Annual sunlight duration (hours)	Direct Solar Radiation (W/m²)	Reflected Solar Radiation (W/m²)	Diffuse Solar Radiation (W/m²)	Global Solar Radiation (W/m²)
0	2.5	0.27	4392	1000	0	0	1000
15	2.64	0.58	4348	697	42	36	775
30	2.78	0.97	4304	596	56	48	700
45	3.35	1.37	4260	500	70	60	630
60	3.93	2.53	4216	335	94	80	500
75	5.64	4.45	4172	165	117	100	382
90	7.36	6.99	4128	0	140	120	260

II. DESCRIPTION OF THE PHYSICAL MODEL

The analyzed physical model consists of two low-power solar systems, referred to as systems A and B. These systems are oriented due south at a 15° angle and consist of two solar modules with identical peak power, installed side by side. Each system includes two inverters of equal capacity and two energy measurement devices. The surface of photovoltaic module 'A' will remain uncleaned throughout the

study period, while the surface of photovoltaic module 'B' will be cleaned daily. System 'A' enables the measurement of daily, monthly, and semi-annual dust deposits while maintaining a null optical depth value. I_0 represents the daily extraterrestrial solar radiation, I_C is the global solar radiation reaching the PV solar cells, τ\tau is the optical thickness in the atmosphere, and X is the thickness of dust deposited on the surface of the PV module. At τ<0.1, it corresponds to a clear sky, while at τ>0.1, it corresponds to a sky loaded with desert aerosols or clouds. At X=0, the PV solar module is well-cleaned without dust on the surface, and at X>0, the solar module has a surface loaded with dust.

Numerical results

The optical depth equation is written as follows :

$$\tau = \left(\ln ln\left(\frac{I_{c/reference}}{I_{c\,real/B}}\right)\right) \quad (1)$$

The dust deposition equation is written as follows :

$$X = \ln ln\left(\left(e^{(-\tau)}\right)\left(\frac{I_{c/reference}}{I_{c\,real/A}}\right)\right) \quad (2)$$

Discretization of the optical depth equation :

$$\tau_{i,j}^{t+1} = \frac{\tau\left(\Delta t\left(\tau_{i+1,j+1}^{t} - \tau_{i+1,j-1}^{t} - \tau_{i-1,j+1}^{t} + \tau_{i-1,j-1}^{t}\right)\right)}{4\Delta x\Delta y} + \tau_{i,j}^{t} \quad (3)$$

Discretization of the dust thickness equation :

$$\chi_{i,j}^{t+1} = \chi\left(\Delta t\frac{\chi_{i+1,j+1}^{t} - \chi_{i+1,j-1}^{t} - \chi_{i-1,j+1}^{t} + \chi_{i-1,j-1}^{t}}{4\Delta x\Delta y}\right) + \chi_{i,j}^{t} \quad (4)$$

With:

$I_{c/référence} = \cos cos\,\theta\left(I_0 + 30e^{(0.75*L)} + 35e^{(0.72*L)}\right)$;

$\theta = 90^{o} - cos^{-1}(\sin sin\,\delta\ *\ \sin sin\,L\ +\ \cos cos\,\delta\ *\ \cos cos\,L\ *\ \cos cos\,hs\ )$;

$km = 0.274e^{(0.036*L)}$.

$k = 0.11e^{0.024*L}$;

$m = 2.5e^{0.012*L}$.

Where :

m : relative air mass;
k : extinction coefficient;
km: optical path length;
L: site latitude;
$I_{c\,real/A}$: real global solar radiation measured from solar system A;
$I_{c\,real/B}$: real global solar radiation measured from solar system B.

III. DISCUSSION

Solar obstacles refer to elements originating from both terrestrial and atmospheric sources that obstruct sunlight before it reaches the ground or a target surface. Understanding these obstacles is essential for accurately assessing the solar energy potential of a given area. Solar obstacles can be categorized into two main types: atmospheric obstacles and terrestrial obstacles.

Atmospheric solar obstacles are particles suspended in the atmosphere, such as clouds, precipitation, dust waves, and desert aerosols, which entirely or partially block sunlight before it reaches the ground. On the other hand, terrestrial solar obstacles consist of environmental elements, like desert dust, factories and fires, sea salt particles, volcanic ash, and smog, that settle on a solar surface and prevent the rays from reaching solar cells (Figure 2).

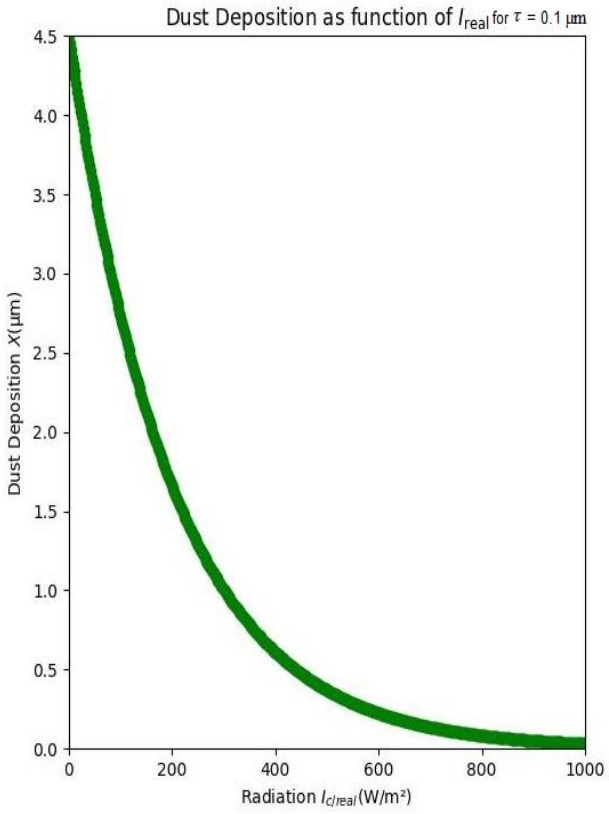

a

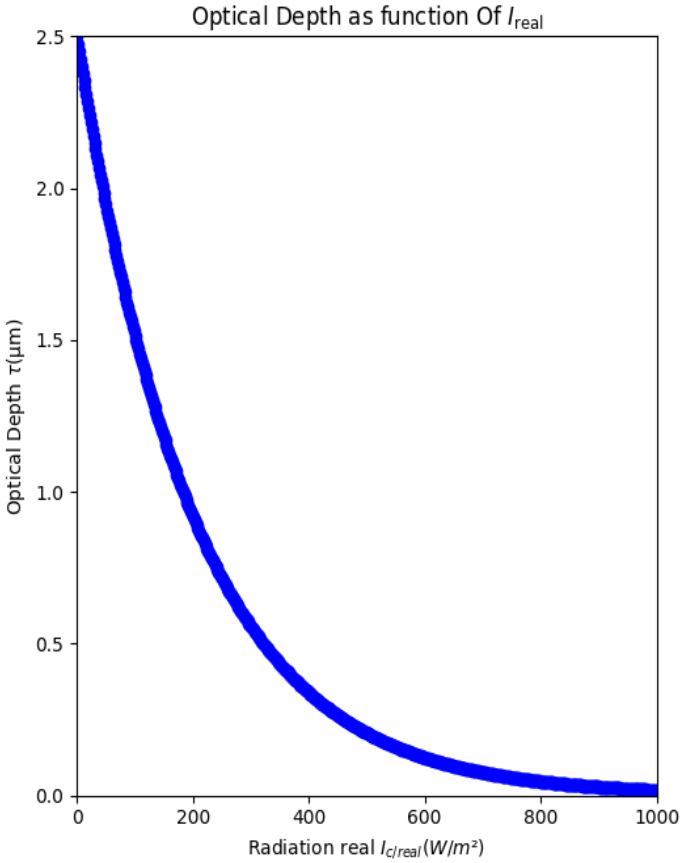

b

Figure 2-a,b: Impact of atmospheric and terrestrial solar obstacles on solar radiation.

The solar radiation received by a surface receives on the surrounding environment, which can vary at different times of the day. The impact of these obstacles on the performance of a solar installation can be substantial. Atmospheric solar obstacles, such as optical thickness, can affect performance rates by 86.64% to 98.77%, while terrestrial solar obstacles, such as dust deposits, can reduce performance by 58.83% to 84.85%.

Figure 3 demonstrates the direct and global solar radiation as a function of the sun's position in the northern and southern hemispheres. Positive signs (+) indicate the sun's position in the northern hemisphere, while negative signs (-) denote its position in the southern hemisphere. The Gaussian curve is used to observe the evolution of global solar radiation received by PV cells, regardless of the nature and thickness of atmospheric or terrestrial solar obstacles.

An analysis of Figure 3, the curve is divided into columns represented by standard deviations. The percentages indicate the values of global solar radiation corresponding to each standard deviation. The closer the global solar radiation is to the average, the more its value tends toward 0 W/m², signifying a significant presence of solar obstacles above the PV solar modules. Conversely, the farther the global solar radiation is from the average, the higher its value (greater than or equal to 700 W/m²), indicating a lower presence of solar obstacles.

Regarding radiation, the average standard deviation for dust deposits from terrestrial solar obstacles is 261.88 W/m², which influences solar radiation more than atmospheric solar obstacles, which average 442.45 W/m². The difference between the average standard deviations (atmospheric solar obstacle and

terrestrial solar obstacle) is 180.57 W/m². A low average standard deviation indicates a significant impact on solar radiation. Therefore, in the case of simultaneity (dusty surface and hazy sky), the average standard deviation is 180.61 W/m², which is lower than individual solar obstacles. This shows that the combined effect of solar obstacles, both atmospheric and terrestrial, has a greater impact on solar radiation compared to when these obstacles are assessed individually.

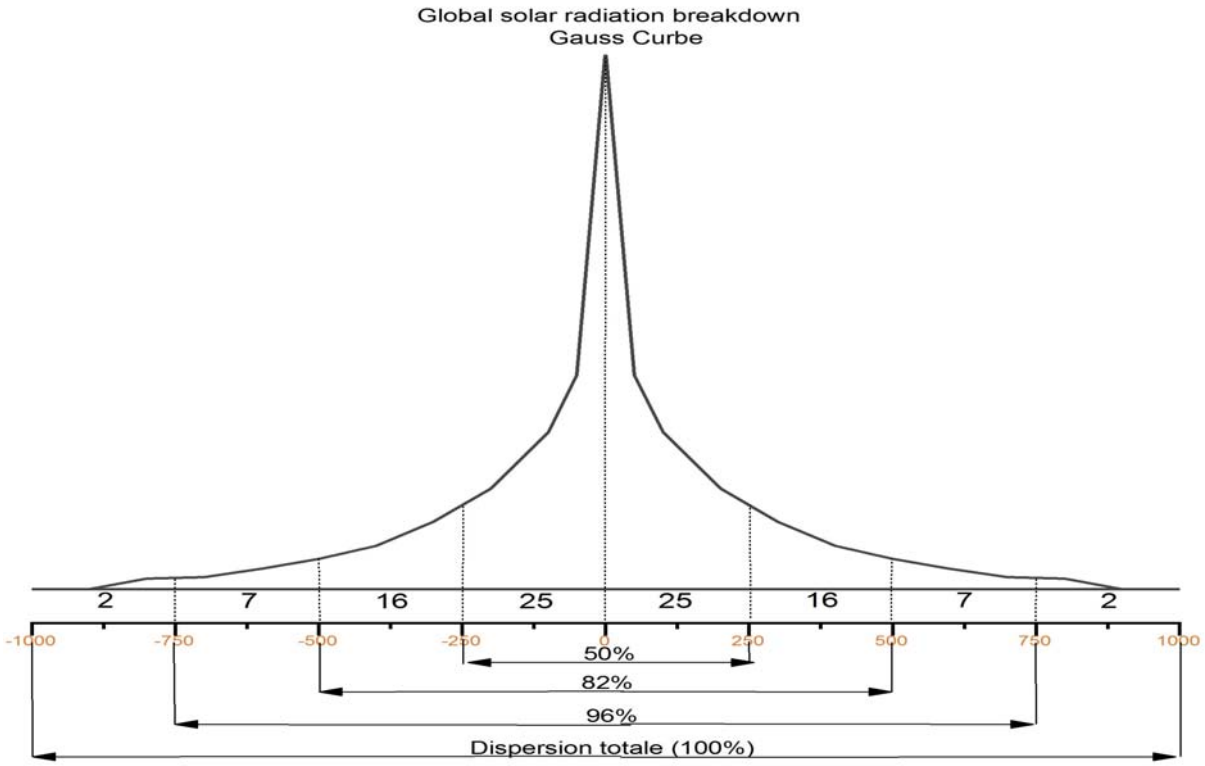

Figure 3: Gaussian curve illustrating the relationship between solar obstacles and global solar radiation.

Relative air mass indicates the amount of atmosphere a light ray must traverse before reaching a target on the ground. In Figure 4, at 0° latitude, solar rays pass through a thin atmosphere with a relative air mass (m) of 2.5. At 90° above the equator, the rays pass through three (3) times more atmosphere to reach an observer at this latitude, with a relative air mass of 7.36. In the context of solar obstacles, the intensity of light reaching the target is influenced both by the atmospheric conditions between the Sun and the instrument, and by the quantity of obstacles present along its path.

The extinction or attenuation coefficient is a parameter that quantifies how the optical thickness (or optical depth in astrophysics) of an aerosol varies with wavelength. At 0° latitude, solar radiation passes through a thin atmosphere, similar to relative air mass, giving an extinction coefficient of 0.11. In contrast, at 90° from the Earth's poles, the extinction coefficient value is 0.95, nearly 9 times that of the equator. At the equator, the extinction coefficient and relative air mass exhibit lower values, gradually increasing as latitude rises.

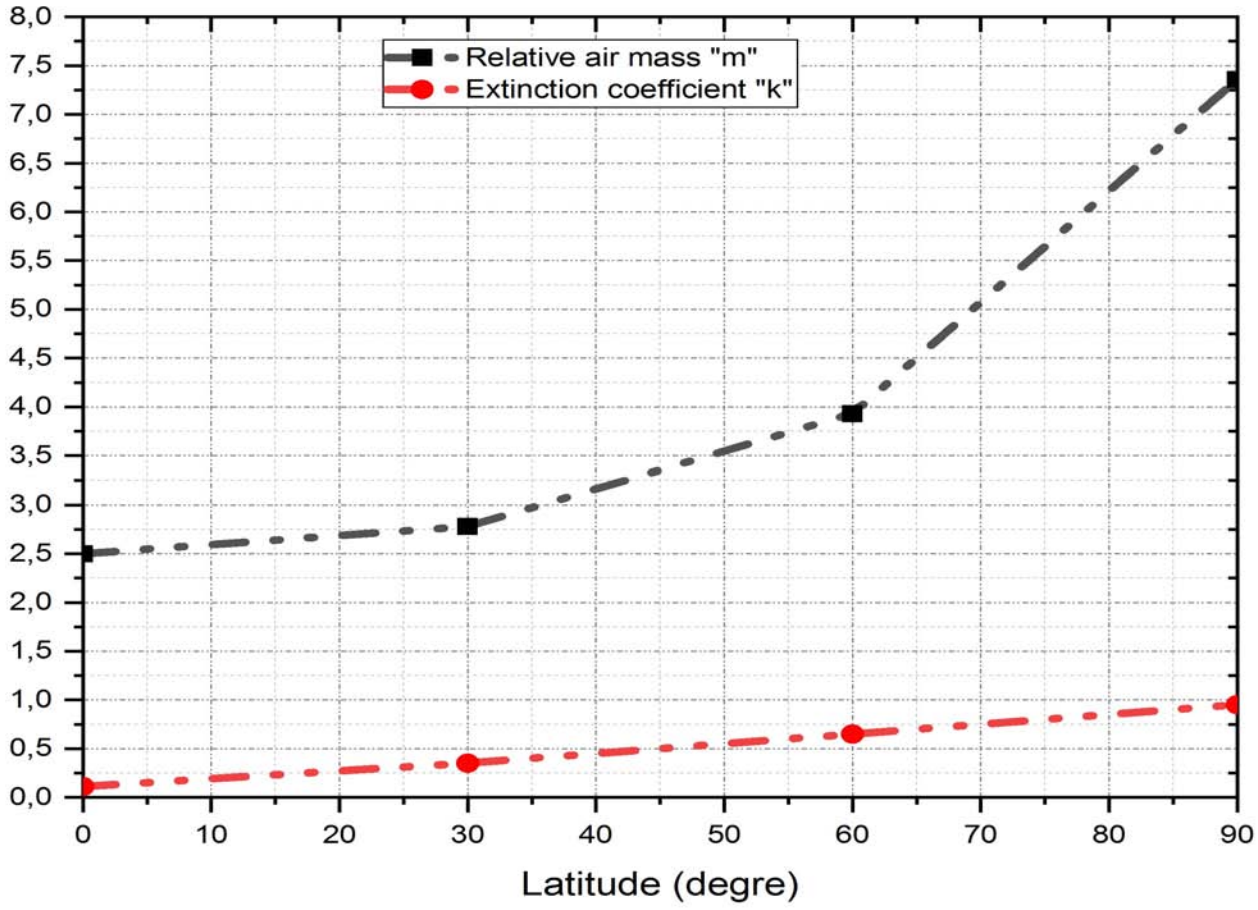

Figure 4: Chart of m and k as a function of Earth's latitude

Under a cloudless sky, solar radiation decreases as the optical path length "km" increases with Earth's latitude. At 0° latitude, the optical path length "km" is short, with a value of 0.274, explaining why global and direct solar radiation is maximum at the equator, with approximate values of 1000 W/m² (Table 1).

Direct solar radiation is more intense near the equator because solar light reaches it almost perpendicularly (Figure 5-a). These values gradually decrease as one moves away from the equator. Reflected solar radiation corresponds to a portion of the solar energy that, instead of being absorbed by the Earth's surface, is sent back into the atmosphere. This amount of reflected radiation increases with latitude, probably due to the increased snow cover and atmospheric reflection. Diffuse solar radiation results from the scattering of solar light by the atmosphere. Although generally stable, it can vary depending on local atmospheric conditions, such as cloud density or the presence of particles. Finally, global solar radiation, which combines direct, reflected, and diffuse radiation, demonstrates the decrease in direct radiation as latitude increases, a phenomenon partially compensated by diffuse and reflected radiation (Figure 5-b).

At the equator, diffuse solar radiation is almost zero, indicating that most solar light reaches the surface directly with minimal, tiny scattering. At a latitude of 45°, a significant portion of solar radiation is scattered by the atmosphere, thus increasing diffuse radiation. At a latitude of 60°, scattering becomes more intense, which significantly increases diffuse radiation. The combination of direct and diffuse radiation determines global solar radiation. Diffuse radiation values rise further from the equator because light travels through a thicker atmospheric layer, causing more scattering. At the equator, reflected radiation measures zero, likely due to the direct angle of solar incidence that minimizes

reflected light. At a latitude of 45°, a small portion of solar radiation is reflected, probably due to the increased reflective surfaces like clouds. And at, at latitude of 60°, reflected radiation increases even more, possibly related to the presence of snow or ice and increased atmospheric reflection.

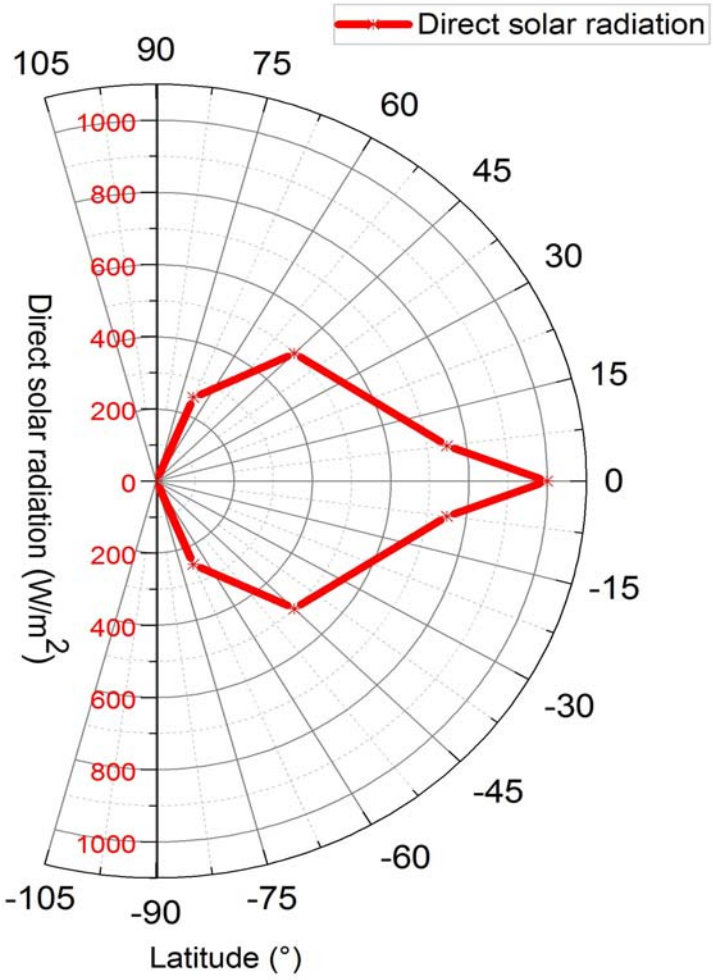

a

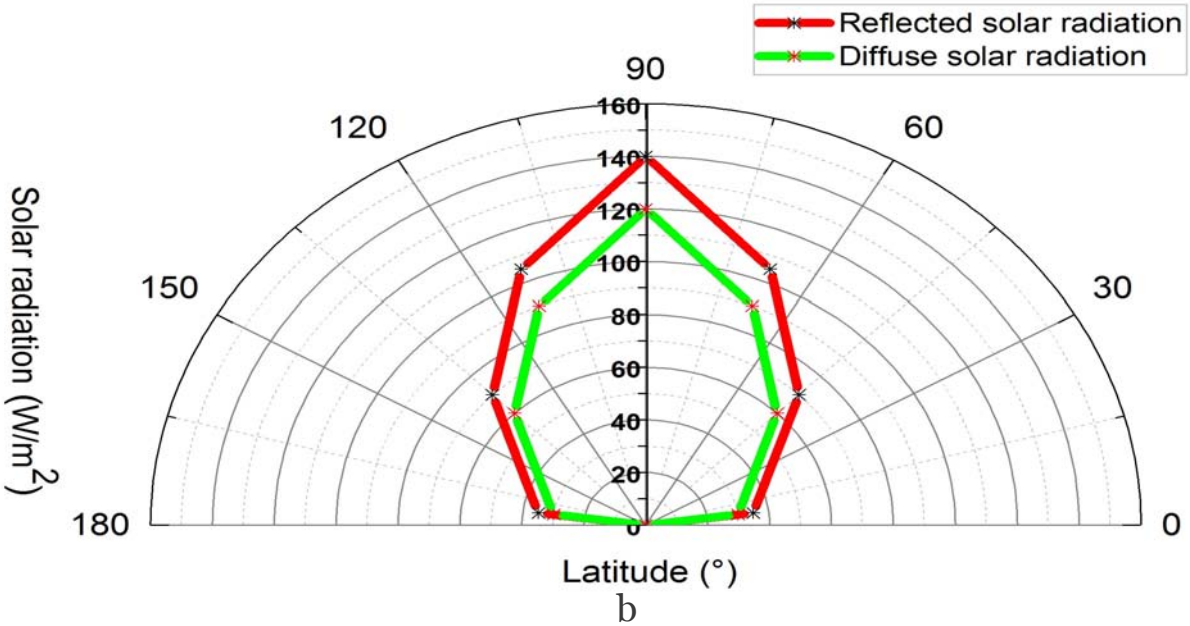

b

Figure 5-a,b: Changes in solar radiation across different latitudes.

Reflected radiation, which represents a portion of solar energy redirected back into the atmosphere, increases with latitude due to greater snow cover and enhanced atmospheric reflection. At lower latitudes, minimal reflection contributes to higher levels of global solar radiation. However, as latitude rises, reflection intensifies, reducing the direct absorption of solar energy and thereby diminishing global solar radiation.

These analyses demonstrate how each component of solar radiation-direct, diffuse, and reflected-interacts to produce the observed variations in global radiation across different latitudes. The angle of incidence of solar light on the Earth's surface is directly influenced by latitude and the time of day. For a given latitude, this angle changes throughout the day due to the Earth's rotation and throughout the seasons due to the Earth's revolution around the Sun.

At high latitudes, the atmosphere absorbs and scatters a greater portion of solar radiation, which reduces direct radiation while increasing diffuse radiation. These changes significantly impact the climate patterns observed across different latitudes. Equatorial regions benefit from warmer and more stable temperatures, while polar areas are colder and experience more pronounced seasonal variations. For solar panel projects, these data are essential for optimizing the angle and position of the panels based on latitude to maximize solar radiation capture.

The optical path length is crucial in the intensity and diffusion of solar radiation with latitude. The observed variations are logical, as the angle of incidence of solar light in the atmosphere directly affects the optical path length. The more oblique the light penetrates the atmosphere, the longer the optical path, leading to increased absorption and scattering of solar rays.

From the equator, where the optical path is shortest, to higher latitudes, where it lengthens, this directly impacts the observed direct and global solar radiation. The values show a decrease in direct solar radiation with increasing latitude and variations in diffuse radiation. These data help to understand the distribution of solar energy by latitude, which is essential for understanding the differences in sunlight across the Earth.

Regarding calculations and modeling, it is crucial to consider the variations in optical path length and solar radiation according to Earth's latitude. These variations are essential for understanding how solar obstacles influence the amount of radiation reaching photovoltaic cells. The variation in extinction coefficients clearly demonstrates that polar regions undergo significantly higher attenuation of solar radiation compared to equatorial areas.

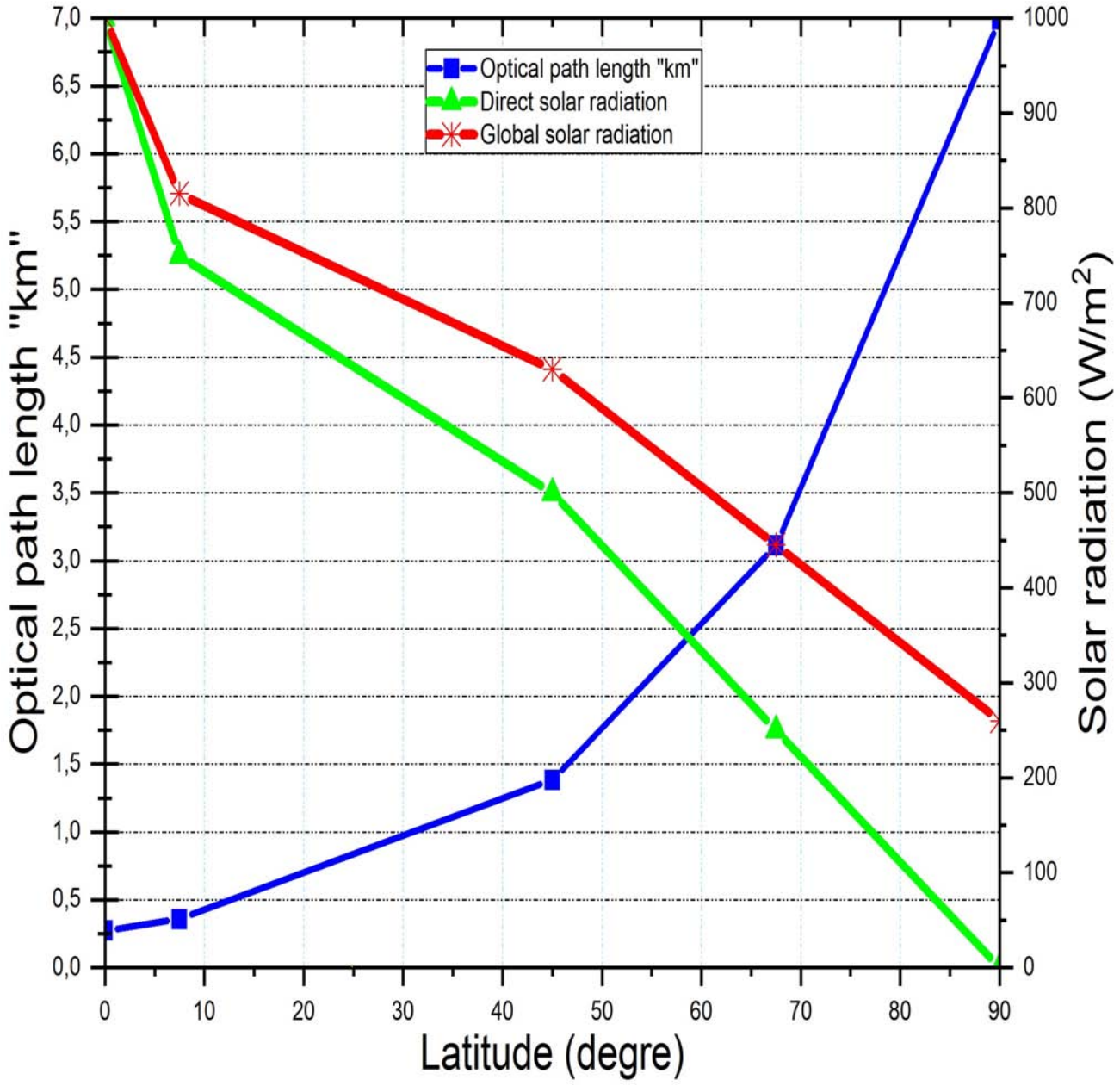

Figure 6: Impact of Latitude on the Distribution of Solar Obstacles

It shows that as latitude increases, atmospheric and terrestrial solar obstacles become more significant, reducing the efficiency of solar installations. It is also interesting to note that seasonal fluctuations impact the amount of available solar radiation. For example, during winter, polar regions receive much less solar radiation due to the low angle of incidence and increased solar obstacles.

The Earth's elliptical orbit around the Sun directly affects both the intensity and distribution of solar radiation received on its surface. Indeed, the Earth's position in its orbit and the tilt of its rotational axis influence the amount of sunlight that reaches different regions throughout the year. This phenomenon is responsible for the seasonal variations in sunlight. In this annual round of 365 days, the Earth completes a full rotation on its axis in 24 hours. The curves in Fig. 7 shows the variation of daily sunlight duration from the equator to the Earth's poles. This north-south axis is tilted at an angle of 23°27′ relative to the perpendicular direction to the plane of the Earth's orbit around the Sun. This

tilt remains constant throughout the Earth's orbit and is responsible for the seasonal variations, with opposite effects in the northern and southern hemispheres. Thus, during the winter months (December 21 to March 21) in the northern hemisphere, Sunlight is relatively short, and the Sun does not climb very high in the sky.

From March 21 to September 21, marking the summer months, the situation reversed : the northern hemisphere is tilted toward the Sun. The days are longer than the nights in the northern hemisphere, and the incident radiation is closer to vertical, giving a maximum sunlight duration of over 16 hours at the latitude of 90° – 23°27′. At the spring and autumn equinoxes (March 21, September 21), the radiation is perpendicular to the equator (latitude 0°), and all around the globe, the days and nights are of equal length. At the summer solstice (June 21), the Earth is tilted toward the solar rays, and at noon, these rays are perpendicular to the Tropic of Cancer (latitude 23°27′ N). Sunlight duration is maximum in the northern hemisphere and minimum in the southern hemisphere (fig.1). The Sun never sets in the regions of the globe located within the Arctic Circle (which is 23°27′ below the 90° latitude of the North Pole). The evolution of sunlight from the equator to the North and South Poles follows a spiral trajectory in the shape of a snail shell.

At the winter solstice, sunlight duration is shortest in the northern hemisphere and, conversely longest in the southern hemisphere. Thus, from the autumn equinox (September 21) at noon at latitude 0°, the duration of sunlight decreases over the months until it reaches its shortest peak on December 21 in the northern hemisphere with 4 hours at 90° – 23°27′, then increases again until the spring equinox. At the summer solstice, the progression of sunlight duration with latitude is the opposite of that in winter. Sunlight duration increases with latitude and peaks on June 21, marking the summer solstice, the longest day in the northern hemisphere with more than 16 hours at 90° – 23°27′. The curve in Figure 8 illustrates the variation in annual sunlight duration, which decreases progressively from the equator toward the Earth's poles. At the equator, the annual sunlight duration reaches its maximum of 4,392 hours. The spiral shape of the curve shows a constant decrease from the equator to the North and South Poles. The shortest annual sunlight duration on Earth, totaling 4,055 hours, is observed at latitudes 90° – 23°27′ near the North and South Poles.

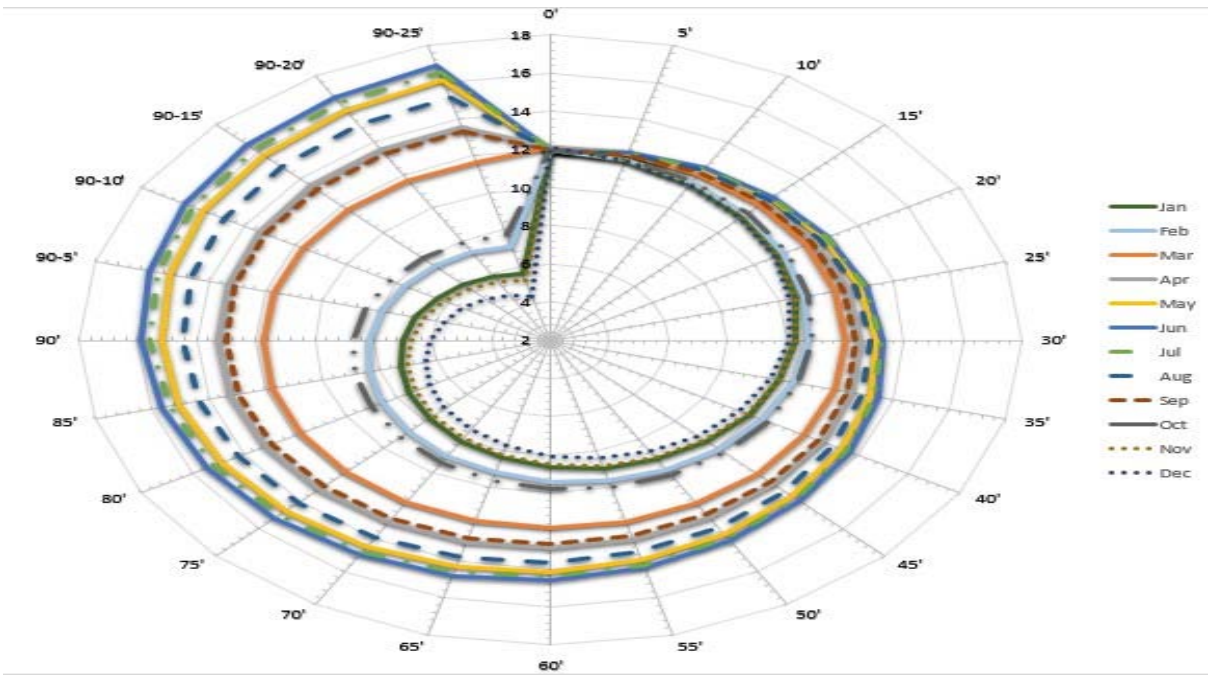

a

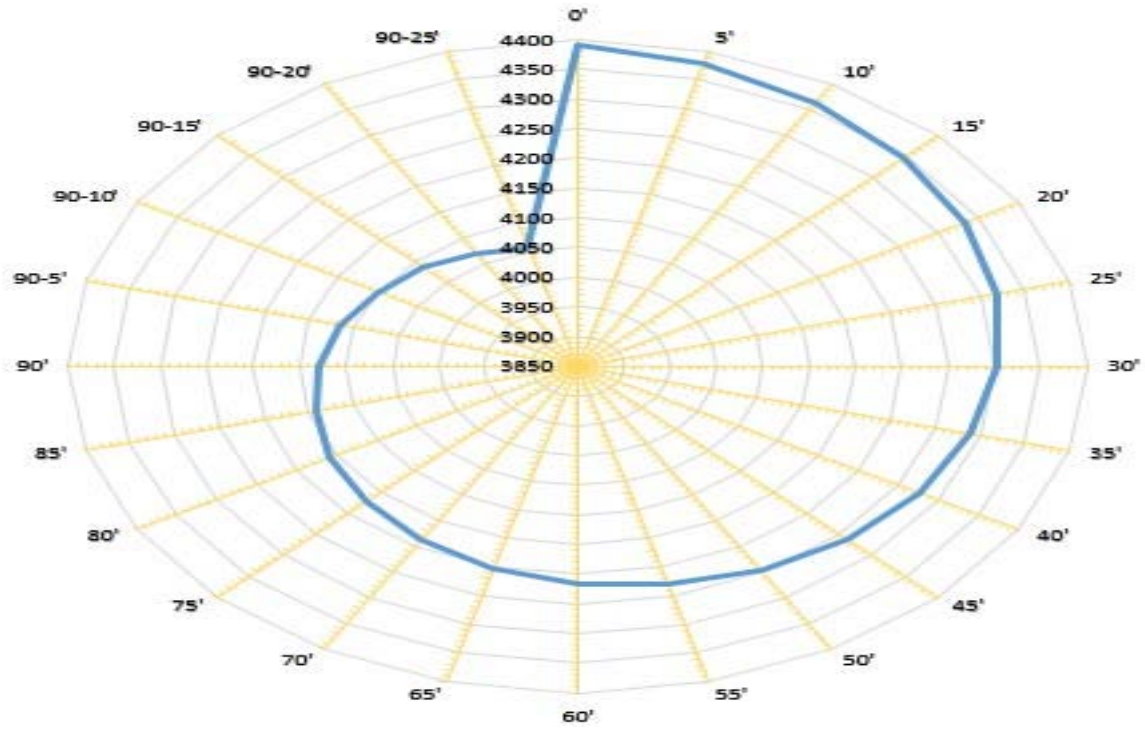

b

Figure 7-a,b: Changes in Daily and Annual Sunlight from the Equator to the Poles

The study of solar obstacles has critical practical applications, particularly for optimizing solar panel projects. By considering the optical thickness of aerosols and dust deposits, it is possible to determine the ideal angles and positions of solar panels to maximize energy efficiency. Additionally, managing these obstacles, such as reducing industrial particle emissions or regularly cleaning solar surfaces, can significantly improve the performance of solar installations.

Taking into account both atmospheric and terrestrial solar obstacles is crucial for a precise assessment of a region's solar energy potential. Studies show that the impact of these obstacles varies by latitude, with more pronounced effects at higher latitudes. A better understanding of these phenomena allows for developing effective mitigation strategies and optimization of solar energy use, contributing to a more sustainable future.

IV. CONCLUSION

This study highlighted the importance of atmospheric and terrestrial solar obstacles in evaluating the performance of photovoltaic installations in arid regions. Using PV solar systems, we demonstrated that desert aerosols and dust deposits can significantly reduce the amount of solar radiation reaching photovoltaic cells.

The findings highlight that aerosol optical thickness and dust accumulation on solar surfaces are key factors in the reduction of global solar radiation. Simulations showed that solar obstacles impact energy performance differently depending on whether they occur individually or simultaneously. The combined presence of multiple obstacles results in a more pronounced reduction in energy performance.

These observations provide a solid foundation for optimizing photovoltaic systems, particularly concerning the location, orientation, and maintenance of solar panels. The proposed mitigation

strategies can help maximize the efficiency of solar installations by reducing the negative impact of solar obstacles.

In conclusion, this research contributes to understanding the interactions between solar obstacles and photovoltaic systems, offering promising prospects for improving solar energy capture in arid environments.

REFERENCES

1. Ilboudo, W.D.A. (2024) Physical Analysis of Atmospheric Phenomena Associated with Climatic Storms: Approach Study Related to Climate Change on Earth. Atmospheric and Climate Sciences, 14, 355-367. https://doi.org/10.4236/acs.2024.144022
2. Ilboudo, W.D.A., Yamba, K., Koumbem, W.N.D. and Ouédraogo, I. (2024) Numerical Models and Methods of Atmospheric Parameters Originating in the Formation of the Earth's Climatic Cycle. Atmospheric and Climate Sciences, 14, 277-286. https://doi.org/10.4236/acs.2024.142017
3. Borel, L. and Favrat, D. (2005) Thermodynamique et énergétique (Volume 1) presses polytechniques.https://www.epflpress.org/produit/332/9782880745455/thermodynamique-et-energetique-volume-1
4. Jensen, W.B. (2003) The Universal Gas Constant R. Journal of Chemical Education, 80, 731-732. https://doi.org/10.1021/ed080p731
5. [5] Saha, K. (2008) The Earth's Atmosphere: Its Physics and Dynamics. Springer-Verlag, Berlin. http://gnssx.ac.cn/docs/The%20Earths%20Atmosphere.%20Its%20Physics%20and%20Dynamics%20(Kshudiram%20Saha)%20(z-lib.org).pdf
6. Keckhut, P., Hauchecone, A., Claud, C., Funatsu, B.M., et al. (2013) Refroidissement de la stratosphère: Détection réussie mais quantification encore incertaine. La Météorologie, 82, 31-37. https://doi.org/10.4267/2042/51479
7. Ilboudo, W.D.A., Ouedraogo, I., Koumbem, W.N.D. and Kieno, P.F. (2021) Modeling the Impact of Desert Aerosols on the Solar Radiation of a Mini Solar Central Photovoltaic (PV). Energy and Power Engineering, 13, 261-271. https://doi.org/10.4236/epe.2021.137018.
8. Ouedraogo, I., Ilboudo, W.D.A., Koumbem, W.N.D. and Ouedraogo, A. (2022) Experimental Investigation of the Structural Coloured Reflections from Elytra of the Megacephala Regalis Citernii. American Journal of BioScience, 10, 186-190.
9. Koumbem, W.N.D., Ouédraogo, I., Ilboudo, W.D.A. and Kieno, P.F. (2021) Numerical Study of the Thermal Performance of Three Roof Models in Hot and Dry Climates. Modeling and Numerical Simulation of Material Science, 11, 35-46. https://doi.org/10.4236/mnsms.2021.112003.
10. Ilboudo, W.D.A. (2021) Impact of Desert Aerosols on the Solar Radiation of a Solar Central Photovoltaic (PV): A Modelling Approach. Novel Perspectives of Engineering Research, 9, 149-160. https://doi.org/10.9734/bpi/nper/v9/2048B.

This page is intentionally left blank

Geospatial Modeling of Urban Expansion Scenarios and their Influence on Local Development in the Quevedo Canton with a 2030 Vision

José Luis Muñoz, Jefferson Sánchez & Luis Veas Triana

Quevedo State Technical University

ABSTRACT

Quevedo's urban growth has evolved rapidly due to population growth, economic development, and land use changes. This study analyzed this expansion through geospatial modeling, identifying growth patterns and projecting scenarios until 2030. A methodology based on Markov Chains and IDRISI software was used, integrating geospatial and temporal data obtained from satellite images, official cartography and socioeconomic records. The application of Geographic Information Systems (GIS) made it possible to determine areas with greater urbanization potential, considering factors such as land use, proximity to road infrastructure and population density. The results showed a sustained urban growth, with an increase of 32% (1,104 ha) of the urban area projected for 2030. At the same time, there was a 44.9% reduction in agricultural areas (6,040.4 ha) and a 45.0% reduction in livestock areas (1,360.9 ha), which could generate land use conflicts and pressure on natural resources. In addition, uncontrolled urban sprawl was identified as a risk to equitable access to basic services, infrastructure and security. It was concluded that it is essential to implement sustainable land-use planning strategies that regulate sprawl and balance urban growth with environmental conservation and land productivity. The development of controlled expansion plans that prioritize the provision of basic services and the protection of strategic agricultural zones is recommended, guaranteeing a planned and sustainable urban development.

Keywords: territorial planning, spatial sampling, GIS, urban growth, land use planning.

Classification: LCC Code: GE170-190

Language: English

Great Britain Journals Press

LJP Copyright ID: 925664
Print ISSN: 2631-8490
Online ISSN: 2631-8504

London Journal of Research in Science: Natural & Formal

Volume 25 | Issue 6 | Compilation 1.0

Geospatial Modeling of Urban Expansion Scenarios and their Influence on Local Development in the Quevedo Canton with a 2030 Vision

José Luis Muñoz [α], Jefferson Sánchez[σ] & Luis Veas Triana[ρ]

SUMMARY

The urban growth of Quevedo has evolved rapidly due to population growth, economic development, and land-use changes. This study analyzed this expansion using geospatial modeling, identifying growth patterns and projecting scenarios through 2030. A methodology based on Markov Chains and IDRISI software was used, integrating geospatial and temporal data obtained from satellite images, official cartography, and socioeconomic records. The application of Geographic Information Systems (GIS) allowed the identification of areas with the greatest potential for urbanization, considering factors such as land use, proximity to road infrastructure, and population density. The results showed sustained urban growth, with a 32% increase (1,104 ha) in the projected urban area by 2030. At the same time, a 44.9% reduction in agricultural areas (6,040.4 ha) and a 45.0% reduction in livestock areas (1,360.9 ha) were recorded, which could generate land-use conflicts and pressure on natural resources. Furthermore, uncontrolled urban expansion was identified as a risk to equitable access to basic services, infrastructure, and security. It was concluded that it is essential to implement sustainable land-use planning strategies that regulate expansion and balance urban growth with environmental conservation and soil productivity. The development of controlled expansion plans that prioritize the provision of basic services and the protection of strategic agricultural areas, guaranteeing planned and sustainable urban development, is recommended.

Keywords: territorial planning, spatial sampling, GIS, urban growth, territorial planning.

*Author*αασ ρ: Quevedo State Technical University - UTEQ.

ABSTRACT

Quevedo's urban growth has evolved rapidly due to population growth, economic development, and land use changes. This study analyzed this expansion through geospatial modeling, identifying growth patterns and projecting scenarios until 2030. A methodology based on Markov Chains and IDRISI software was used, integrating geospatial and temporal data obtained from satellite images, official cartography and socioeconomic records. The application of Geographic Information Systems (GIS) made it possible to determine areas with greater urbanization potential, considering factors such as land use, proximity to road infrastructure and population density. The results showed a sustained urban growth, with an increase of 32% (1,104 ha) of the urban area projected for 2030. At the same time, there was a 44.9% reduction in agricultural areas (6,040.4 ha) and a 45.0% reduction in livestock areas (1,360.9 ha), which could generate land use conflicts and pressure on natural resources. In addition, uncontrolled urban sprawl was identified as a risk to equitable access to basic services, infrastructure and security. It was concluded that it is essential to implement sustainable land-use planning strategies that regulate sprawl and balance urban growth with environmental

London Journal of Research in Science: Natural & Formal

conservation and land productivity. The development of controlled expansion plans that prioritize the provision of basic services and the protection of strategic agricultural zones is recommended, guaranteeing a planned and sustainable urban development.

Keywords: territorial planning, spatial sampling, GIS, urban growth, land use planning.

I. INTRODUCTION

In Latin America, population growth in urban areas dates back to the 1970s, when free market policies were implemented throughout the region and international organizations encouraged population concentration in cities with a view to their sustainability (Duque, 2021). (Vega and Cánovas, 2023). This measure facilitated the strengthening of the real estate sector and allowed power groups to exert their influence on the areas to be urbanized and the direction of urban growth (Yacila, 2021). Furthermore, uncontrolled urban expansion led to the loss of green areas and natural spaces, as well as an increased demand for basic services such as drinking water, energy, and transportation (Koprowska et al., 2020). (Maeso and Hidalgo, 2020). This raises questions about the future challenges of land use planning, the provision of basic services, environmental preservation, and economic and social development (Long et al., 2021). (Hendricks and Van Zandt, 2021) (Wang et al., 2022).

Population growth in Latin America and the Caribbean shows an almost perfectly arithmetic trend, according to World Bank data collected from 1970 to 2020 (García et al., 2023). This region showed accelerated population growth, going from 300 million to more than 650 million inhabitants. Regarding the percentage of urban population in relation to the total, Latin America and the Caribbean increased their urban population from 57% to 81% (Sandoval and Sarmiento, 2020). (Giorguli et al., 2022) . In the case of Ecuador, the population increased from approximately 5 million to almost 18 million today, with the urban population increasing from 39% to 64% nationwide (Guerrero, 2022). (Roldan et al., 2024). These data show that in the last decade the pressure on urban and developable land has been increasing (Duque and Montoya, 2021). The rapid growth of Ecuadorian cities has generated pressure on natural resources and urban infrastructure, negatively affecting the quality of life of their inhabitants (Mena et al., 2022).

Quevedo is a dynamic, constantly evolving city that has witnessed a dizzying urbanization process in recent decades, becoming one of the ten most populated cities in the country. The city's uncontrolled expansion has resulted in the loss of green areas and natural spaces, as well as increased pressure on basic services and existing infrastructure (Coello et al., 2024) . Population densification in urban areas has contributed to traffic congestion, air pollution, and the degradation of the natural environment (Mena et al., 2022). The demand for housing, services, and employment continues to rise, leading to increased pressure on available resources and an unequal distribution of the benefits of urban development (Mejía et al., 2024) . Furthermore, the lack of adequate planning has exacerbated socioeconomic segregation and the vulnerability of certain population groups.

Urban growth without adequate planning leads to the overexploitation of resources, affecting the sustainability of cities (Duranton and Puga, 2023). This phenomenon highlights the need to rethink urban development and resource management to promote a more equitable and sustainable environment (Domingo et al., 2021). Therefore, in the formulation of territorial planning plans, it is essential to carry out spatial analyses that allow defining suitable areas for urban growth in line with the characteristics of the territory (Sotelo, 2020) . (Otero and Llop, 2020) . These analyses may include techniques such as multicriteria evaluation, spatial interpolation analysis, surface modeling, accessibility and connectivity analysis, among others (Fernandez, 2020). (Sisman and Aydinoglu, 2020) (Sadooghi et al., 2022).

Multi-criteria assessment is an essential tool in urban planning, as it allows for the consideration of various variables such as topography, availability of basic services and proximity to protected areas to identify the most suitable areas for urban development. (Sagastume et al., 2022). This approach facilitates decision-making in complex and poorly structured problems, providing a solid basis for sustainable land use planning (Cardoso and Carñel, 2022). Similarly, spatial interpolation analysis is equally valuable, as it allows estimating values in locations without direct data, such as population density or service demand (Gold, 2020). (Du et al., 2020). This process involves the manipulation of spatial information to extract new meaningful data, using techniques that generate continuous surfaces from existing data points (Barragán, 2022) . Furthermore, surface modeling is crucial for generating three-dimensional representations of the territory (López, 2023) , facilitating the visualization and understanding of its morphology and relief (Crissi, 2021) . These representations are essential for analyzing phenomena such as elevation, slope, and other geographical aspects that influence urban planning (Cahe and de Prada, 2024).

The use of advanced geospatial modeling techniques, especially Geographic Information Systems (GIS), is presented as a powerful tool for analyzing urban growth patterns, identifying risk areas, and evaluating development scenarios (Li et al., 2020). These tools allow the cartographic representation of complex urban phenomena and support informed decision-making in territorial planning (Sassi et al., 2020). (Mamonov et al., 2021) . Thus, the integration of these methodologies into urban expansion research not only enriches scientific knowledge in the field of urban planning but also provides valuable information for the formulation of effective and sustainable urban policies and strategies (Cabrera et al., 2020). (Lytvynchuk et al., 2020).

Lack of familiarity with these spatial analysis methodologies can lead to the formulation of unclear and superficial Territorial Plans, which in turn can result in empirically based territorial classification and delimitation driven by political or economic interests (Alvarado and Jiménez, 2020). It is essential that those responsible for formulating these plans have the knowledge and tools necessary to carry out rigorous, data-driven spatial analyses that enable informed and sustainable decisions regarding territorial development (Koldasbayeva et al., 2024). (Zhang et al., 2024) .

In this context, there is a need to delve deeper into the patterns and processes of urban expansion in Quevedo, as well as their impact on local development and the quality of life of its inhabitants. This understanding is essential for guiding policies and measures that foster sustainable, equitable, and resilient urban growth in the city moving forward. This research seeks to provide tools and knowledge that enable more effective and sustainable urban planning in Quevedo. By modeling different urban expansion scenarios using geospatial techniques, planners and decision-makers will be able to visualize and assess various growth trajectories and their potential impacts.

1.1 Study area

The city of Quevedo is located in the northern part of the province of Los Ríos, belonging to the Costa region of continental Ecuador, with geographical coordinates 1 °02' 00" South latitude and 79 °27 '00" West longitude, at an altitude of 74 meters above sea level (Fig. 1). Its territorial extension is 3125.06 hectares. It borders geographically with the cantons: Buena y Fe Valencia (North), Mocache and Ventanas (South), Quinsaloma and Ventanas (East), El Empalme of the province of Guayas (West).

(a) (b)

Figure 1: Geographic location of the city of Quevedo: (a) boundaries of the urbanized area of the city of Quevedo; (b) panoramic view of the urban structure of Quevedo and its main tributary.

II. METHODOLOGY

2.1 Population and sample

Population

The study population for this research corresponds to all properties located in the Quevedo canton, Ecuador. Quevedo, a medium-sized city in the Los Ríos province, which according to official data from the National Institute of Statistics and Census (INEC, 2022), has a population of 206,008 inhabitants and is home to a diversity of properties that span both urban and rural areas within the canton. These properties exhibit a variety of distinguishing characteristics, including their geographic location in the Ecuadorian coastal region, their diverse land use, ranging from residential to agricultural and industrial, as well as their size and morphology, which can vary from small residential plots to large tracts of land. Furthermore, the property population is distributed across areas with different levels of access to basic services and urban amenities, reflecting the complexity of Quevedo's urban structure.

Within the context of a non-experimental documentary or bibliographic design, the units of analysis used will encompass a variety of sources, such as official documents, municipal records, previous studies, and maps, to gain a comprehensive understanding of urban expansion and its impact on local development in Quevedo.

According to the urban cadastre of the Decentralized Autonomous Government (GAD) of the Quevedo Canton, a total of 70,000 properties were identified that belong to the urban area of the "Quevedo" canton.

Sample

The determination of the population subset for this research will be based on stratified random sampling, considering the different urban and rural areas within the Quevedo canton. The objective is

to obtain a representative sample that reflects the diversity of property characteristics throughout the study area.

To determine a representative sample of a population of 70,000 properties in the Quevedo canton, we can use several sampling methods. One of the most common methods is simple random sampling, which involves randomly selecting a specific number of elements from the population to form the sample.

To establish the sample size, the sample size calculation formula for finite populations will be used, which is expressed as:

$$x = \frac{z^2 Npq}{e^2(N-1) + z^2 pq} \quad (1)$$

Where:

N = is the sample size N is the population size p is the probability of success

q = is the probability of failure (1 – p)

z = is the standard normal value corresponding to the desired confidence level.

S = is the estimate of the population standard deviation.

e = is the maximum admissible error (estimation error)

For the z value, a 95% confidence level was assumed, giving a value of 1.96. For p, a probability of 50% was assumed, so q will also have a value of 50%; for E, an error of 5% was estimated.

The formula was applied to determine the sample size required to achieve a specific confidence level and margin of error. Once the sample size was calculated, the properties included in the sample were randomly selected.

2.2 Research instruments

The research instruments used in this study included questionnaires, interview guides, and geospatial analysis tools. Each is detailed below:

1) Questionnaires: Structured questionnaires were designed to collect quantitative data from local residents and property owners in Quevedo. These questionnaires contained closed-ended and open-ended questions about perceptions of urban sprawl, access to basic services, quality of life, and other relevant variables. Questions were guaranteed to be clear, relevant, and unbiased to elicit accurate and meaningful responses.
2) Interview Guides: Semi-structured interview guides were developed to conduct in-depth interviews with municipal officials, urban planning experts, and community leaders. These guides included open-ended questions and topics designed to explore in-depth policies, practices, and perceptions related to urban development in Quevedo, ensuring the collection of detailed and relevant information.
3) Geospatial Analysis Tools: Geospatial analysis tools, such as Geographic Information Systems (GIS), were used to visualize and analyze spatial data on urban expansion, land use, and infrastructure distribution in Quevedo. Software such as QGIS, ArcGIS, and IDIRIS were used, using the Lean Chain Modeler module and applying the Markov Chain. These tools allowed for the integration and analysis of georeferenced data to identify spatial patterns and trends in urban development.

4) Procedural diagram: Schematically, the procedure executed by the Markov Chain model (MC-Markov) demonstrates the relationship between input information and execution in a different pair run. For the first execution of the process, stages 2010 and 2020 are established, which will serve as elementary intervals for the calibration process. After that, the extrapolation to the 2020-2030 validation period is generated.

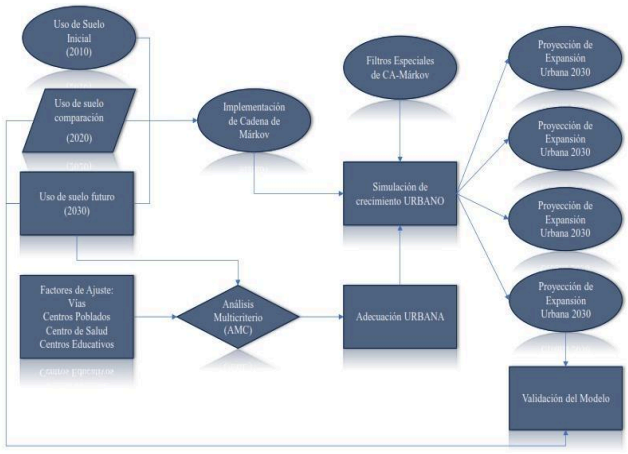

Figure 2: Execution scheme of the process with CA-Markov.

Once the system is ready, a validation process is generated that evaluates simulated urban growth by comparing it with the existing urban expansion during that period (2020-2030). The subsequent execution uses the 2010 and 2030 stages as a calibration process and, based on this, performs extrapolations for three sequential projections segmented into 20-year periods: 2030-2050, 2050-2070, and 2070-2090.

To ensure the reliability and validity of the research instruments, the following criteria will be followed:

a. Reliability: The questionnaires and interview guides were pilot-tested with a representative sample group before their full implementation. In addition, an inter-interviewer consistency analysis will be conducted to ensure consistency in the application of the interview guides.
b. Validity: A thorough review of existing literature and relevant documents was conducted to ensure the validity of the questions and topics included in the questionnaires and interview guides. In addition, feedback from experts in the field of study was sought to validate the content of the instruments. Attention was paid to question formulation to avoid bias and ensure that they adequately capture the constructs intended to be measured.

2.3 Data collection

Once the specific objectives of this research were established, relevant information sources were identified. This included consulting official documents, institutional reports, previous studies, statistics, databases, academic literature, among other relevant resources. Subsequently, the appropriate data collection instruments were selected to obtain the required information. Techniques such as surveys, direct observation, and document review were employed. These strategies made it possible to collect the data necessary to answer the research questions.

Primary data collection for this research was carried out through a series of meticulously planned activities. First, a physical and digital inventory of all cartographic information that influences or generates interest in the application or determination of urban expansion projections will be conducted, focusing on the entire urban and peri-urban area of the Quevedo canton. This will address

aspects relevant to the research process, such as the history of urban expansion, geographic layers of basic service coverage and access to roads and towns, and existing urban amenities in the city.

2.4 Data source

Municipality of Quevedo

Data were obtained on urban zoning, current land use, and urban and peri-urban areas. This information made it possible to establish the areas authorized for urban development and compare their expansion in recent years.

Table 1: Data collected - GADM Quevedo

Type of Information	Data Purpose	Data Format	Analysis Tools Used
Urban zoning, land use, urban and peri-urban areas	Determine authorized areas for urban development and analyze expansion trends in the canton.	Shapefiles, vector maps at 1:1000 scale, structured tables.	ArcGIS, QGIS
Orthophotography	Obtain spatial precision over urban and peri-urban areas	Orthophotograph in ECW format at a scale of 1:1000 from 2015	ArcGIS, QGIS

Source: Decentralized Autonomous Municipal Government of Quevedo Canton (GADMQ, 2024).

Military Geographic Institute (IGM)

It provided base mapping and detailed geospatial data for the Quevedo area, such as topography and land-use layers at a working scale of 1:25,000 in geodatabase (GDB) format, which were transformed into shapefile (SHP) format for processing. This data was used to identify areas that have experienced significant land-use change and are therefore prone to urban expansion.

Table 2: Data collected - Military Geographic Institute (IGM)

Type of Information	Data Purpose	Data Format	Analysis Tools Used
Basic mapping, topography and land use layers	Establish the geographical basis for the analysis of urban growth, including physical characteristics of the territory	BDD - Topography and land use shapefiles, raster maps at a scale of 1:25000	QGIS

Source: Military Geographic Institute (IGM, 2024)

National Institute of Statistics and Census (INEC)

It provided sociodemographic and economic data that complemented the spatial analysis for both 2010 and 2020, allowing for the correlation of growth areas with variables such as population density, demand for services, and settlement growth.

The cartographic information, developed and managed by the National Institute of Statistics and Census (INEC), provides up-to-date and essential data for modeling urban expansion scenarios in the Quevedo canton, thus enriching the analysis of spatial patterns and their implications for local development.

Table 3: Data collected - National Institute of Statistics and Census (INEC)

Type of Information	Data Purpose	Data Format	Analysis Tools Used
Demographic, economic and population density data	The socioeconomic distribution in Quevedo	Structured databases in Excel,	Excel
census cartography for the years 2010 and 2020	Correlate urban growth with population density	Shapefiles at 1:25000 scale	ArcGIS

Source: National Institute of Statistics and Census (INEC, 2024)

Ministry of Agriculture and Livestock (MAG)

The data collected on the type and capacity of land use helped to delimit areas specifically designated for agriculture, distributed in five (3) categories: Forestry, Agriculture, Livestock, thus protecting lands of agricultural value from uncontrolled urban expansion and additionally, 2 essential categories were determined for the process of determining expansion, such as: Consolidated urban areas and Double River.

Table 4: Data collected - Ministry of Agriculture and Livestock (MAG)

Type of Information	Data Purpose	Data Format	Analysis Tools Used
Land use capacity, agricultural areas and classification	Protect areas of agricultural value from urban growth and ensure agricultural sustainability	Soil classification shapefiles, maps	QGIS

Source: Ministry of Agriculture and Livestock (MAG).

Semi-structured interviews were then conducted with municipal officials, urban development experts, community leaders, and cantonal authorities to obtain detailed, firsthand information on the policies, practices, and challenges related to urban development in Quevedo. These interviews were carefully recorded and subsequently analyzed to identify relevant patterns and themes.

Finally, field visits were conducted to directly observe the urban environment in different areas of Quevedo, gathering qualitative information on infrastructure, land use, and the quality of the urban environment. Detailed observations will be recorded to complement the data obtained through surveys and interviews. These activities will be carried out in a coordinated manner, following ethical protocols and utilizing appropriate sampling techniques to ensure the validity and reliability of the data collected.

Once the data was collected, it was systematically and securely organized. It was then analyzed using appropriate techniques, such as statistical analysis. This process allowed for the data to be examined

and the results to be interpreted in relation to the research objectives and questions posed. Significant patterns, trends, relationships, or findings that emerged from the data were then identified. These findings were related to the existing literature to conduct a discussion relevant to each of the specific research objectives.

2.5 Data processing and analysis.

The processing and analysis of the collected information was carried out through a combination of manual and automated methods, using specialized software when necessary. First, data was coded by assigning numerical codes or categories to the survey and interview responses. The data were then entered into spreadsheets or databases, ensuring their accuracy and completeness. Extensive data cleaning was performed to identify and correct any errors or inconsistencies, ensuring data quality for analysis.

Regarding data analysis, different techniques were applied depending on the nature of the information collected. Descriptive statistical analyses were performed to summarize and present the data in a clear and understandable manner, using tables, graphs, and measures of central tendency and dispersion. In addition, a qualitative analysis of the open-ended responses from the surveys and interviews was conducted, identifying patterns, themes, and emerging trends.

For the spatial analysis of data related to urban expansion, geospatial analysis tools such as population density maps, land use, and service distribution were used. Relevance, consistency, and interpretation criteria were applied during data analysis, ensuring that the results were relevant to answering the research questions and objectives of the study.

The software used for data analysis included tools such as Microsoft Excel and a combination of GIS (Geographic Information Systems) software such as IDIRIS, using the Lean Chain Modeler module for Markov Chain analysis. ArcGIS and QGIS were also used, depending on the specific needs of each statistical and spatial analysis. These tools enabled a comprehensive and rigorous analysis of the collected data, providing valuable information for research on the urban expansion of Quevedo and its impact on local development.

III. RESULTS

3.1 Urban growth history using geospatial and temporal data to identify significant areas of expansion in the Quevedo canton.

The collection and analysis of geospatial data from the Municipality of Quevedo identified key points for planning a potential urban expansion. Using strategic information, sectors with high growth potential were delimited by integrating urban zoning, land use, and orthophotography into a Geographic Information System (GIS). Processing shapefiles and vector maps at a scale of 1:1000 in ArcGIS and QGIS facilitated the assessment of territorial evolution and its compliance with current regulations. The results revealed clear growth patterns in urban and peri-urban areas, highlighting strategic sectors for expansion. The precision provided by orthophotography allowed for more precise delimitation of these areas, consolidating an essential database for territorial planning and the sustainable management of urban growth in the Quevedo canton (Fig. 3).

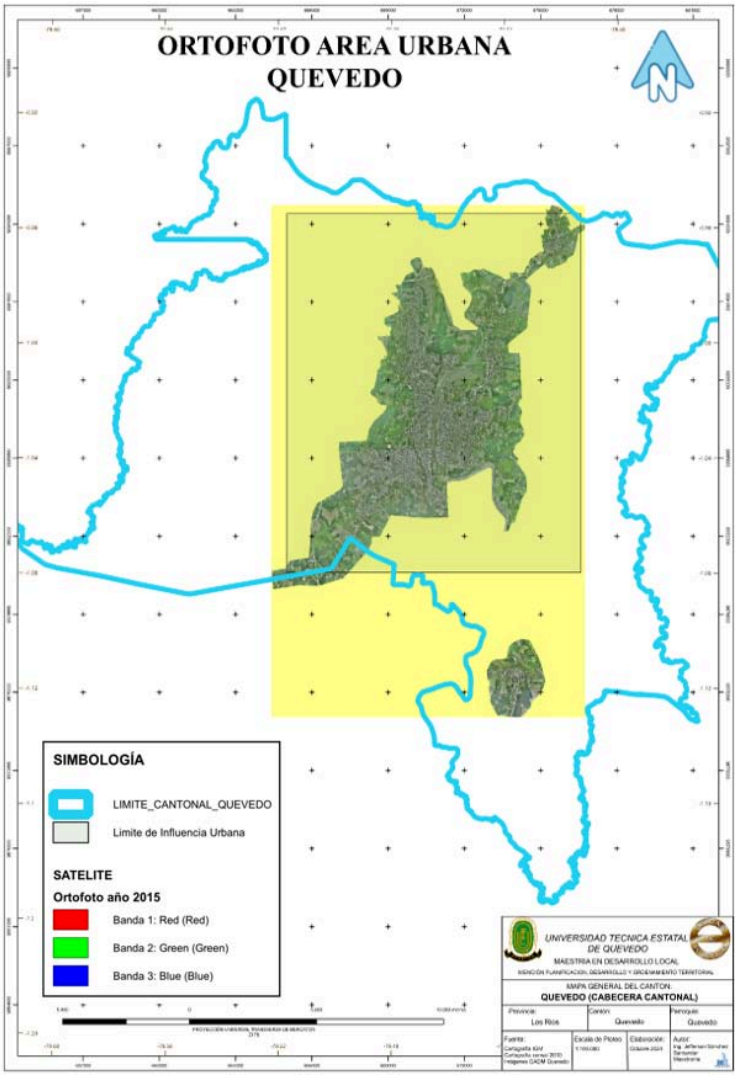

Figure 3: Orthophoto of the Quevedo canton.

The data provided by the IGM, which include base cartography and geospatial data with detailed information on topography and land use at a scale of 1:25,000 for the 2010 and 2020 periods, established a solid geographic basis for assessing urban growth. From this analysis, areas with significant land-use changes and high potential for urban expansion were identified. Additionally, a spatial analysis was conducted to exclude areas of high agricultural value and protected areas, ensuring that urban growth projections are compatible with the principles of territorial sustainability. A base map was generated delimiting viable areas for urban expansion, considering the canton's topography and its interaction with urban growth dynamics. This information represents a key tool for territorial planning and strategic decision-making, facilitating orderly and sustainable urban development in Quevedo (Fig. 4).

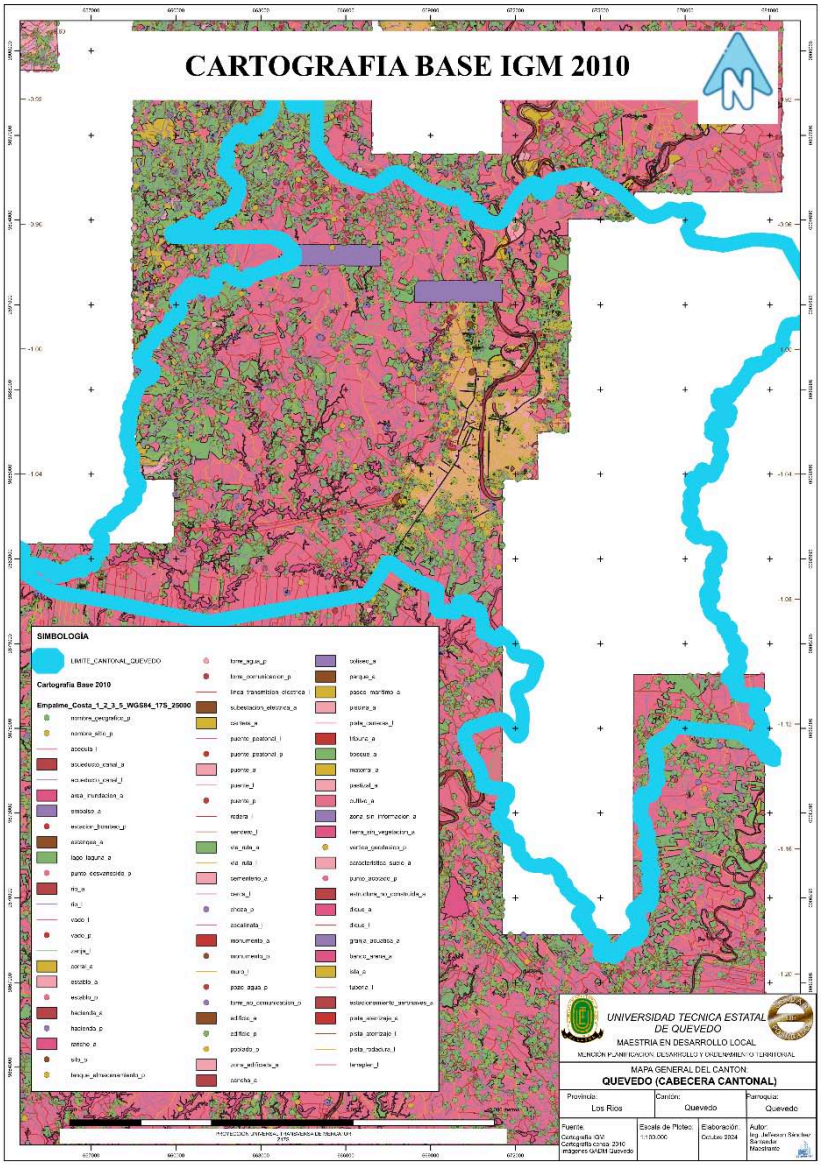

Figure 4: Quevedo *base cartography 2010-2020.*

Data obtained from the National Institute of Statistics and Census (INEC) for the years 2010 and 2020 allowed for the correlation of territorial expansion with key variables such as population density, settlement growth, and service demand. The integration of census data into population density maps, processed in Excel and ArcGIS, revealed significant changes in the canton's demographic distribution. Areas of accelerated growth were identified, allowing for an assessment of the impact of urbanization on the territory's socioeconomic structure. Despite the delay in the 2020 Census, the 2019-2020 base cartography was a key input for projecting expansion trends. As a result, comparative maps were generated highlighting the areas with the greatest urban growth and their relationship with population distribution, providing essential information for territorial planning and the sustainable management of urban development in Quevedo (Fig. 5).

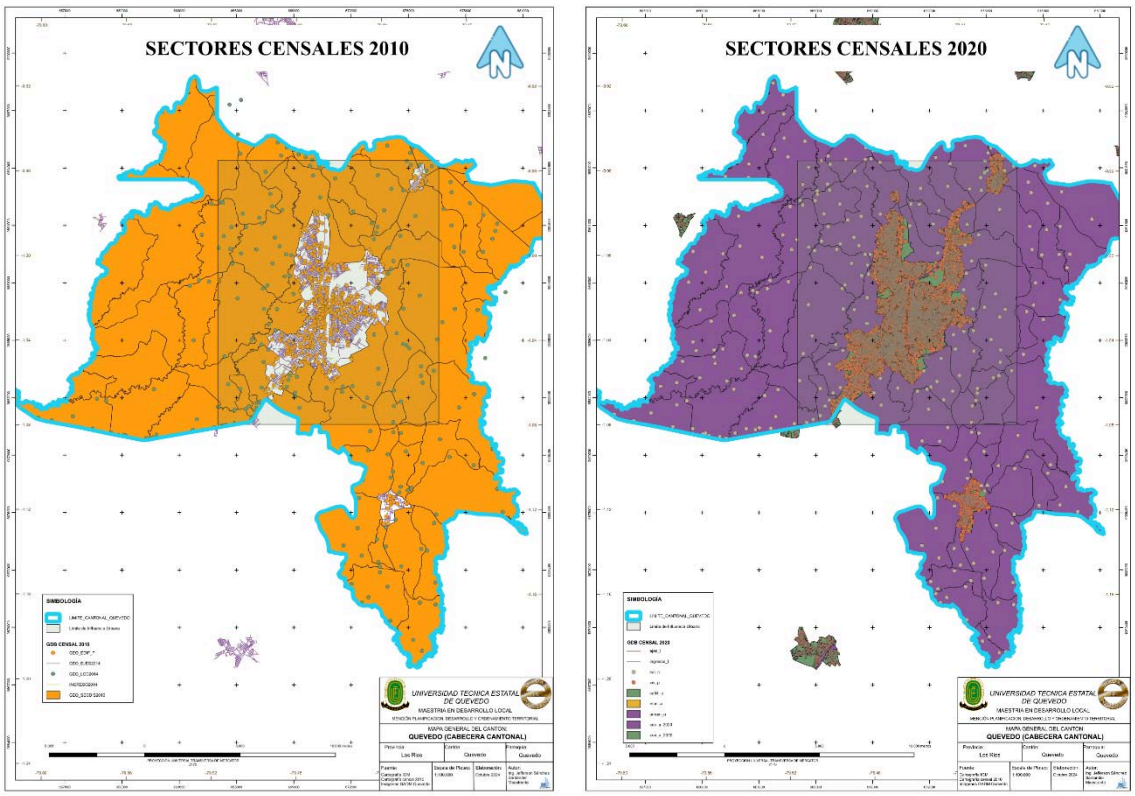

Figure 5: Census sectors of the Quevedo canton: (a) 2010 census period; (b) 2020 census period.

Analysis of information provided by the Ministry of Agriculture and Livestock (MAG) enabled the establishment of a precise land classification in the Quevedo canton for the 2010 and 2020 periods, differentiating between five key categories: forestry, agricultural, livestock, consolidated urban areas, and double rivers. This segmentation was essential for delimiting areas of high agricultural value and identifying zones with potential for urban expansion. By processing soil classification shapefiles and maps in QGIS, data was cross-referenced with urban growth zones, allowing for the identification of priority areas for agricultural conservation and the avoidance of unplanned urbanization of productive lands. A land use capacity map was generated, providing a key tool for the sustainable management of urban growth, ensuring a balance between territorial expansion and the protection of agricultural resources. This information is essential for strategic decision-making in Quevedo's territorial and urban planning (Fig. 6).

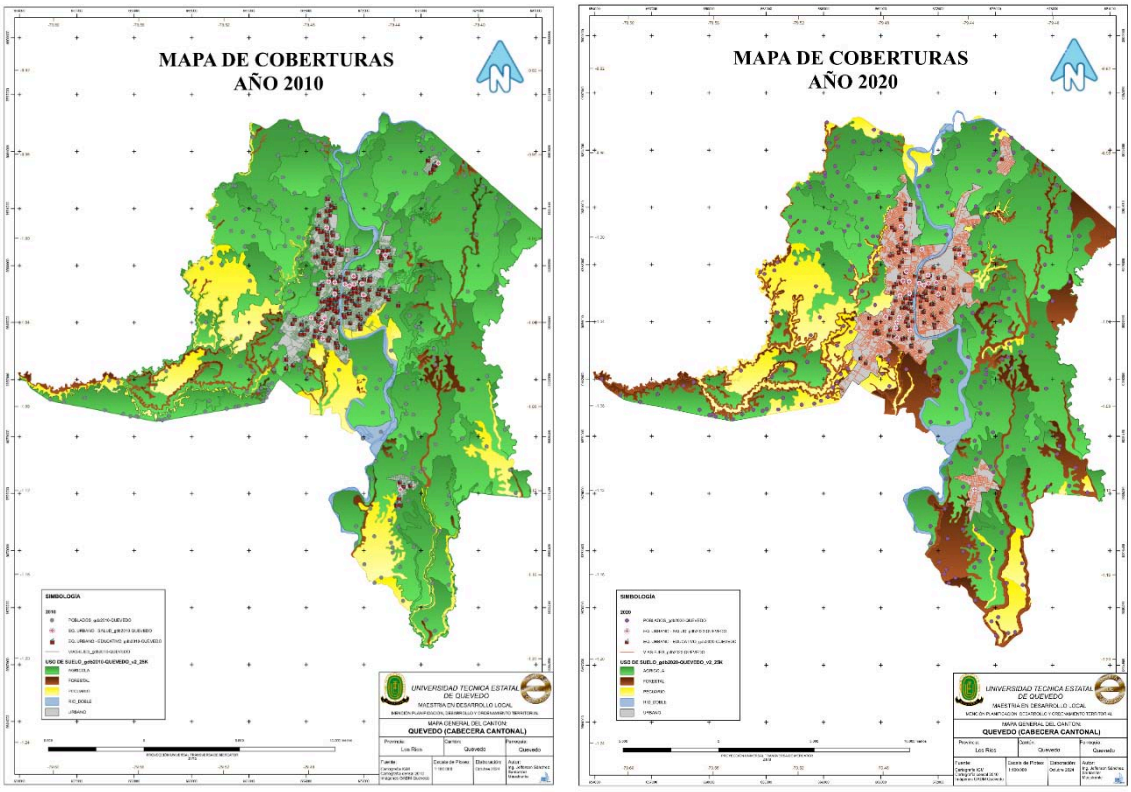

(a) (b)

Figure 6: Land-use cover maps for Quevedo canton: (a) 2010 land cover layer; (b) 2020 land cover layer.

3.2 Urban expansion scenarios using geospatial modeling techniques in Quevedo with a 2030 vision

The results obtained from the urban expansion scenario modeling process in Quevedo offer a detailed and phased projection of land use changes over 20-year intervals, visualizing projected urban growth for the years 2030 as an initial resulting basis for the scope of the research, and additionally generating projections for the years 2050, 2070 and 2090.

The implementation of the Markov chain in the IDRISI Land Change Modeler enabled a robust simulation based on the observed transitions between the 2010 and 2020 stages, identifying areas with a high probability of conversion to urban uses and reflecting the influence of factors such as land use, proximity to roads and proximity to towns (Fig. 7).

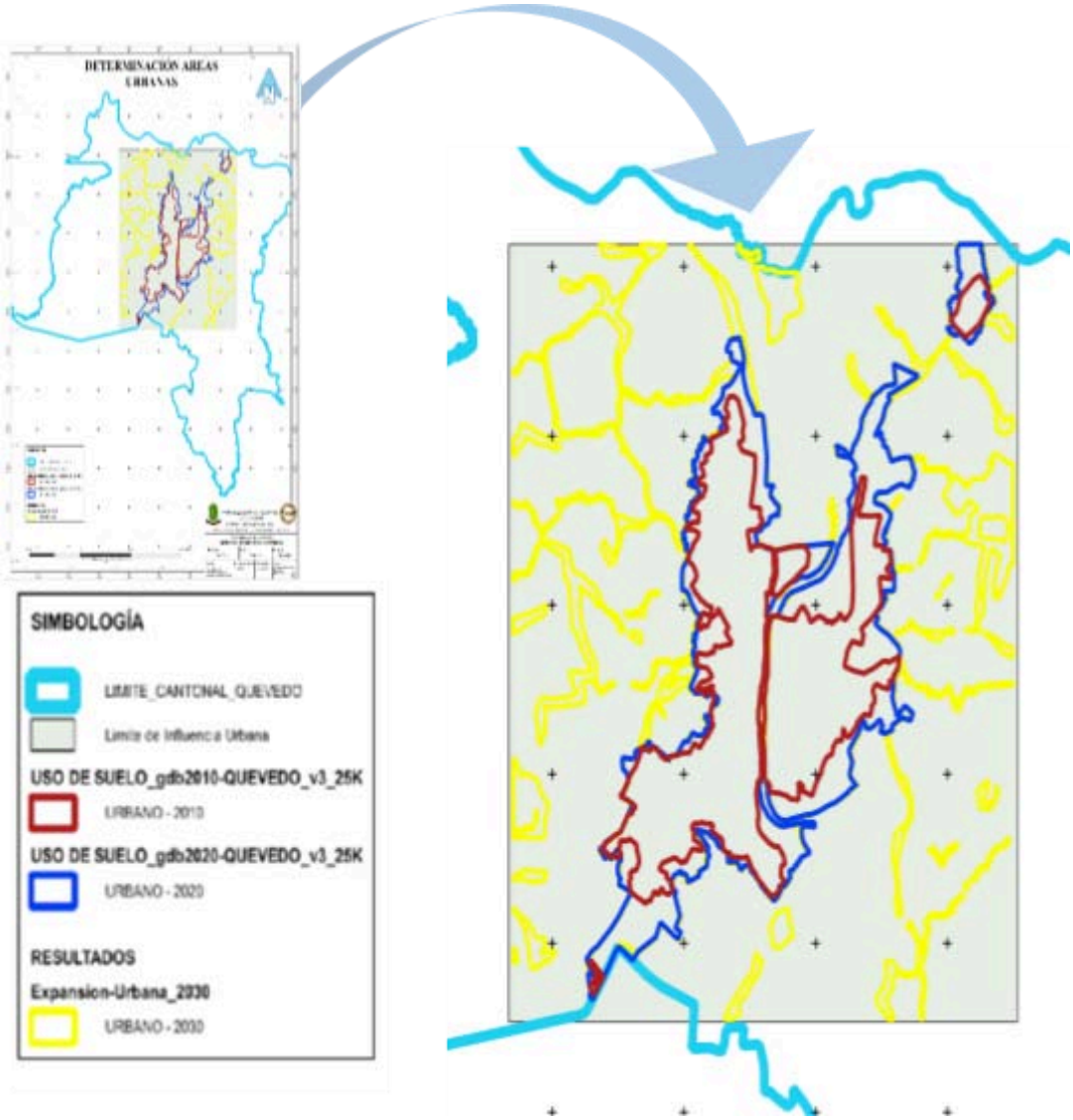

Figure 7: Comparison of Quevedo's urban expansion projection, year 2030.

The scenario for 2030 projects an urban growth of 1,104 hectares, corresponding to a 32% increase compared to the 2020 stage, concentrated in areas with high accessibility, particularly in sectors such as El Guayabo, La Victoria, El Pital, Recinto El Minón, Recinto La Estrella, La Estrella (Las Palmas sector), Santa Rita, Virginia N°2, These sectors coincide with being in areas close to the main communication routes and towns, especially on lands whose activities were previously destined for agriculture and livestock. Based on the prediction established in the model, significant pressure on these productive lands is shown, which poses challenges for territorial planning and natural resource management (Fig. 8).

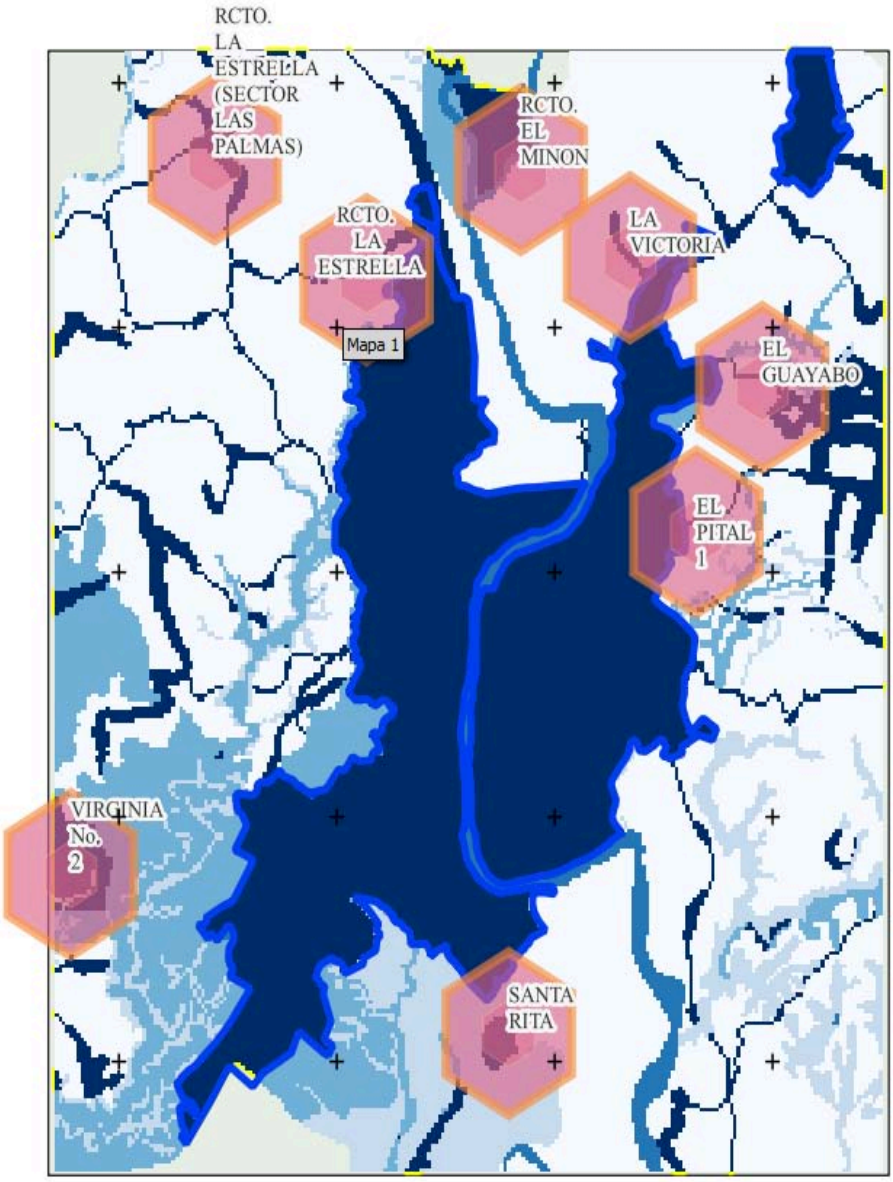

Figure 8: Modeling of Quevedo's urban expansion projection for the 2030 scenario.

The scenario for the year 2050 shows an expansion that includes forest lands and areas further away from population centers. This pattern reflects a growing pressure on lands that were previously not urban, such as those located in the southern part of Recinto la Virginia #2, El Bosque sector, Tropifrutas, Recinto la Estrella, La Victoria Norte, Faita, reaching an urban land occupation of 6,286.2 hectares, which is an increase of 81% compared to the 2020 stage, implying a possible significant transformation of natural areas. Considering maintaining correct control over the expansion areas, it is extremely important to apply conservation measures and territorial planning policies that can effectively manage this advance, in order to minimize the environmental impact and preserve (Fig. 9).

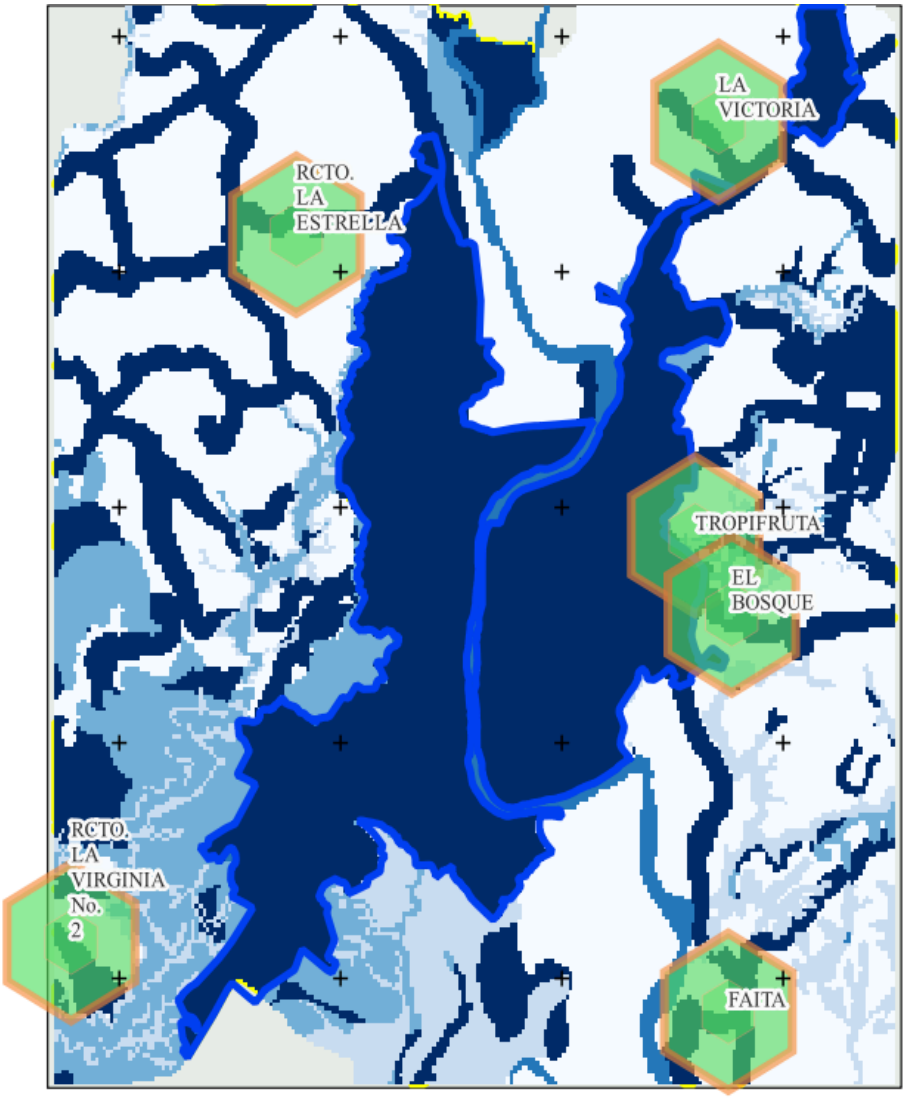

Figure 9: Modeling of Quevedo's urban expansion projection for the 2050 scenario.

The scenario for the year 2070 shows a projection with considerable advances in peripheral and less accessible areas, indicating a dispersed growth that could generate challenges in access to basic services, such as drinking water, electricity, health and education, especially in more remote areas such as Recinto El Tropezón, Hacienda María Isabel, Colonia Villa Franca, Recinto San Vicente, Hacienda Agua Blanca, which is reflected in a total increase of 116% in occupation of the urban area in relation to the 2020 stadium, reaching a total of 7,527.3 hectares of occupation of urban land in Quevedo (Fig. 10).

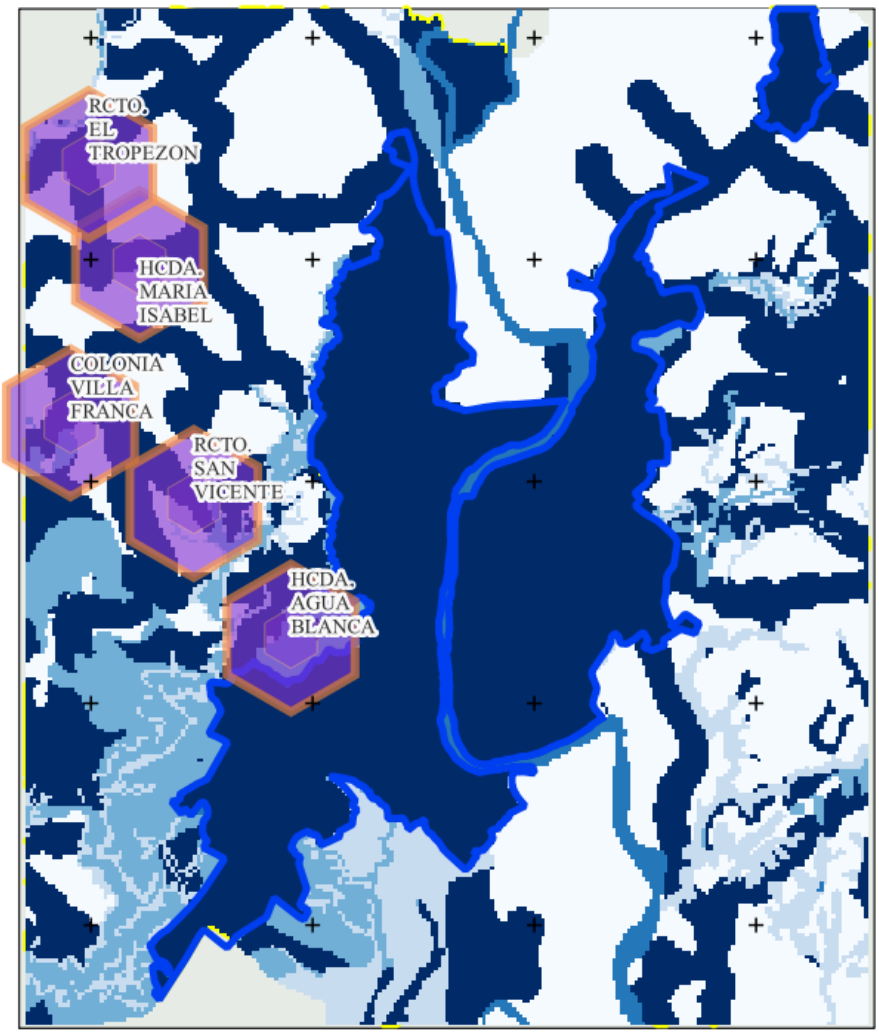

Figure 10: Modeling of Quevedo's urban expansion projection for the 2070 scenario.

The 2090 scenario shows a final projection with substantial urban growth reaching 8,494.6 hectares, with urbanized areas occupying a significant portion of the lands originally designated for agricultural and livestock activities, marking a consolidation in the sectors established in the 2030, 2050 and 2070 scenarios and additionally expanding urban expansion in sectors such as Cañalito, Nueva Esperanza sector, Ana María Sector, Recinto El Barro, Hacienda San Juan. This scenario suggests a considerable impact on the availability of land for agricultural uses, which could affect food production and the economic sustenance of rural communities (Fig. 11).

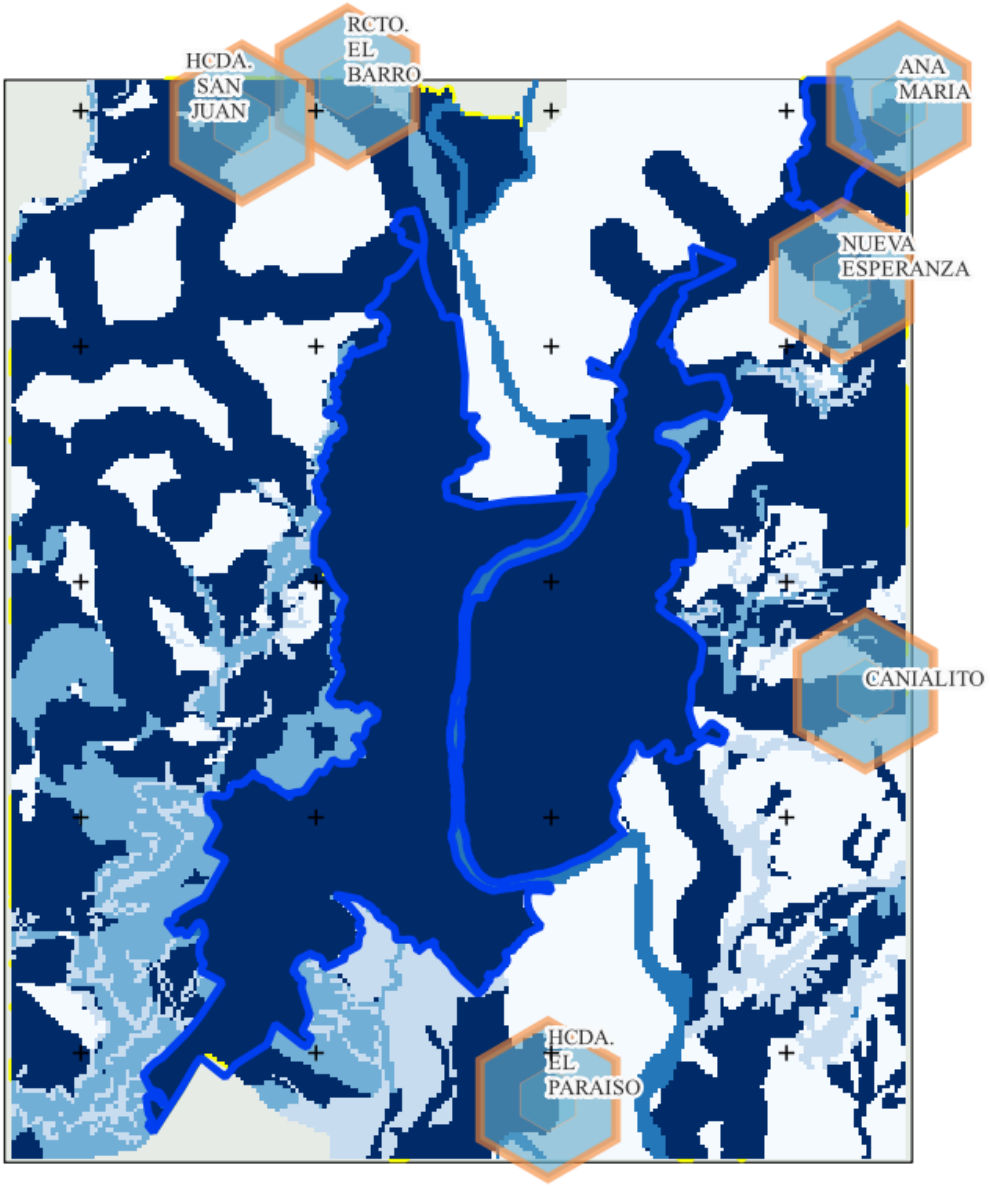

Figure 11: Modeling of Quevedo's urban expansion projection for the 2090 scenario.

3.3 Urban expansion scenarios influence access to basic services, security, and economic activity in the Quevedo canton.

The polygons marked in dark tones within the expansion zones suggest areas with a high density of projected growth. These areas are aligned with road and access infrastructure that connect directly to the urban core of Quevedo, facilitating access and, therefore, increasing their attractiveness for residential and commercial development. The proximity of these sectors to main transportation routes is a determining factor in their selection for expansion, as it facilitates the mobility of residents and enhances access to basic goods and services (Fig. 12).

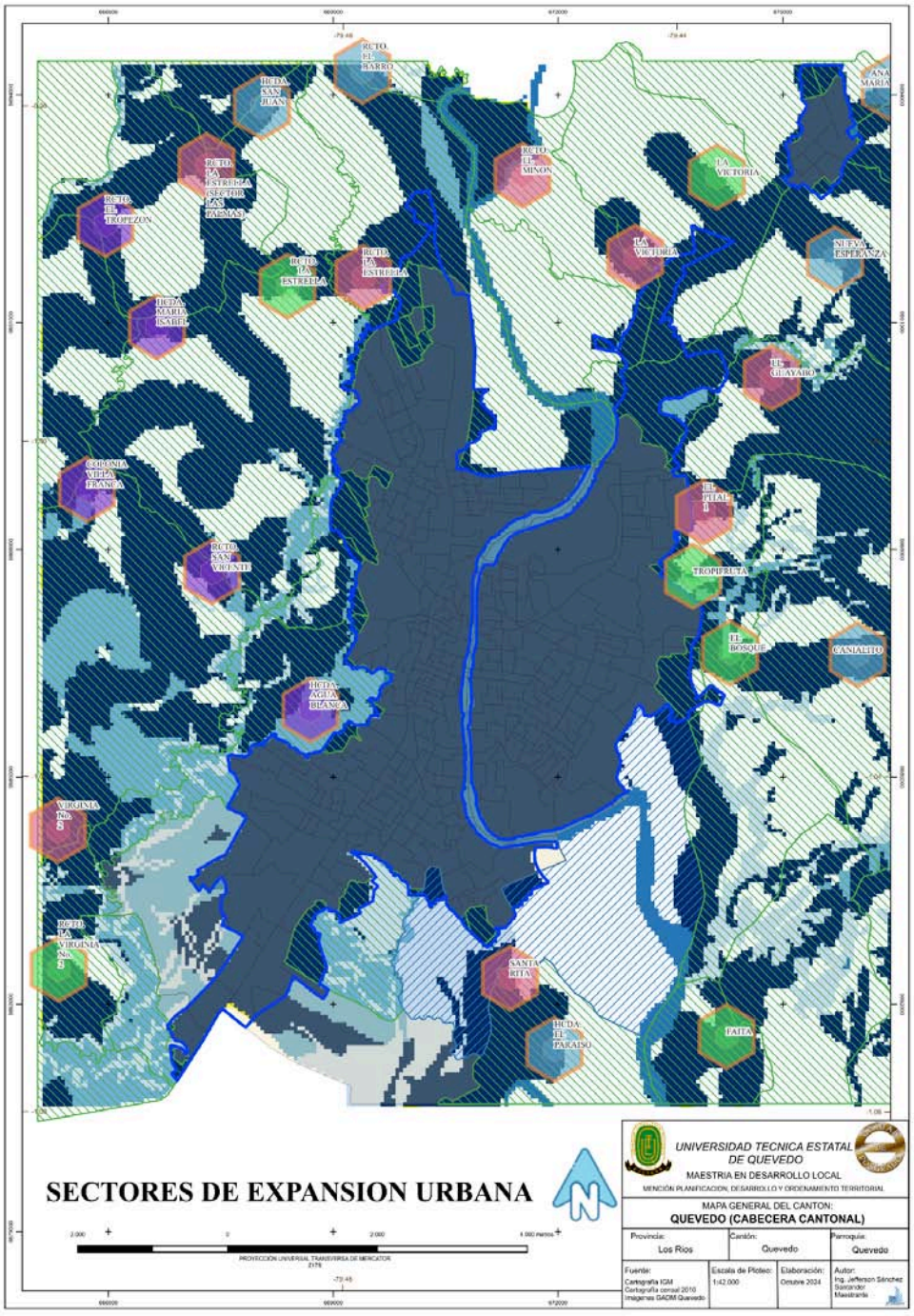

Figure 12: Identification of sectors with projections for urban expansion 2030-2090.

Based on the analysis of data obtained from the urban expansion scenario modeling process and looking toward 2030, the areas of the Quevedo canton with a high projection of urban expansion are revealed, highlighting strategic sectors located mainly on the outskirts of the consolidated urban area. These sectors, with greater predominance located in the northern part of the city, include areas identified as: El Guayabo, El Bosque, Tropifruta, La Victoria, Nueva Esperanza, Recinto El Minón, La Estrella (Las Palmas sector), and a slight projection in the south and southwest where the sectors known as Hacienda Agua Blanca, Santa Rita, Virginia N°2, Faita, among others, are located. The concentration of areas prone to expansion in these sectors suggests a tendency for urban growth to shift towards peripheral areas, which coincides with the need for infrastructure and basic services development in these areas.

Within the geospatial analysis, a combination of urbanizable zones and rural areas, especially those used for agriculture and forestry, also stands out, suggesting potential land-use conflicts between urban expansion and the preservation of agricultural land. This projected expansion presents challenges in terms of balancing urbanization and the protection of natural resources. Therefore, it is crucial to establish planning policies that ensure the sustainable development of these areas, avoiding the loss of productive land.

IV. DISCUSSION

The analysis of urban growth in Quevedo, supported by an exhaustive collection and review of data from the various sources investigated, ensured the reliability and accuracy of the results obtained. The integration of information from key institutions, such as the Military Geographic Institute (IGM), the National Institute of Statistics and Census (INEC), the Ministry of Agriculture and Livestock (MAG), and the municipality of Quevedo, established a solid foundation of geospatial and socioeconomic data. These data covered critical aspects for modeling urban expansion scenarios in the city of Quevedo, such as land use, infrastructure for services and basic facilities, and demographic patterns, allowing for a comprehensive view of urban expansion in the canton.

IGM mapping and INEC census data provide precision in land-use classification and delimitation, while MAG data contribute to understanding areas of agricultural value that could be affected by urban expansion (Ulloa and Martín, 2024) . Specifically, MAG data reflected significant changes in land categories between 2010 and 2020.

The agricultural area experienced a 24.1% reduction, going from 17,683.4 hectares in 2010 to 13,442.3 hectares in 2020, while the urban area increased by 56.4%, from 2,226.9 hectares to 3,482.4 hectares over the same period. Likewise, an increase in the forest area was observed, which went from 800.0 hectares in 2010 to 2,005.5 hectares in 2020, suggesting reforestation efforts or changes in land use. Similarly, livestock use showed growth from 2,444.8 hectares to 3,022.2 hectares, while the water body category (double river) increased from 806.5 hectares to 1,306.2 hectares.

These changes reflect a transformation in land use that, while responding to the dynamics of urban expansion and population growth, also poses challenges in terms of territorial planning and sustainability (Salazar et al., 2020) . The reduction in agricultural land and the increase in urban land indicate growing pressure on productive resources, underscoring the importance of territorial planning strategies that seek a balance between urban development and the conservation of strategic land for agricultural, livestock, and forestry production.

The application of the Markov chain (CA-Markov) in IDRISI software, as mentioned (Viana et al., 2022), is one of the most effective methods for modeling stochastic and probabilistic evolution processes, especially when the only available information is the current state of the system. This application, combined with data preprocessing in ArcGIS, allowed the development of a robust and detailed projection of urban expansion in Quevedo from 2030 to 2090. The modeling results clearly show how factors such as land use type, proximity to main communication routes, and proximity to population centers are key determinants of the direction and pace of future urbanization.

Considering the prospective urban expansion scenarios for Quevedo, it can be seen that without an adequate land use and management plan, urban growth could jeopardize highly valuable agricultural areas, affecting both the economic and territorial sustainability of the canton. This situation is worrying, since studies carried out in Ecuador have shown that uncontrolled urban expansion and the consequent loss of agricultural land negatively affect the environmental balance as well as food security and the local economy, a problem already observed in other cities with similar growth patterns, as

indicated by (Ortiz, 2023) . The projection to the year 2090 also points to the danger of dispersed urban development, which could lead to disconnected areas with limited access to basic services, increasing territorial and social inequalities in the region.

The generation of urban expansion scenarios in the Quevedo canton suggests a series of significant impacts on various aspects of the canton's urban environment, including access to basic services, security, and economic activity in the areas with the greatest growth projections. This third outcome focuses on understanding how projected urban growth will influence these three fundamental aspects, considering both quantitative data derived from geospatial modeling and the opinions of key stakeholders interviewed, including municipal officials and neighborhood leaders.

Urban expansion into peri-urban areas poses a significant challenge in terms of service management. The areas with the greatest potential for expansion, such as the neighborhoods of El Guayabo, La Estrella, and Santa Rita, currently face limitations in drinking water, sewage, and electricity infrastructure. The Director of Planning for the Municipal GAD stated that proximity to access roads and the availability of infrastructure significantly influence zoning decisions and investment prioritization in these areas. However, he mentioned that rapid and significant expansion could exceed existing capacity, which would put greater pressure on municipal resources to improve or expand these services in these areas.

Previous studies have shown that in similar situations, considering the conversion of land to urban uses without adequate planning, it has complicated the delivery of basic services, such as drinking water, electricity, and waste management, particularly in areas with rapid population growth. According to Salazar et al., 2021, (Salazar et al., 2020).

Urban sprawl could also increase the risks of insecurity in areas with low connectivity and limited police presence (Cabrera et al., 2020) . Expansion into peri-urban areas complicates the work of police surveillance, which, according to the councilor, taking his words, expansion into rural areas often increases the risk of crime by making constant surveillance difficult (Cabrera-Barona et al., 2020) . This phenomenon is supported by studies that indicate that rapid urban growth has been linked to an increase in security problems, particularly in areas of informal settlements that lack appropriate infrastructure. This problem is generating a greater perception of insecurity among residents of the sector and the community in general (Bonilla et al., 2020). (Ortiz, 2023).

Economic activity, in general terms, anticipates that urban growth or expansion could expand opportunities for developing businesses and services and generating employment for the local population. However, residents of areas like El Guayabo maintain that the local economy still faces significant limitations. While the arrival of new residents has favored the establishment of small businesses, such as neighborhood stores, real economic growth in the community requires stronger support from municipal and government authorities. This requires public investment in infrastructure and policies that promote the formalization and diversification of stable jobs, capable of guaranteeing solid and recurring income for families, thus incentivizing local consumption.

The research of (Donoso & Sarmiento, 2020) (Ortega and Pino, 2021) supports this idea, demonstrating that an urban expansion process where effective territorial planning is implemented attracts investment and promotes local employment, especially in activities such as commerce and construction, which becomes a boost for the local economy, while a disorderly expansion without planning by the competent authorities tends to slow down development due to the lack of adequate services and incentives for companies.

V. CONCLUSIONS

The analysis of urban growth in Quevedo between 2010 and 2020 revealed a significant transformation in land use, with a reduction in agricultural areas from 17,683.4 to 13,442.3 hectares and an increase in urban areas from 2,226.9 to 3,482.4 hectares, reflecting sustained expansion. The integration of geospatial and temporal data from official sources allowed for precise mapping of these dynamics, correlating them with demographic factors, infrastructure, and territorial regulations. The use of GIS tools enabled a detailed comparative analysis, identifying key spatial patterns for territorial planning.

Geospatial modeling of urban expansion scenarios in Quevedo with a 2030 vision allowed for the accurate projection of territorial growth and its future implications. The implementation of the Markov Chain-based methodology and the use of IDRISI software made it possible to identify sectors with a high probability of conversion to urban land, such as El Guayabo, El Pital 1, La Victoria, Recinto El Minón, Recinto La Estrella, Recinto La Estrella (Las Palmas Sector), Santa Rita, Virginia No. 2, El Bosque, Faita, La Victoria, Tropifruta, Colonia Villa Franca, Hacienda Agua Blanca, Hacienda María Isabel, Recinto El Tropezón, Recinto San Vicente, Ana María, Cañalito, Hacienda El Paraíso, Hacienda San Juan, Nueva Esperanza, and Recinto El Barro, considering key factors such as land use, proximity to roads, and population centers. The results showed sustained urban growth, projecting a 32% increase in 2030 and reaching 144% by 2090, with a significant impact on the reduction of agricultural and livestock areas. Uncontrolled expansion could generate land-use conflicts and challenges in the provision of basic services, requiring land-use planning strategies that balance urbanization with environmental and productive sustainability.

The analysis of urban expansion in Quevedo demonstrated its significant impact on access to basic services such as drinking water, sewage treatment, electricity, and public transportation, as well as access to educational institutions, health sub-centers, security, and economic activity. The identification of sectors with high growth projections, such as El Guayabo, El Pital 1, Faita, La Estrella, Santa Rita, and La Virginia, revealed that rapid urbanization generates a growing demand for essential infrastructure, which can exceed municipal capacity if not properly planned. Furthermore, it was determined that expansion into peri-urban areas such as the Tropifruta sector, Colonia Villa Franca, Hacienda Agua Blanca, Hacienda María Isabel, Recinto El Tropezón, Recinto San Vicente, Ana María, Cañalito, Hacienda El Paraíso, Hacienda San Juan, Nueva Esperanza, and Recinto El Barro, presents security risks due to poor connectivity and limited surveillance coverage, highlighting the need for integrated land use and control strategies. In the economic sphere, while urban growth has boosted trade and job creation in specific sectors, the lack of infrastructure and strategic planning limits its sustainable development.

REFERENCES

1. Alvarado, R., & Jiménez, C. (2020). The relationship between competitiveness and regional development in Ecuador: An application of spatial models. *Journal of Economics and Politics*, *3* , 117–133. https://doi.org/10.25097/rep.n31.2020.06
2. Barragán, F. (2022). Spatial network analysis for the study of internal migration: an application to the Ecuadorian case. *Documents d'anàlisi Geogràfica*, *68* (2), 335–361. https://doi.org/10.5565/rev/dag.696
3. Bonilla, S., Mora, A., Vaca, A., Estrella, A., & Herrera, M. Á. (2020). Modeling the relationship between urban expansion processes and urban forest characteristics: An application to the Metropolitan District of Quito. *Computers, Environment and Urban Systems*, *79*, 101420.
4. Cabrera-Barona, PF, Bayón, M., Durán, G., Bonilla, A., & Mejía, V. (2020). Generating and mapping Amazonian urban regions using a geospatial approach. *ISPRS International Journal of Geo-Information*, *9* (7), 453.

5. Cabrera, PF, Bayón, M., Durán, G., Bonilla, A., & Mejía, V. (2020). Generating and mapping Amazonian urban regions using a geospatial approach. *ISPRS International Journal of Geo-Information*, *9* (7), 453. https://doi.org/10.3390/ijgi9070453
6. Cahe, E.J., & de Prada, J.D. (2024). Territorial planning: A strategic vision of the rural urban fringe in Adelia María, Córdoba. *RIVAR (Santiago)*, *11* (32), 42–59. https://doi.org/10.35588/rivar.v11i32.6144
7. Cardoso, M. M., & Carñel, G. E. (2022). Urban planning: A multi-criteria assessment for new locations for health centers in Santa Fe. *Cuadernos de Vivienda y Urbanismo*, *13* (25), 1–25. https://doi.org/10.11144/Javeriana.cvu15.puem
8. Coello, KPB, León, CC, & Coello, GB (2024). Evaluation of environmental quality in the city of Quevedo: the significant role of the San Camilo parish in sustainable development. *South Center*, *8* (1). https://doi.org/10.37955/cs.v8i1.341
9. Crissi, V. (2021). A conceptual model for addressing territorial planning. *Economy, Society and Territory* , *21* (67), 865–892. https://doi.org/10.22136/est20211721
10. Domingo, D., Palka, G., & Hersperger, AM (2021). Effect of zoning plans on urban land-use change: A multi-scenario simulation for supporting sustainable urban growth. *Sustainable Cities and Society* , *69* , 102833. https://doi.org/10.1016/j.scs.2021.102833
11. Donoso, ME, & Sarmiento, FO (2020). Sustainable urbanism or amenity migration fad: Critical analysis of urban planning of Cuenca cityscapes, Ecuador. In *The Elgar Companion to Geography, Transdisciplinarity and Sustainability* (pp. 252–268). Edward Elgar Publishing.
12. Du, P., Bai, X., Tan, K., Xue, Z., Samat, A., Xia, J., Li, E., Su, H., & Liu, W. (2020). Advances of four machine learning methods for spatial data handling: A review. *Journal of Geovisualization and Spatial Analysis* , *4* , 1–25. https://doi.org/10.1007/s41651-020-00048-5
13. Duque, I. (2021). Smart cities in the planning and urban governance agenda in Latin America. *Cuadernos de Geografía: Colombian Journal of Geography*, *30* (2), 280–296. https://doi.org/10.15446/rcdg.v30n2.89479
14. Duque, I., & Montoya, J.W. (2021). Climate change and urbanization. *Colombian Journal of Geography* , *30* (2), 274–279.
15. Duranton, G., & Puga, D. (2023). Urban growth and its aggregate implications. *Econometrica* , *91* (6), 2219–2259. https://doi.org/10.3982/ECTA17936
16. Fernandez, FE (2020). Territorial planning with multi-criteria evaluation. *RevIISE-Journal of Social and Human Sciences* , *18* (18), 47–71.
17. García, JRR, Inga, CV, Huertas, FDA, Medina, RAU, Rivadeneira, ROA, & Rodríguez, MAM (2023). *Education and Society in Latin American Culture* . OSF. https://doi.org/10.31219/osf.io/2yzpk
18. Giorguli, SE, García, VM, & Masferrer, C. (2022). Demographic Environment and Migration Perspectives in Latin America and the Caribbean. In *The Routledge History of Modern Latin American Migration* (pp. 277–293). Routledge.
19. Gold, C. M. (2020). Surface interpolation, spatial adjacency and GIS. In *Three dimensional applications in GIS* (pp. 21–35). CRC Press.
20. Guerrero, PEO (2022). The urbanization process in 20th-century Ecuador. *ACORDES* , 89–104.
21. Hendricks, M.D., & Van Zandt, S. (2021). Unequal protection revisited: Planning for environmental justice, hazard vulnerability, and critical infrastructure in communities of color. *Environmental Justice*, *14* (2), 87–97. https://doi.org/10.1089/env.2020.0054
22. Koldasbayeva, D., Tregubova, P., Gasanov, M., Zaytsev, A., Petrovskaia, A., & Burnaev, E. (2024). Challenges in data-driven geospatial modeling for environmental research and practice. *Nature Communications* , *15* (1), 10700. https://doi.org/10.1038/s41467-024-55240-8
23. Koprowska, K., Łaszkiewicz, E., & Kronenberg, J. (2020). Is urban sprawl linked to green space availability? *Ecological Indicators* , *108* , 105723. https://doi.org/10.1016/j.ecolind.2019.105723

24. Li, W., Batty, M., & Goodchild, M.F. (2020). Real-time GIS for smart cities. In *International Journal of Geographical Information Science* (Vol. 34, Issue 2, pp. 311–324). Taylor & Francis. https://doi.org/10.1080/13658816.2019.1673397
25. Long, H., Zhang, Y., Ma, L., & Tu, S. (2021). Land use transitions: Progress, challenges and prospects. *Land* , *10* (9), 903. https://doi.org/10.3390/land10090903
26. López, F. (2023). Evolution of urban growth and the territorial model on the coast of the southeastern Spanish peninsula. *Revista de Geografía Norte Grande*, *84*, 293–321. https://doi.org/10.4067/S0718-34022023000100293
27. Lytvynchuk, I., Skydan, O., & Ivaniuk, O. (2020). Local governance and territorial development on the basis of GIS. *Management Theory and Studies for Rural Business and Infrastructure Development* , *42* (4), 422–433. https://doi.org/10.15544/mts.2020.43
28. Maeso, RPH, & Hidalgo, EC (2020). Emerging challenges in the distribution of urban and rural population in the world: A global and European overview of urban growth. *História e Economia*, *24* (1), 21–37.
29. Mamonov, K., Sklyar, I., Pilicheva, M., Kasyanov, V., & Shyshkin, E. (2021). A model for assessing the regional land-use territorial development. *Geodesy and Cartography*, *70* (2).
30. Mejía, A.J., Fuentes, N.M., & Chávez, M.R. (2024). Challenges and opportunities in the provision of drinking water services by the Decentralized Autonomous Government of the Quevedo Canton. *Scientific Code Research Journal* , *5* (E4), 56–76. https://doi.org/10.55813/gaea/ccri/v5/nE4/461
31. Mena, CF, Benitez, FL, Sampedro, C., Martinez, P., Quispe, A., & Laituri, M. (2022). Modeling urban growth and the impacts of climate change: the case of Esmeraldas City, Ecuador. *Sustainability* , *14* (8), 4704. https://doi.org/10.3390/su14084704
32. Ortega, K.M., & Pino, S.L. (2021). Social and economic impact of risk factors affecting citizen security in Ecuador. *Espacios Magazine*, *42* (21). https://doi.org/10.48082/espacios-a21v42n21p04
33. Ortiz, RP (2023). *Characterization of Peri-Urban Territories: Patterns and Dynamics: The Case of the Metropolitan District of Quito, Ecuador* . University of Liege (Belgium).
34. Otero, A., & Llop, J.M. (2020). The Intermediate City: Growth and Development Dynamics. *Territories*, *43SPE* , 1–8.
35. Roldan, AL, Arellano, LM, Arteaga, EZ, Carpio, WM, & Argudo, FM (2024). Economic analysis of population growth and its influence on Ecuadorian socioeconomic development: an econometric approach. LATAM *Latin American Journal of Social Sciences and Humanities*, *5* (5), 1286–1306. https://doi.org/10.56712/latam.v5i5.2687
36. Sadooghi, S.E., Taleai, M., & Abolhasani, S. (2022). Simulation of urban growth scenarios using integration of multi-criteria analysis and game theory. *Land Use Policy*, *120*, 106267. https://doi.org/10.1016/j.landusepol.2022.106267
37. Sagastume, D., Gibert, J.M.R., Briones, C.S., & Banda, M.A.L. (2022). Challenges in integrating SuDS into urban planning in developing country cities: a multicriteria analysis. *Aristas Journal*, 7–12.
38. Salazar, E., Henríquez, C., Durán, G., Qüense, J., & Puente-Sotomayor, F. (2021). How to define a new metropolitan area? The case of quito, Ecuador, and contributions for urban planning. *Land*, *10* (4), 413.
39. Salazar, E., Henríquez, C., Sliuzas, R., & Qüense, J. (2020). Evaluating spatial scenarios for sustainable development in Quito, Ecuador. *ISPRS International Journal of Geo-Information* , *9* (3), 141. https://doi.org/10.3390/ijgi9030141
40. Sandoval, V., & Sarmiento, JP (2020). A neglected issue: Informal settlements, urban development, and disaster risk reduction in Latin America and the Caribbean. *Disaster Prevention and Management: An International Journal*, *29* (5), 731–745. https://doi.org/10.1108/DPM-04-2020-0115

41. Sassi, E., Benabdelhafid, A., & Hammami, S. (2020). Territory planning model integrating GIS and Supply chain. *International Journal of Transportation Engineering and Technology*, *6* (1), 1. https://doi.org/10.11648/j.ijtet.20200601.11
42. Sisman, S., & Aydinoglu, A.C. (2020). Using GIS-based multi-criteria decision analysis techniques in the smart cities. *The International Archives of the Photogrammetry, Remote Sensing and Spatial Information Sciences*, *44*, 383–389. https://doi.org/10.5194/isprs-archives-XLIV-4-W3-2020-383-2020, 2020.
43. Sotelo, I. (2020). Scientific dissertation on territorial sustainability and the environment. *Environmental Observatory*, *23*, 9. https://doi.org/10.5209/OBMD.73165
44. Ulloa, R., & Martín, S. (2024). Determining the areas most suitable for urban land use while minimizing impact on natural areas. The case of the Machachi Valley, Ecuador. *Heliyon*, *10* (17).
45. Vega, C. A., & Cánovas, G. V. (2023). *Haiti: Society, Migration, and Development*. (First). El Colegio de Mexico AC.
46. Viana, CM, Pontius Jr, RG, & Rocha, J. (2022). A framework to evaluate land change simulation software with an illustration of a Cellular Automata–Markov model. *Agricultural Land Systems: Modeling Past, Present and Future Regional Dynamics*, 125.
47. Wang, J., Bretz, M., Dewan, M.A.A., & Delavar, M.A. (2022). Machine learning in modeling land-use and land cover-change (LULCC): Current status, challenges and prospects. *Science of the Total Environment*, *822*, 153559. https://doi.org/10.1016/j.scitotenv.2022.153559
48. Yacila, HC (2021). Urban concentration and inequality in Latin America. *Scientific Bulletin Sapiens Research*, *11* (1), 81–88.
49. Zhang, Z., Liu, J., Wang, C., Zhao, Y., Zhao, X., Li, P., & Sha, D. (2024). A spatial projection pursuit model for identifying comprehensive urban vitality on blocks using multisource geospatial data. *Sustainable Cities and Society* , *100*, 104998. https://doi.org/10.1016/j.scs.2023.104998

This page is intentionally left blank

Isolation of Fungi Associated with Rugose Spiralling Whitefly, *Aleurodicus Rugioperculatus* Martin in Different Host Crops

Kishor Pujar, Shivanna, B & Jemla Naik, D

University of Agricultural Sciences

ABSTRACT

The adults and nymphs of rugose spiralling whitefly, Aleurodicus rugioperculatus were collected from ten different host crops (coconut, banana, arecanut, bamboo palm, Syzygium sp. maize, guava, custard apple, sapota, karanja) during 2021-2023. The fungal isolation from adults and nymphs was carried out through plating technique and obtained colonies were pure cultured for identification. The results revealed that, Aspergillus spp. and Penicillium spp.. were found common in adults and nymphs of A. rugioperculatus collected on seven host crops (coconut, banana, arecanut, bamboo palm, guava, custard apple, and sapota). The fungi were identified based on conidia and conidiophore structure. The role of fungus in association with A. rugioperculatus is assumed to be symbiotic, where fungus would help in digestion of cellulose and provides nutritional supportThe adults and nymphs of rugose spiralling whitefly, Aleurodicus rugioperculatus were collected from ten different host crops (coconut, banana, arecanut, bamboo palm, Syzygium sp. maize, guava, custard apple, sapota, karanja) during 2021-2023. The fungal isolation from adults and nymphs was carried out through plating technique and obtained colonies were pure cultured for identification. The results revealed that, Aspergillus spp. and Penicillium spp.. were found common in adults and nymphs of A. rugioperculatus collected on seven host crops (coconut, banana, arecanut, bamboo palm, guava, custard apple, and sapota). The fungi were identified based on conidia and conidiophore structure. The role of fungus in association with A. rugioperculatus is assumed to be symbiotic, where fungus would help in digestion of cellulose and provides nutritional support.

Keywords: aleurodicus rugioperculatus, aspergillus spp., host crops and symbiosis.

Classification: LCC Code: QK602.3

Language: English

Great Britain Journals Press

LJP Copyright ID: 925665
Print ISSN: 2631-8490
Online ISSN: 2631-8504

London Journal of Research in Science: Natural & Formal

Volume 25 | Issue 6 | Compilation 1.0

Isolation of Fungi Associated with Rugose Spiralling Whitefly, *Aleurodicus Rugioperculatus* Martin in Different Host Crops

Kishor Pujar [α], Shivanna, B[σ] & Jemla Naik, D[ρ]

ABSTRACT

The adults and nymphs of rugose spiralling whitefly, Aleurodicus rugioperculatus were collected from ten different host crops (coconut, banana, arecanut, bamboo palm, Syzygium sp. maize, guava, custard apple, sapota, karanja) during 2021-2023. The fungal isolation from adults and nymphs was carried out through plating technique and obtained colonies were pure cultured for identification. The results revealed that, Aspergillus spp. and Penicillium spp.. were found common in adults and nymphs of A. rugioperculatus collected on seven host crops (coconut, banana, arecanut, bamboo palm, guava, custard apple, and sapota). The fungi were identified based on conidia and conidiophore structure. The role of fungus in association with A. rugioperculatus is assumed to be symbiotic, where fungus would help in digestion of cellulose and provides nutritional support.

Keywords: *aleurodicus rugioperculatus, aspergillus* spp., host crops and symbiosis.

Author α: Ph.D. Scholar, Department of Entomology, University of Agricultural Sciences, Bangalore-560065.
σ ρ: Ph.D. Scholar, Department of Entomology, University of Agricultural Sciences, Bangalore-56006.

I. INTRODUCTION

Whiteflies (Hemiptera: Aleyrodidae) are one of the most economically important group of pests with global distribution and wide host range (Kanakala and Ghanim, 2019). They cause damage in an active way by acting as vector for various plant viruses under the genera *Begomovirus*, *Crinivirus*, *Closterovirus etc.*) and passively by encouraging sooty mould deposits on plants through honeydew secretion (Head and Savinelli, 2008). Later, the sooty mould formed by the honeydew secreted by them leads to the closing of stomata as a result the gas exchange by the plants get interrupted that leads to poor development of plants. The invasive insect pest, rugose spiraling whitefly, *Aleurodicus rugioperculatus* (Hemiptera: Sternorrhyncha: Aleyrodidae) was described by Martin from Belize in Central America in 2004 based on puparia collected under the leaves of coconut. India is the only country in the Oriental region, where this whitefly has been introduced on coconut in the Pollachi region of Coimbatore district, Tamil Nadu and Kottayam in Kerala during July – August 2016 (Sundararaj and Selvaraj, 2017). The adaptation trait of the whiteflies to changing climate and to the new host is the key factor their spatiotemporal distribution. Since, whiteflies are phloem feeders which mainly suck the nutritionally deprived sap from the plant. The supplementation of the required nutrients (mainly essential amino acids) will be supplied by the microbes which resides inside their body in a symbiotic way. The two main functions of these endosymbionts of sap sucking insects are; those which are beneficial to the insect under specific ecological conditions and those which play a role in metabolic activities of the insect. (Gosalbes *et al.*, 2010). Fungus is being an unexplored microbe in the insect, hence the present study is focusing on the isolation and identification of fungal isolates of *A. rugioperculatus* collected on different hosts.

II. MATERIALS AND METHODS

2.1 Preparation of insects for experiment

The whiteflies were collected on different host plants (Coconut, Banana, from the different zones of Karnataka, from each zone minimum three locations were selected (Table 2). Alive whitefly adults and nymphs were collected from each host of each location for microbial isolation The adult whiteflies collected from different locations and hosts (Table 2) were surface sterilized with 70 per cent ethanol for 1 minute followed by 0.1 per cent sodium hypochlorite for 1 minute and then rinsed with sterile distilled water for 2 to 3 times to remove the external microbes and wax.

2.2 Serial dilution and plating

The media of 1M potato dextrose agar (PDA) were prepared for isolating the fungus respectively and autoclaved at 121℃ and 15 psi for one hour. Autoclaved PDA was allowed to cool then, streptomycin sulphate (100mg/ml) was added (to prevent bacterial growth) just before pouring the media into Petri plates (to avoid disintegration of antibiotic). The surface sterilized adults were crushed in a sterilized 1.5 ml micro-centrifuge tube using a sterilized micro pestle with 1 ml of phosphate buffer saline (PBS) solution (pH 7.4). Prior to that, micro-centrifuge tubes were labelled with date, host and location. The homogenized samples were centrifuged at 2000 RPM for 10 minutes. Then 100 µl of the homogenized mixture was added to micro centrifuge tubes containing 900 µl of sterile distilled water. Serial dilution of samples was made up to 10^{-4}.

Each Petri plate was labelled with host, location, date and respective dilution on the ventral surface. 100 µl of aliquot of all the dilutions were plated on PDA media and spread using a sterilized glass spreader. Then, Petri plates were wrapped with the para-film and incubated at 28℃ for 5-7 days in bio-oxygen demand (BOD) incubator (KEMI$^{@R}$). Further, plates were observed for microbial growth after every 48 hours.

2.3 Identification and characterization of microbes

Fungal plates, the incubation period was five to seven days, then fungal isolates were pure cultured in a single plate by inoculating a single spore in the PDA plate and incubated at room temperature for seven days. Further, fungi were identified by dropping the small portion of the mycelia on the glass slide with cotton blue dye. Then mycelia was sheared and observed under compound microscope at 100X lens. The conidiophore characters were observed for identification of fungus using a compound microscope (LEICA DM750) with a 100X lens at the Department of Plant Pathology, UAS Bangalore.

III. RESULTS AND DISCUSSION

3.1 Fungal diversity of whiteflies collected from different hosts

The fungal isolates *Aspergillus* spp. and *Penicillium* spp. were obtained from the *A. rugioperculatus* collected from the seven host crops i.e., coconut, banana, arecanut, bamboo palm, guava, custard apple, and sapota. The fungal isolates were pure cultured in a single plate by inoculating a single spore in the PDA plate and incubated at room temperature for seven days. The small portion of the mycelia was picked up and dropped on the glass slide with cotton blue dye. Then mycelia was sheared and observed under compound microscope at 100X lens.

3.2 Morphological identification of fungus

The colonies of the *Aspergillus* spp. were green and its reverse side was brown with biserrated conidiophores. Flask-shaped or cylindrical phialides either in a single or double series on the surface of a vesicle at the apex of a conidiophore was observed (Plate 1 and 2). Penicillium species had septate hyphae that gave rise to branched or unbranched conidiophores with secondary branches that give Penicillium a brush-like appearance (Plate 3 and 4) Wang *et al.* (2017) also identified the Penicillium species based on the brush like appearance of the conidiophores. Similar morphological characters of *A. flavus* were listed by Klich (2002) and Samson *et al.* (2019). In general, *Aspergillus* spp. and *Penicillium* spp. were recorded as a pathogen, food contaminator etc. But in the present study, selective presence of fungus in different hosts and absence of fungal isolate in the control plates revealed their association with *A. rugioperculatus*. As per the report of Okyere (2023), the most frequent fungal isolates found on insects are species of Aspergillus, Penicillium, Fusarium, Cladosporium, and Phycomycetes. As a support to the present study, *A. flavus*, was isolated as from the gut contents of wax moth *G. mellonella* larvae as potential microplastic particle-degrading microorganism in the study of Zhang *et al.* (2020). Poitevin *et al.* (2018) reported the association of *Trichoderma atroviride*, *Aspergillus flavipes*, *Aspergillus iizukae*, *Penicillium mallochii*, *Penicillium adametzioides* with European pepper moth (*Duponchelia fovealis*). The fungus, involves in digestion of the cellulose in leaves through production of cellulase. Which was clearly reported in the study of Klemm *et al.* (2002) that, binding of lignins to cellulose requires further degrading enzymes, which many fungi possess.

IV. CONCLUSION

The present study revealed the association of *Aspergillus* sp. and *Penicillium* sp. with *A. rugioperculatus* on different host crops. The facultative fungi residing in the insects are less explored and most of the insect-associated fungi are uncultivable, hence the low diversity with respect to fungi was observed in the present study.

REFERENCES

1. Gosalbes M J, Latorre A, Lamelas A and Moya A (2010), Genomics of intracellular symbionts in insects. International Journal of Medical Microbiology, **300**(5): 271-278.
2. Head G and Savinelli C (2008), Adapting insect resistance management programs to local needs. Insect resistance management: biology, economics and prediction, p.305.
3. Kanakala S and Ghanim M (2019), Global genetic diversity and geographical distribution of *Bemisia tabaci* and its bacterial endosymbionts. *PLoS ONE,* **14**:e0213946.
4. Klemm D, Schmauder H and Heinze T (2002), Biopolymers. *Cellulose*, **6**: 275-319.
5. Klich M A (2002), Identification of common *Aspergillus* species. CBS
6. Okyere A A (2023), Food Safety Management of Insect-Based Foods. In *Food Safety Management* (pp. 223-233). Academic Press.
7. Poitevin C G, Porsani M V, Poltronieri A S, Zawadneak M A C and Pimentel I C (2018), Fungi isolated from insects in strawberry crops act as potential biological control agents of *Duponchelia fovealis* (Lepidoptera: Crambidae). Applied entomology and zoology **53**: 323-331.
8. Samson R A, Houbraken J, Thrane U, Frisvad, J C and Andersen B (2019) Food and indoor fungi. Westerdijk Fungal Biodiversity Institute.
9. Sundararaj R and Selvaraj K (2017), Invasion of rugose spiralling whitefly, *Aleurodicus rugioperculatus* Martin (Hemiptera: Aleyrodidae): A potential threat to coconut in India. Phytoparasitica **45**:71–74.
10. Wang X C, Chen K, Zeng Z Q (2017), Phylogeny and morphological analyses of Penicillium section Sclerotiora (Fungi) lead to the discovery of five new species. Scientific Reports (**7**): 8233.

11. Zhang J, Gao D, Li Q, Zhao Y, Li L, Lin H, 2020, Biodegradation of polyethylene microplastic particles by the fungus *Aspergillus flavus* from the guts of wax moth *Galleria mellonella*. Science of the Total Environment **704**: 135931.

Plate 1: Morphology of *Aspergillus* spp.

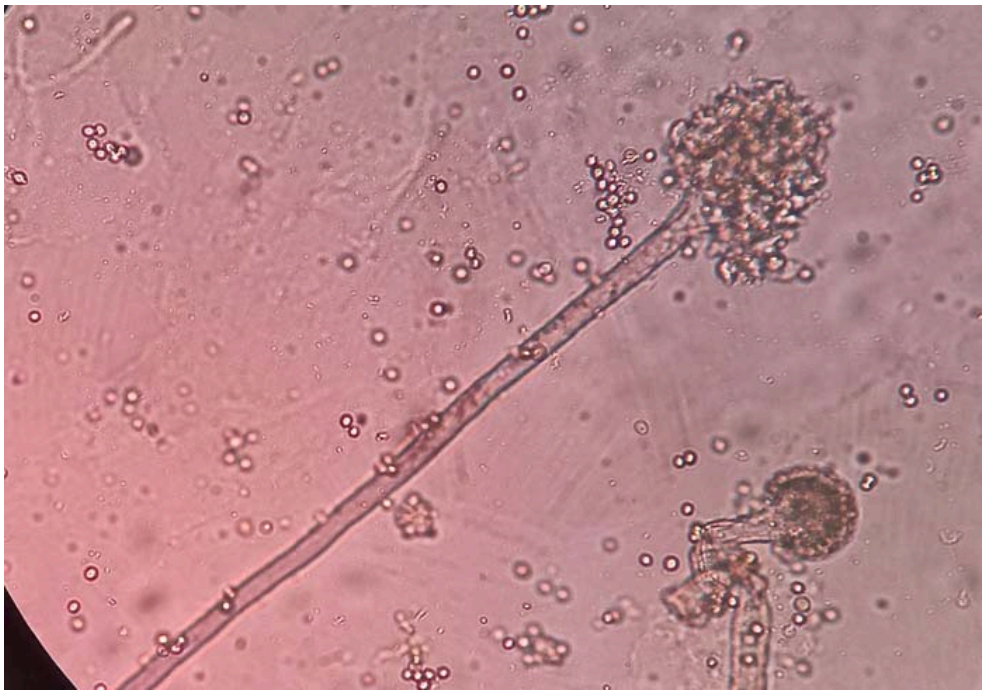

Plate 2: Conidia and conidiophores of *Aspergillus* spp.

Plate 3: Morphology of *Penicillium* sp.

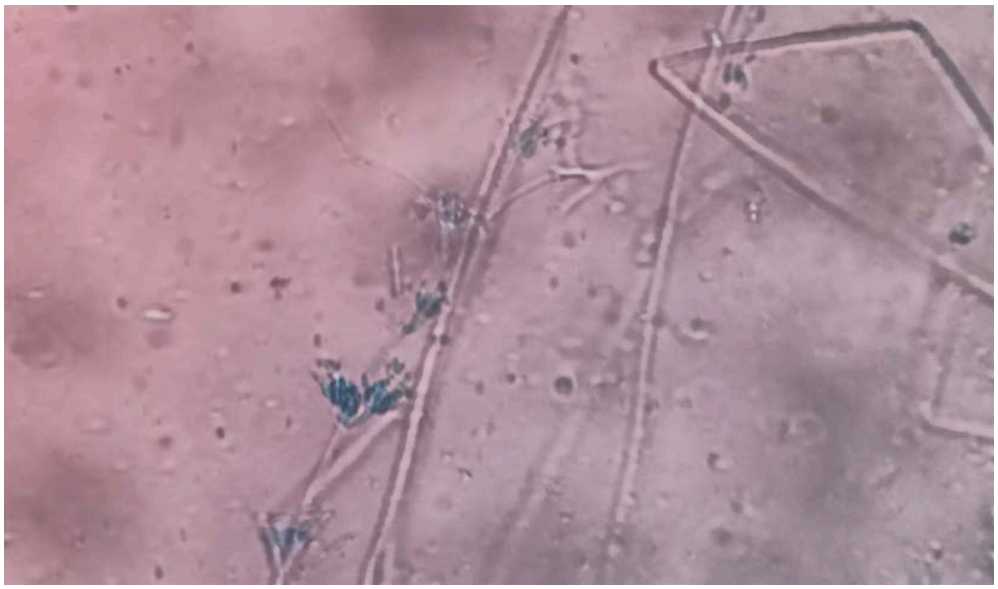

Plate 4: Conidia and conidiophores of *Penicillium* sp.